

**Ultra-Low Phase Noise Microwaves from Optical Signals**

by

**Jennifer A. Taylor**

B.A., University of Arkansas, 2004

M.S., University of Colorado, 2008

A thesis submitted to the  
Faculty of the Graduate School of the  
University of Colorado in partial fulfillment  
of the requirements for the degree of  
Doctor of Philosophy  
Department of Physics

2012

This thesis entitled:  
Ultra-Low Phase Noise Microwaves from Optical Signals  
written by Jennifer A. Taylor  
has been approved for the Department of Physics

---

Dr. Scott Diddams

---

Prof. Neil Ashby

---

Prof. Henry Kapteyn

---

Prof. Konrad Lehnert

---

Prof. Kelvin Wagner

Date \_\_\_\_\_

The final copy of this thesis has been examined by the signatories, and we find that both the content and the form meet acceptable presentation standards of scholarly work in the above mentioned discipline.

Taylor, Jennifer A. (Ph.D., Physics)

Ultra-Low Phase Noise Microwaves from Optical Signals

Thesis directed by Dr. Scott Diddams

Continuous-wave lasers locked to high-finesse optical reference cavities are oscillators that produce  $\sim 500$  THz optical signals with unprecedented stability. Indeed, sub-femtosecond fractional frequency instability at one second averaging can now be achieved. A self-referenced femtosecond laser frequency comb (FLFC) is used as a frequency divider to provide a phase-coherent link between optical and microwave domains, dividing the frequency down to the gigahertz range while also transferring the stability of the original signal. Photodetectors then convert the optical pulses into electronic signals. The resultant 10 GHz microwave signals have ultra-low phase noise below  $-100$  dBc/Hz at 1 Hz offset, surpassing that of traditional microwave oscillators. This new approach offers significant improvement for many applications that rely on stable microwave signals, and may even create new measurement technologies otherwise unachievable with current signal sources.

In reality, fundamental and technical sources of noise in each stage of the optical-to-microwave generation process limit the ultimate achievable stability of the signal. Optical reference cavities are limited by environmental effects and thermal fluctuations, and FLFC dividers suffer from intrinsic timing jitter, amplitude noise, and limited stabilization servo bandwidth. However, it is the seemingly straightforward photodetection of optical pulses that proves to be the limiting factor in the ultimate noise floor of these signals.

In this thesis, I describe the noise limitations of each part of the optical-to-microwave scheme, particularly focusing on the noise limitations of photodetection. I will give a basic representation of these photodetection noise phenomena in terms of the physical behavior of optically-generated electrons in semiconductor photodiodes. The two main photodetection noise phenomena—shot noise and amplitude-to-phase conversion—will be thoroughly characterized in the context of generation of 10 GHz low phase noise signals. Finally, I will use this characterization of photodetector noise

to choose optimal photodetectors and operating conditions to realize unprecedentedly low phase noise signals with a variety of optical-to-microwave generation schemes.

## Dedication

To my husband, Bart Taylor, for his unfailing support of this journey and the countless sacrifices made, small and large, so this work could come to fruition.

## Acknowledgements

NIST is an amazing organization with wonderful people doing state-of-the-art research. As an undergraduate I dreamed of doing fascinating and fundamental research at such a prestigious institution. Some days I am still amazed that I actually got to spend my graduate career working here.

I would like to thank Dave Howe for offering me the opportunity to begin my graduate career at NIST and for continued support during my tenure as a graduate student. I also thank Neil Ashby for his academic and professional guidance while here at NIST, providing a link to academia while I was somewhat removed from campus. I am grateful to Chris Oates and Scott Diddams for affording me the opportunity to collaborate with their group. Without the resources of the Optical Frequency Measurements group, none of this research would have been possible.

I could not have accomplished any of this work without the help of my many colleagues. I am indebted to Craig Nelson and Archita Hati for countless hours of instruction and supervision as I learned the fundamentals of phase noise. I am grateful to Tara Fortier, Frank Quinlan, and Haifeng Jiang for insights into perplexing problems encountered while building and measuring these systems. I am pleased to be able to call my colleagues friends.

I appreciate the foundational instruction of my undergraduate advisors, John and Gay Stewart, and their continued support to this day.

Finally, thank you to my committee members—Scott Diddams, Neil Ashby, Henry Kapteyn, Konrad Lehnert, and Kelvin Wagner—for giving their time and resources for the completion of this dissertation.

## Contents

<b>Chapter</b>		
<b>1</b>	<b>Introduction</b>	<b>1</b>
1.1	The need for low-noise microwave signals . . . . .	1
1.2	The optical-to-microwave generation method . . . . .	3
1.3	Applications requiring ultra-stable microwaves . . . . .	5
1.4	Alternative approaches to microwave generation . . . . .	6
1.5	Noise limitations of the optical-to-microwave scheme . . . . .	8
1.6	Goal of this work/thesis statement . . . . .	10
<b>2</b>	<b>Generation of Microwaves from Optical Sources</b>	<b>11</b>
2.1	The Optical-to-Microwave Scheme . . . . .	11
2.1.1	Optical Frequency References . . . . .	11
2.1.2	Femtosecond Laser Frequency Dividers . . . . .	14
2.1.3	Photodetectors . . . . .	20
2.2	Noise Limitations . . . . .	21
2.2.1	Optical Reference Noise . . . . .	22
2.2.2	Femtosecond Laser Frequency Divider Noise . . . . .	24
2.2.3	Fiber Link Noise . . . . .	25
2.2.4	Photodetector Noise . . . . .	26

<b>3</b>	<b>Semiconductors, Photodetection, and Devices</b>	<b>28</b>
3.1	Introduction to Semiconductors and Photodiodes . . . . .	28
3.1.1	P-N and P-I-N Junctions . . . . .	30
3.1.2	Photodetector Parameters . . . . .	34
3.1.3	P-N and P-I-N Semiconductor Photodetectors . . . . .	36
3.1.4	Photodiode Structures . . . . .	37
3.2	Devices . . . . .	40
3.2.1	DDR PIN Diodes . . . . .	41
3.2.2	Uni-traveling carrier diodes . . . . .	44
<b>4</b>	<b>Noise Characterization and Photodetection</b>	<b>51</b>
4.1	Introduction to Noise–Frequency Stability in the Time and Frequency Domains . . .	51
4.1.1	Time Domain Representations of Frequency Stability–The Allan Variance . .	53
4.1.2	Frequency Domain Representations of Frequency Stability– $\mathcal{L}(f)$ . . . . .	54
4.1.3	Power Law Scale and Noise Types . . . . .	57
4.2	Noise in Photodetectors . . . . .	58
4.2.1	Thermal Noise . . . . .	59
4.2.2	Shot Noise . . . . .	60
4.2.3	Amplitude to Phase Conversion . . . . .	64
<b>5</b>	<b>Characterization of Photodetector Noise</b>	<b>67</b>
5.1	Impulse Response . . . . .	67
5.2	Saturation and Repetition Rate . . . . .	71
5.2.1	Reduced photodiode saturation with Er:Fiber laser via rep rate multiplication	72
5.2.2	Fabry-Perot filter cavity . . . . .	72
5.2.3	Mach-Zehnder Interferometer . . . . .	73
5.3	Amplitude-to-Phase Conversion . . . . .	78
5.3.1	Phase Bridge Measurement System . . . . .	79

5.3.2	AM-to-PM Results . . . . .	84
5.3.3	Prediction of Phase noise from RIN using $\alpha$ . . . . .	87
<b>6</b>	<b>Demonstrations of Ultra-Low Phase Noise Microwave Signals</b>	<b>94</b>
6.1	Absolute Phase Noise of Photonic Oscillator . . . . .	95
6.2	Residual and Absolute Phase Noise with Hybrid Photonic-Microwave Oscillator . . .	101
6.3	Residual Noise on Er:Fiber laser with repetition rate multiplication . . . . .	105
6.4	Residual phase noise with MUTC diodes . . . . .	108
<b>7</b>	<b>Conclusion and Future Work</b>	<b>110</b>
7.1	Review of results and analysis . . . . .	110
7.2	Future Work . . . . .	111
	<b>Bibliography</b>	<b>115</b>

## Tables

### Table

3.1	List of DSC diodes used in this work . . . . .	42
3.2	List of MUTC diodes used in this work . . . . .	50

## Figures

### Figure

1.1	Optical to microwave generation scheme . . . . .	4
1.2	Phase noise of various microwave oscillators . . . . .	7
2.1	Clock transitions . . . . .	13
2.2	Optical Reference Cavity . . . . .	14
2.3	Schematic of Optical Reference . . . . .	15
2.4	Femtosecond mode-locked laser output . . . . .	16
2.5	Ti:S Stabilization . . . . .	17
2.6	Ti:S Spectrum . . . . .	19
2.7	Er:Fiber laser spectra . . . . .	20
2.8	Optical Reference Noise . . . . .	23
2.9	Optical Fiber Link . . . . .	26
3.1	PN Junction . . . . .	31
3.2	PN Energy bands . . . . .	31
3.3	Biasing of PN junction . . . . .	32
3.4	P-I-N junction . . . . .	33
3.5	P-I-N energy band . . . . .	37
3.6	Schematic of DDR Photodiode . . . . .	39
3.7	Energy Band Diagram for MUCT Photodiode . . . . .	40

3.8	Example Schematic of MUTC Diode . . . . .	40
3.9	Device structure of DSC photodiodes . . . . .	41
3.10	Dual-packaged DSC Photodiode . . . . .	43
3.11	GRIN Lens Beam Profile . . . . .	43
3.12	DSC Connection . . . . .	45
3.13	MUTC Devices . . . . .	46
3.14	MUTC Connection . . . . .	47
3.15	Photos of MUTC Setup . . . . .	48
3.16	Device Structure of MUTC Diodes . . . . .	50
4.1	Frequency Spectra . . . . .	54
4.2	Phase Bridge . . . . .	56
4.3	Time and Frequency Power Laws . . . . .	58
4.4	Photodetection Circuit . . . . .	59
4.5	Thermal and Shot Noise Powers . . . . .	62
4.6	Saturation in DSC Photodiodes . . . . .	63
4.7	Pulse Energy and Repetition Rate . . . . .	64
5.1	DSC Impulse Response . . . . .	69
5.2	MUTC Impulse Response . . . . .	70
5.3	Fabry-Perot Cavity . . . . .	73
5.4	Fabry-Perot Mode Multiplication . . . . .	73
5.5	Schematic of Fiber MZI . . . . .	74
5.6	Filtered Outputs in Time and Frequency Domains . . . . .	75
5.7	Repetition Rate Multiplication for DSC Diode . . . . .	76
5.8	Repetition Rate Multiplication for MUTC Diodes . . . . .	77
5.9	Free-space MZI for Ti:S . . . . .	78
5.10	Saturation with Ti:S Rep Rate Multiplication . . . . .	78

5.11	Quadrature Phase Bridge . . . . .	80
5.12	Demodulation Phase Bridge . . . . .	83
5.13	Demodulation Phase Bridge . . . . .	84
5.14	AM-to-PM with Rep Rate Multiplication . . . . .	86
5.15	AM-to-PM Dependence on Optical Modes . . . . .	88
5.16	Precision of Phase Noise with $\alpha$ . . . . .	89
5.17	Phase Extraction from FFT . . . . .	91
5.18	Calculation of $\alpha$ from FFT . . . . .	92
6.1	Absolute Phase Noise Measurement Schematic . . . . .	96
6.2	Absolute Phase Noise . . . . .	99
6.3	Absolute Timing Stability . . . . .	100
6.4	Phase Noise of 10 GHz Oscillators . . . . .	102
6.5	Hybrid Oscillator . . . . .	103
6.6	Hybrid Oscillator Phase Noise . . . . .	104
6.7	Er:Fiber Phase Noise Measurement System . . . . .	106
6.8	Repetition Rate Phase Noise with DSC Diode . . . . .	107
6.9	Repetition Rate Phase Noise with MUTC Diodes . . . . .	109

# Chapter 1

## Introduction

### 1.1 The need for low-noise microwave signals

Time—or more specifically, time difference—is one of the most fundamental quantities that can be measured in nature; in fact, the second is the most accurately realized unit of measurement [1]. An ideal sine wave provided by a frequency source is in essence a clock with perfectly spaced “ticks,” which can be used as a kind of ruler for measuring the timing and events. Likewise, time’s relationship to distance means that a clock can also be used to measure length. In fact, the meter is internationally defined as the length of the path traveled by light in vacuum during a time interval of  $1/299\,792\,458$  of a second. Accurate measurements of these two fundamental quantities alone comprise a vast array of scientific applications today.

Of course, no frequency reference can produce a prolonged, perfect sine wave; there is always some noise associated with fluctuations in the zero crossing (phase) or magnitude (amplitude) of the signal. For example, with improved measurement precision, frequency references of the past, such as the rotation of the earth, have been found to slowly change over time, and have been gradually replaced over the course of centuries with increasingly more stable and accurate mechanical and electronic clocks<sup>1</sup> [1]. Not coincidentally, the “tick rate” of these references have in general increased over time, with periods decreasing from years and days to minutes and seconds and beyond.

---

<sup>1</sup> Stability, or precision, is the degree to which the interval between clock ticks remains constant, and accuracy is the degree to which the interval between clock ticks matches the interval given by an agreed upon standard (e.g. ultimately traceable to the SI definition of the second based on the Cesium ground-state hyperfine transition of 9,192,631,770 oscillations per second).

Through the end of the twentieth century, technologies that require stable frequency sources for reference have primarily relied on electronic and atomic oscillators—for example, those based on quartz resonators or cesium atomic clocks—to provide stable frequency signals on the order of megahertz up to a few tens of gigahertz. However, the development of these technologies is in large part limited by the stability of these references. For example, radar, which uses reflections of radio waves to determine range, direction, or speed of objects, is limited by the current stability of available oscillators; if the radar signal is noisy, some changes in object speed or size are so small that they are indistinguishable from the noise. However, the development of new frequency sources that dramatically improve upon the stability of existing frequency references would push existing technologies to a new level of performance and enable entirely new fields of research.

In principle, a clock based on a frequency transition  $\sim 100,000$  times higher than a microwave signal would provide orders of magnitude improvement in stability because of the finer division of time and thus higher precision [2] [3]. Ultimately, the development of optical clocks through the second half of the twentieth century provided the means for such ultra-stable optical references. The long-term stability ( $> 1$  s) provided by atomic transitions is ideal for clocks or any measurement requiring exact traceability to the SI second. However, for most applications requiring a reference signal for timing and metrology, such as those mentioned previously, the continuous wave lasers locked to optical reference cavities serving as the local oscillator for these systems provide signals with unprecedented short-term stability at less than one second.

To generate an interval of time with an optical standard, one must be able to reliably count these extremely rapid oscillations. However, for applications requiring signals on the order of tens of gigahertz, a frequency on the order of  $10^{15}$  Hz corresponds to a period of 1 fs, much too fast to be counted by conventional electronics. Dividing a very stable optical frequency down to a microwave frequency where it could be readily handled is quite compelling, especially if the stability of the optical signal can be preserved during the division process. It is all the more enticing because the optical phase noise power spectrum, denoted by  $\mathcal{L}(f)$ , is reduced by a factor of  $N^2$  (or  $20 \log N$  in

dB) where  $N$  is the optical-to-microwave frequency ratio  $f_{\text{opt}}/f_{\text{microwave}}$ :

$$\mathcal{L}_{\text{microwave}}(f) = \mathcal{L}_{\text{opt}}(f)/N^2. \quad (1.1)$$

From hundreds of terahertz to tens of gigahertz,  $N$  is on the order of  $10^5$ , corresponding to 100-dB suppression on noise.

If optical signals are to be divided down to stable microwave sources, then there must be some mechanism for translating the terahertz signal to a microwave signal while preserving the stability offered by a higher frequency. Previously, connecting optical to microwave and making an actual measurement of an optical frequency involved a complicated, multi-stage laser frequency synthesis chain that multiplied in harmonic steps from microwave frequencies to optical frequencies of interest [3]. The advent of mode-locked laser frequency combs [4] [5] [6] enabled a much more straightforward method of optical-to-microwave division while maintaining the ultra-stable performance of the original optical source [7] [8] [9].

## 1.2 The optical-to-microwave generation method

This optical-to-microwave generation scheme, shown in Figure 1.1, will be described fully in Chapter 2 but is briefly described here. The output of a mode-locked femtosecond laser is a train of optical pulses separated by a certain time  $T_{\text{rep}}$ . In the frequency domain, these pulses produce a comb of individual frequencies separated by the repetition rate,  $f_{\text{rep}} = 1/T_{\text{rep}}$ . The repetition rate is determined by the cavity length for each individual laser and is typically between tens of megahertz to a few gigahertz. If the frequency of one of the “teeth” can be controlled by the stable frequency of the optical reference cavity, then the repetition rate of the mode-locked laser is carefully controlled as well, and the stability of the optical reference cavity is transferred to the whole frequency comb and to the microwave domain.<sup>2</sup>

Precise measurement of the repetition rate is key to completing the frequency division. Photodetection of the stabilized optical pulse train from the mode-locked laser produces a corresponding

---

<sup>2</sup> Control of the offset frequency,  $f_0$ , is also required for stabilization of the frequency comb. It has been neglected here for simplicity but will be considered in detail in Chapter 2.

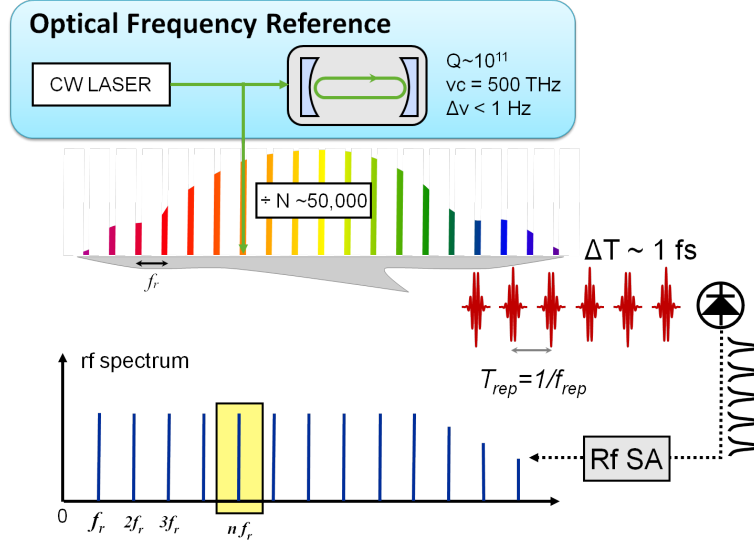


Figure 1.1: Optical to microwave generation scheme. Rf SA is microwave spectrum analyzer.

electronic pulse train; in the frequency domain, this produces another comb, a series of discrete tones at harmonics of the pulse repetition rate. For example, a pulse train with  $f_{rep} = 1 \text{ GHz}$  will produce tones at 1 GHz, 2 GHz, 3 GHz, and so on, up to the bandwidth of the photodetector. An electronic bandpass filter is used to select the desired frequency, resulting in the ultimate generation of a microwave signal having the same unprecedented stability of the optical reference cavity.

This frequency comb-based photonic generator for producing ultra-stable, low phase noise microwaves has many benefits. Unlike other microwave oscillators whose frequency is fixed, often determined by some physical artifact that is difficult or impossible to change, this method of frequency synthesis is tunable and scalable. In this work, the experiments and analysis focuses on 10 GHz, which is a historically interesting frequency used in many applications. However, given the number of harmonics produced from photodetection of the optical pulse train, any frequency that is a harmonic of the repetition rate could be selected, up to the bandwidth of the photodetector. While commercial photodetector bandwidths may be limited to about 100 GHz at the present time, faster ones are under continuous development, meaning this method will continue to be scalable to even higher frequencies as this technology continues to expand [10]. Virtually any frequency in the microwave domain could be synthesized by changing the repetition rate of the femtosecond laser

and shifting the offsets between the comb tooth and the reference frequency from the cavity.

### 1.3 Applications requiring ultra-stable microwaves

The availability of microwave signals with sub-femtosecond stability would be advantageous to several significant scientific and technical applications. A few examples are listed here. One example would be the use of these microwave signals as a stable clock for analog-to-digital conversion (ADC). Electronic ADC has increased timing jitter as the sampling rate increases, limiting resolution; but ADC clocked with a low-phase noise, high-frequency ( $>10$  GHz) reference oscillators would provide timing jitter and resolution beyond that achievable with state-of-the-art electronics ( $<10$  fs over narrow-band integration limits) [11] [12].

A number of large-scale scientific facilities would benefit from femtosecond-level timing accuracy between remotely located optical and microwave sources. One such application is very-long baseline interferometry (VLBI), a technique that interferometrically combines signals (tens of gigahertz to hundreds of gigahertz) from widely separated radio telescope arrays [13] [14] [15]. The separation of the antennae, up to 18 km apart, causes the same astronomical signal to arrive at each with a large differential phase, thus achieving exceptionally high angular resolution. Stability in timing distribution is also important for advances envisioned in particle accelerators such as x-ray free-electron lasers (XFEL) [16], in which electron beams are accelerated over kilometer-long distances and require precise timing between optical and electronic systems as they interact with these very fast moving electrons [17] [18] [16] [19]. Because of the long distances between objects in these two systems, a highly stable reference signal is required for precise synchronization across the facilities.

Microwave waveform synthesis and generation uses optical combs to generate specifically shaped microwave spectra. ADC technology and high timing jitter prevent the creation of ultrabroad-bandwidth arbitrary waveforms in the 10-60 GHz range using electronic means, but optical pulse shaping can create arbitrary waveforms by modifying the spectrum and phase of an optical comb to produce the desired wave shape before being converted into the electrical domain by a high-speed

photodetector [20] [21].

An ultra-stable frequency signal could also be used in secure encryption of information [22]. By using a frequency standard with the best stability and accuracy, secure information could be encoded as a very small frequency offset or phase modulation on the signal and transmitted from one place to another. The encoding would be so small that it would be undetectable in the noise of a regular oscillator; only a recipient of this signal in possession of an equally stable oscillator could decode the information.

As previously mentioned, more stable signals would enable detection of smaller or slower-moving objects with radar. However, if the oscillator performance of the radar signal were to improve, similar improvements in noise characteristics of the other components in radar systems would have to be improved as well, as existing systems only had to perform well enough to accommodate previous signal references. As better and better frequency sources become more widely available, one would expect future generations of radar systems to be built with these lower-noise signals in mind.

#### 1.4 Alternative approaches to microwave generation

The standard approach for generating 10-GHz signals is directly from a microwave oscillator. There are a few basic types of microwave oscillators that are typically used to generate signals with short-term stability.

Ubiquitous crystal oscillators are based on the mechanical resonance of a vibrating, piezoelectric crystal; quartz is the most commonly used material. Their popularity stems from their size and low cost of manufacturing, and they come in a variety of frequencies from a few kilohertz up to several hundred megahertz. Some frequency generators are based on quartz oscillators, then use electronics to multiply and synthesize higher frequency signals. However, multiplication of the frequency also multiplies the phase noise. For example, a state-of-the-art quartz-based commercial synthesizer has a phase noise of  $\mathcal{L}(f) = -60$  dBc/Hz at 1 Hz frequency offset, carrier scaled to 10 GHz (curve (b) in Figure 1.2) [23].

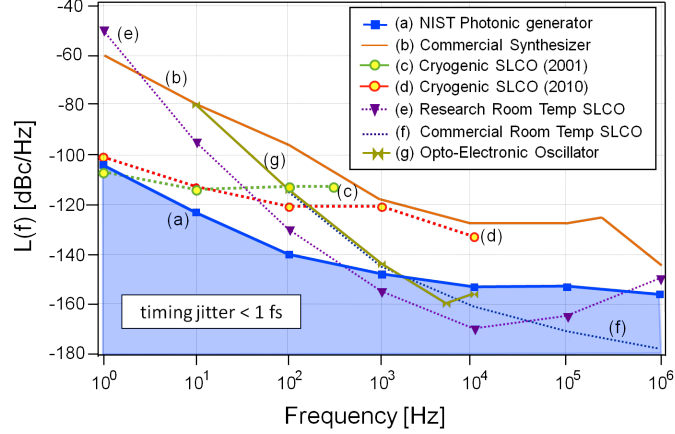


Figure 1.2: Approximate single-sideband phase noise for several leading microwave generation technologies in the 10 GHz range. Spurious tones have been neglected for all data. a. Result of the present work, b. A commercial, quartz-based synthesizer [23], scaled to 10 GHz, c and d. Cryogenic sapphire oscillators [24] [25], e. Research room-temperature sapphire oscillator [26], f. Commercial room-temperature sapphire oscillator, g. Opto-electronic oscillators [27].

Dielectric resonator oscillators, or DROs, are based on high-Q dielectric disc-shaped resonators. They can reach frequencies of 10 GHz or more based on the size of the cavity. They have excellent phase noise far from carrier but rather high close-in. Sapphire-loaded cavity oscillators (SLCOs) are a type of dielectric oscillators that use a sapphire whispering-gallery mode (WGM) resonator suspended inside of a metal cavity to generate microwave signals (curves (e) and (f) Figure 1.2) [28] [26]. Carrier suppression interferometers are then used to reduce carrier power and reduce noise. These oscillators can generate very low phase noise signals far from carrier, but have very high close-in noise. While much development of these oscillators is done in a research environment, one can purchase a commercial version at a variety of microwave frequencies around 10 GHz with comparable far-from-carrier performance; however, these systems are quite expensive and offer very limited tunability in frequency. Cryogenics have been used to improve phase noise in this regime (curves (c) and (d) Figure 1.2) [24] [29] [30] [25]. However, the cryogenic approach loses the far-from-carrier performance of room temperature dielectric oscillators. The introduction of a cryogenic cooling system also adds complexity to operation of the system.

Opto-electronic oscillators (OEOs) are microwave oscillators that use optical waveguides as

a high-Q resonators for modulated optical signals [31]. This resonator could be a long optical fiber delay line (up to tens of kilometers), a Fabry-Perot cavity, or a whispering-gallery mode (WGM) resonator. In a typical OEO, a modulated optical signal is passed through the resonator and then photodetected, amplified, filtered, and phase adjusted before being fed back into the modulator. If the gain of the feedback loop is large enough, self-sustained oscillation can be generated [31]. OEOs have achieved low noise floors at Fourier frequencies  $> 1$  kHz [27], but most designs suffer from the presence of harmonic spurs and poor performance at low Fourier frequencies. Additionally, all such photonic devices with photodetectors have a noise floor ultimately limited by shot noise and the power-handling capabilities of the high-speed photodiode.

Figure 1.2 compares the phase noise ( $\mathcal{L}(f)$ ) of typical microwave oscillators to the photonic generation approach developed in this thesis. The close-to-carrier region (1 Hz to 100 Hz Fourier frequency offset) is the area in which the photonic generator (curve (a)) excels above all other room-temperature microwave oscillators. With a thermal noise-floor limited optical reference cavity, a phase noise of below  $\mathcal{L}(f) = -100$  dBc/Hz at a 1 Hz offset is easily achievable, with  $\mathcal{L}(f) = 117$  dBc/Hz or below quite possible with further developments and new optical references [32] [33] [34]. The present close-to-carrier noise level is comparable to only the very best cryogenic dielectric oscillators (curves (c) and (d)) [24] [29] [30] [25]. The OEO (curve (g)) does not have the close-to-carrier stability of the photonic generator or cryogenic oscillators. While this technique has demonstrated low noise floors, optical techniques including the OEO and the photonic generator are still limited by photodetection. This limitation will be discussed in the following section.

## 1.5 Noise limitations of the optical-to-microwave scheme

While the photonic generator does produce the lowest noise signal over the widest range of offset frequencies, it is not without its own noise limitations. Optical reference cavities are ultimately limited close-to-carrier by environmental effects and Brownian thermal fluctuations of the mirrors [35] [36] [33]. The femtosecond divider limitations include the timing jitter on pulses, amplitude noise on the pump laser, and comb stabilization servos [37] [38]. However, as will be

discussed in detail in Chapter 2, these sources of noise have been thoroughly characterized and very tightly controlled, and unprecedented low levels of noise have still been achieved. It is the deceptively simple photodetection process that proves to be the limiting factor in the ultimate noise floor of these microwave signals.

Photodetection is the final part of the scheme that converts optical pulses into an electronic signal for use in and analysis with standard electronic devices. Photodetection itself is one of the most basic components of all photonic systems. Beyond ubiquitous lightwave communications systems, for some applications it is important to know precisely the arrival time of a light pulse, the timing structure of complex amplitude modulation on a pulse burst, or simply the rate of a periodic train of pulses. For example, photodetection of precisely timed signals is important for optical links used in emerging microwave photonics applications such as radio over fiber, phased-array radars [39] [40], arbitrary waveform generation [21] [41], radio astronomy [15], large-scale free-electron lasers [42] [16] and optical analog-to-digital conversion [12].

Besides the fundamental shot noise of the photocurrent, the conversion of laser amplitude noise into electronic phase noise during photodetection has been previously identified as a limiting noise source for some applications [43] [44] [45] [46] [47] [27]. Any noise introduced by the photodetection process degrades the integrity of the original signal. Therefore, characterizing and improving the noise performance of photodetectors is vital for creating the lowest possible phase-noise signals from a photonic generator.

Some alternative electro-optic techniques for extracting microwave signals from a mode-locked laser pulse train have recently been developed to address issues related to excess noise in photodetection [42] [48]. However, these optical systems lack the simplicity of photodetection while adding even more complexities to the system, which could lead to more sources of errors. Furthermore, the recent advances in photodetection that will be shown in this work have ultimately outpaced the results demonstrated by this alternative method [48].

Because of its simplicity, photodetection remains the standard method of converting optical signals to electronic signals. Advances in photodiode design and manufacturing produce

increasingly better devices. Careful characterization of these noise properties can inform future development, producing devices that overcome these conspicuous noise limitations.

## **1.6 Goal of this work/thesis statement**

Given the initial promise of the photonic generator approach, further development of this technique for generation of ultra-stable, low-phase noise signals is clearly valuable. In this thesis, I will describe in detail the optical-to-microwave scheme, the noise limitations of each part of the photonic oscillator, and the solutions for minimizing these effects. I will particularly focus on the noise limitations of photodetection. I will give a basic representation of these photodetection noise phenomena in terms of the physical behavior of photonic-generated electrons in semiconductor photodiodes. The two main photodetection noise phenomena—shot noise and amplitude-to-phase conversion—will be thoroughly characterized in the context of generation of 10 GHz low phase noise signals. Finally, I will use this characterization of photodetector noise to choose photodetectors and operating conditions to realize unprecedentedly low phase noise signals with a variety of optical-to-microwave generation schemes.

## Chapter 2

### Generation of Microwaves from Optical Sources

#### 2.1 The Optical-to-Microwave Scheme

The optical-to-microwave conversion scheme used in this thesis consists of three distinct parts, which are shown in Figure 1.1 and described in detail in this chapter. The first section is the original optical frequency reference signal, which is generated from a stable continuous wave (CW) laser locked to a narrow, high-frequency atomic transition. Next, one comb mode of a self-stabilized femtosecond laser frequency comb (FLFC) is locked to this ultra-stable signal, which relates optical frequencies to microwave frequencies via its repetition rate. Finally, the train of pulses out of the mode-locked FLFC impinges on a photodetector, inside of which the conversion from optical frequencies to microwave frequencies occurs.

##### 2.1.1 Optical Frequency References

For over sixty years, the basis for the most stable frequency sources in the world has been electronic and hyperfine atomic transitions inside atoms [2]. Early on, microwave transitions, such as the one in Cesium that defines the second, were exclusively used, as microwave technologies were well-established and stable optical oscillators were still developing. However, a clock based on a higher-frequency transition would provide orders of magnitude improvement in stability by dividing time into smaller intervals. The fractional frequency instability of a clock as a function of the averaging time,  $\tau$ , (quantified by the Allan Deviation; see Section 4.1.1) can be written for an oscillator locked to an atomic transition with frequency  $\nu_0$  and linewidth  $\Delta\nu$ :

$$\sigma_y \approx \frac{\Delta\nu}{\nu_o\sqrt{\tau N}}, \quad (2.1)$$

where  $N$  is the number of atoms [3]. It is evident that increasing the frequency and decreasing the linewidth will decrease the overall timing instability. Therefore, a narrow linewidth atomic transition at an optical frequency ( $\sim 10^{15}$ ) instead of a microwave frequency ( $\sim 10^{10}$ ) would improve the performance by a factor of  $10^5$ . Improvement can also be gained by increasing the number of atoms being interrogated, thus increasing the signal to noise ratio (S/N).

The long-term stability ( $t < 1s$ ) offered by atomic transitions is vital for a clock, a frequency source intended to provide stability as well as accuracy at long timescales. However, for signals requiring stability of phase, such as is the focus of this research, short-term stability ( $t < 1s$ ) is necessary. The trapping and probing of atoms in an optical frequency reference is quite noisy at these short times, and ultimately the reference cavity serving as the local oscillator for these systems sets the limit at less than one second for the stability of such low-phase noise signals. We will briefly discuss the atomic aspect of the optical frequency references used in this work; however, the main focus of ultra-low phase noise signal generation will be the reference cavities of these systems.

There are many different atoms and ions used in optical frequency references, but the following are the four systems regularly used in NIST's optical-to-microwave scheme: calcium (Ca), ytterbium lattice (Yb), mercury ion ( $Hg^+$ ), and aluminum ion ( $Al^+$ ). These four atoms have very narrow atomic transitions, often called clock transitions, which are insensitive to external perturbations and ideal for spectroscopy. The frequencies of these atomic transitions fall within the span of the femtosecond laser frequency combs that we use as frequency dividers (described in detail in Section 2.1.2). These optical transitions are 657 nm for Ca, 578 nm for Yb, 282 nm for  $Hg^+$ , and 267 nm for  $Al^+$  (see Figure 2.1). Moreover, all these references are located in the same building as our Ti:S divider, and signals are received directly from these standards over optical fibers.

The trapping and probing methods of these atomic systems vary depending on the number of atoms and the atomic charge. Calcium and ytterbium are neutral atoms, allowing a large number of

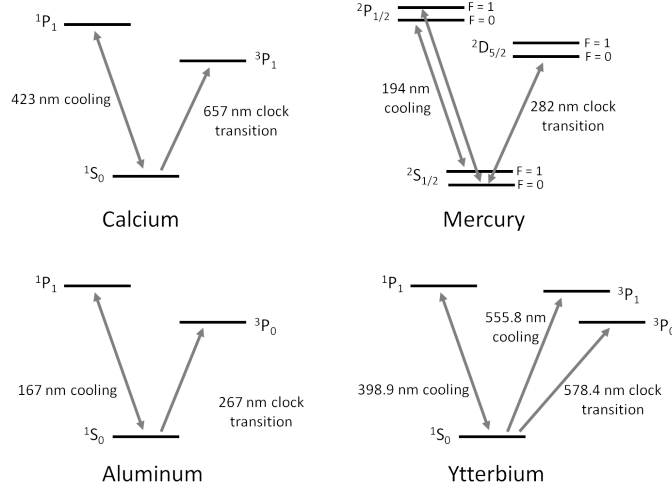


Figure 2.1: The partial level diagrams of cooling and clock transitions for calcium [49], mercury [50], aluminum [51], and ytterbium [52].

atoms,  $N$ , to be trapped, thereby increasing the signal-to-noise ratio and decreasing the instability  $\sigma_y$ . Problems with trapping and probing large numbers of atoms can be cleverly circumvented with different trapping and cooling methods [1][49][53][52]. Likewise, advanced methods for trapping and probing single ions such as  $\text{Hg}^+$  and  $\text{Al}^+$  have been developed [1][54][55][34].

Because the trapping and probing of atoms happens at longer timescales ( $> 1s$ ), the short-term stability of these systems are given by an optical reference cavity, which act as the local oscillator for the entire optical clock system. These are often Fabry-Perot (FP) cavities constructed with high-reflectivity, low-loss mirrors optically contacted onto a rigid spacer with a center bore (Figure 2.2). The high-reflectivity ( $> 99.999\%$ ), low-loss mirrors in these optical frequency reference cavities lead to a cavity finesse ( $\mathcal{F}$ ) of around  $10^5$  to  $10^6$  [56] and quality factor  $Q$  up to  $10^{11}$  [35][36]. Locking continuous wave (CW) lasers to a FP resonance has produced sub-Hertz linewidths at visible wavelengths with corresponding fractional frequency instabilities  $< 4 \times 10^{-16}$  at one second [35][33]. The whole cavity is temperature controlled and held in vacuum to maximize environmental isolation, improving overall stability [33]. The lock must also be incredibly stable, so a Pound-Drever-Hall servo is used to lock the CW laser to a single transverse and longitudinal mode of the cavity [57].

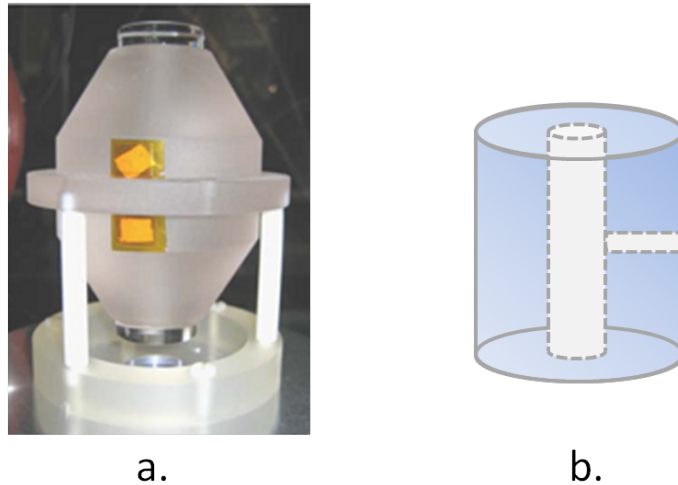


Figure 2.2: a. High-finesse, ultrastable ULE optical cavity in a vertical mounting configuration [36]. b. Schematic of ULE spacer with hollow bore.

Figure 2.3 shows the general scheme for an optical reference. With atoms trapped and cooled to reduce shifts and increase interrogation time, generating the optical atomic reference begins with spectroscopy of the preferred clock transition in the atom. A CW probe laser is locked to the optical cavity in order to resolve these very narrow linewidth transitions. The stabilized probe laser then excites the trapped atoms, and the resonance of the clock transition is detected with a photomultiplier tube. The resonance signal then feeds back to an acousto-optic modulator (AOM) which maintains the probe laser frequency near the atomic resonance. This servo typically operates within a timescale of one to ten seconds.

The resulting ultra-stable optical signal is then sent to a femtosecond laser frequency divider, which provides a phase-coherent link from the uncountable optical domain to the more accessible microwave region.

### 2.1.2 Femtosecond Laser Frequency Dividers

The use of an optical standard as a clock was previously limited by both the inability to electronically count optical cycles and the incredible difficulty of dividing the signal down to a manageable frequency [3]. However, demonstration of counting optical frequencies using a fem-

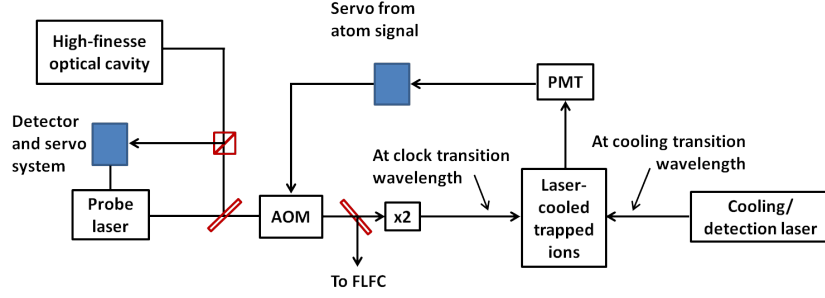


Figure 2.3: General schematic of an optical reference. The probe laser, which is stabilized to a high-finesse optical cavity, is frequency doubled and probes the clock transition of laser-cooled trapped atoms. The signal from the atoms feeds back to the probe laser through an acousto-optic modulator (AOM) to keep it on the atomic resonance.

to-second mode-locked laser in 1999 paved the way for this new technology [58][59][60].

The pulsed output of a femtosecond mode-locked laser gives  $N$  number of individual modes in the frequency domain, producing equally-spaced “comb” teeth (see Figure 2.4). The frequency of any given mode  $n$  is given by

$$\nu_n = n \cdot f_{rep} + f_0, \quad (2.2)$$

where  $f_{rep}$  is the repetition rate (the frequency difference between adjacent modes; the inverse of  $f_{rep}$  gives the period  $T$  between the pulses) and  $f_0$  is the carrier offset frequency. If these two parameters are simultaneously controlled, the resulting frequency comb is stable enough to be used as a divider for an optical reference. A schematic of the stabilization scheme for  $f_{rep}$  and  $f_0$  is shown in Figure 2.5 for the Ti:Sapphire frequency comb.

The carrier offset frequency  $f_0$  is due to the difference between group and phase velocities inside the laser, causing a phase slippage between successive pulses. In order to stabilize  $f_0$ , a group of modes around  $\nu_n$  is frequency-doubled and heterodyned with the  $\nu_m$  mode, where  $m = 2n$ . Mathematically, these two modes are given by:

$$2\nu_n = 2 \times (n \cdot f_{rep} + f_0) = 2n \cdot f_{rep} + 2f_0 \quad (2.3)$$

$$\nu_m = m \cdot f_{rep} + f_0 = 2n \cdot f_{rep} + f_0. \quad (2.4)$$

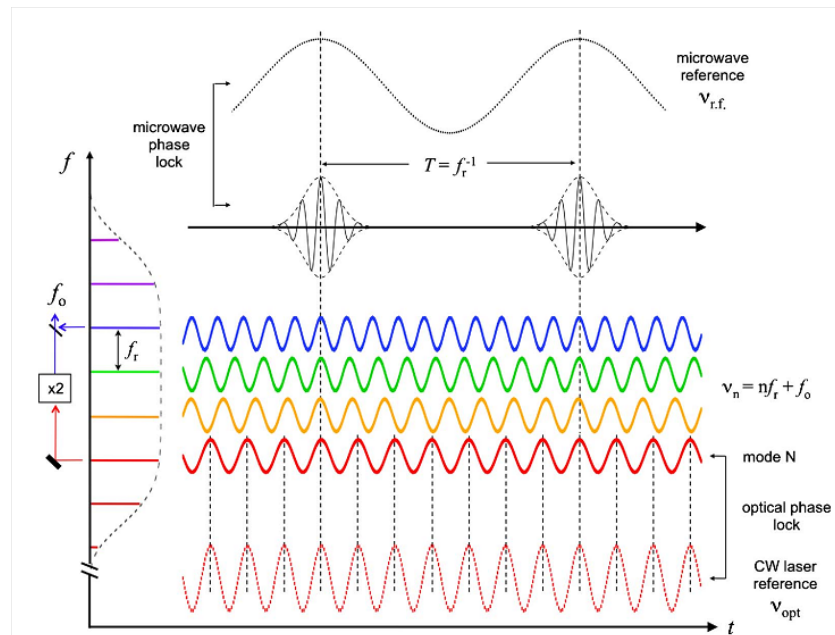


Figure 2.4: The pulsed output of a femtosecond mode-locked laser produces equispaced “comb” teeth [61].

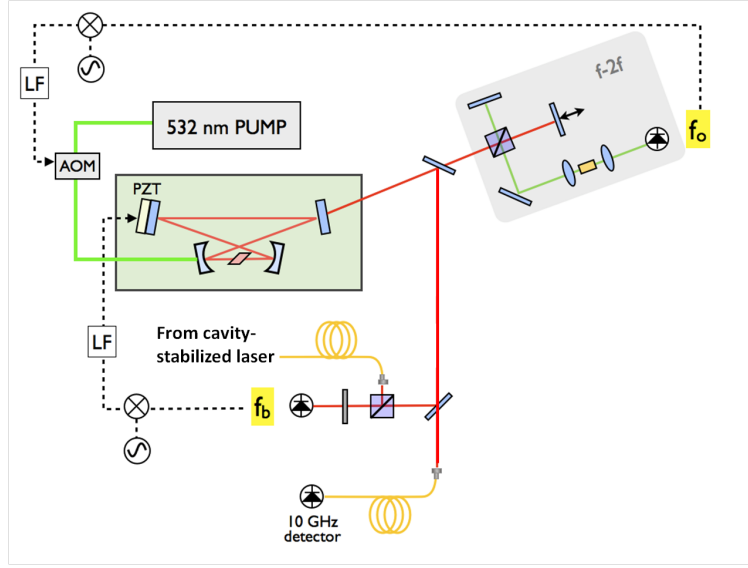


Figure 2.5: Stabilization scheme of a Ti:Sapphire ring laser. LF is loop filter.

The two are heterodyned, or subtracted, to access  $f_0$ :

$$2\nu_n - \nu_m = 2n \cdot f_{rep} + 2f_0 - 2n \cdot f_{rep} - f_0 \quad (2.5)$$

$$= f_0. \quad (2.6)$$

The resulting signal is fed back to an AOM to adjust the laser power and stabilize the offset. This method requires the mode-locked laser's output to span at least one full octave, and only a few femtosecond laser systems have achieved this to date [61]. The  $f$ - $2f$  method provides maximum phase noise reduction for optical-to-microwave division, but self-referencing with two-thirds of an octave, from  $2f$ - $3f$ , is possible with higher-order non-linearity [62][61].

The repetition rate  $f_{rep}$  can be controlled in a couple of ways. First,  $f_{rep}$  can be measured on a fast photodetector (bandwidth greater than the repetition rate) and phase-locked to a low-noise external microwave reference of the same frequency. Alternatively, it can be measured and controlled by phase-locking one tooth of the frequency comb with a CW laser, resulting in a beat frequency between them,  $f_b$ . If this CW laser is the output of the cavity-stabilized optical reference, the stability of the reference is transferred to every optical mode of the comb, since pulse formation via passive mode-locking enforces a constant relative phase among the laser modes [2][63]. The

equation describing the frequency of the comb lines then becomes

$$\nu_{opt} = n \cdot f_{rep} + f_0 + f_b \quad (2.7)$$

where  $\nu_{opt}$  is the frequency of the optical reference. Solving Eq. 2.7 for  $f_{rep}$  yields

$$f_{rep} = (\nu_{opt} - f_0 - f_b)/n. \quad (2.8)$$

Thus,  $f_{rep}$  represents the frequency-divided optical reference with  $f_0$  and  $f_b$  being small offsets. Since  $f_{rep}$  is determined by the cavity length, the stabilization is accomplished by feeding back the error signal of the locks to one cavity mirror that is mounted onto a piezoelectric transducer (PZT), thereby actively adjusting the cavity length.

The repetition rate can be measured by photodetecting the optical pulse train to generate a corresponding electrical pulse train. In the frequency domain, this train of electrical pulses is a series of discrete tones at harmonics of the pulse repetition rate, all, in principle, having the same fractional stability of the optical reference. Any harmonic of  $f_{rep}$  within the photodetector bandwidth can then be selected as a microwave source, thus completing the optical-to-microwave generation.

Reference [61] lists seven femtosecond mode-locked lasers that fit the criteria of octave-spanning self-referencing required for this application to date. Four of those lasers have been used for this purpose at NIST: Titanium:Sapphire (Ti:S), Erbium-doped fiber (Er:fiber), Yb:KYW, and Cr:forsterite. The research described in this paper focuses only on Ti:S and Er:fiber.

Ti:S-based frequency combs were the first combs to be spectrally broadened to an octave and self-referenced [64][6]. Three Ti:S lasers were used in this research; all are Kerr-Lens mode-locked, x-cavity ring lasers, depicted in Figure 2.5, giving a repetition rate of 1 GHz [65]. They are pumped with 8 W of 532 nm light, giving an output of around 1 W of mode-locked laser light. One laser uses  $2f$ - $3f$   $f_0$  stabilization [62] and has a spectral peak at 900 nm, and the other two are full-octave lasers using  $f$ - $2f$  stabilization with spectral peaks near 980 nm [65]. The laser spectrum of one of the two octave-spanning Ti:S lasers is shown in Figure 2.6. The spectra of these lasers span

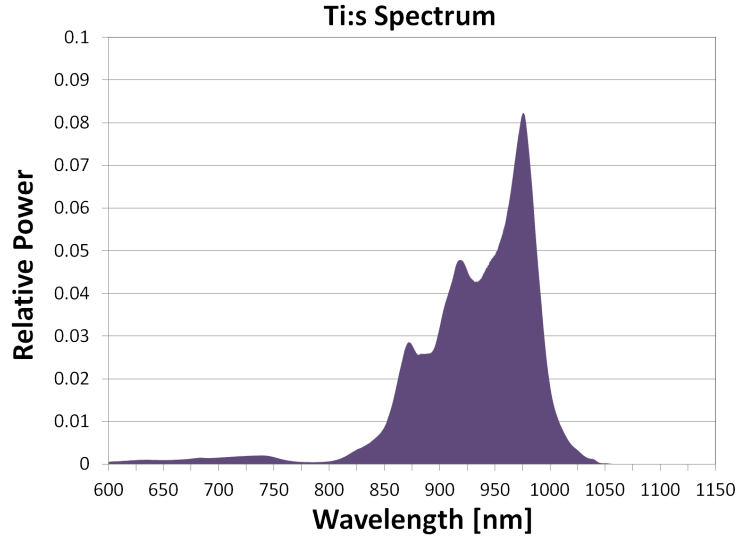


Figure 2.6: Spectrum of  $f$ - $2f$  Ti:S laser with spectral peak near 980 nm.

the range of frequencies given by the optical references described in Section 2.1.1, allowing any of them to be used as the basis for optical-to-microwave conversion. While a higher repetition rate of 1 GHz will prove to be beneficial in terms of noise, the Ti:S requires a very large, powerful, and expensive pump laser at 532 nm, making it less efficient and portable for some applications.

Fiber-based laser systems, such as the Er:fiber lasers used here, are passively mode-locked ring lasers pumped by diode lasers [66][67]. With center wavelengths in the telecom range of 1550 nm, Er:fiber also has the benefit of using common, off-the-shelf parts and being more robust. Low power and fiber components make fiber lasers much less expensive to run than the Ti:S. However, fiber-based systems typically have lower repetition rates; the Er:fiber lasers used in this work have  $f_{rep} = 200$ - $250$  MHz. Scaling the repetition rate to 1 GHz with a fiber laser is possible, yet challenging [68][69][70][71]. Again, this will have important implications when we discuss sources of noise in the optical-to-microwave process.

One Er:fiber laser used in this work is a commercial femtosecond laser made by Menlo Systems. The M-Fiber laser product has a repetition rate of 250 MHz and an average output power of  $> 400$  mW, and it is self-modelocking with microcontrollers and a computer control system. This is the primary laser used for photodiode characterizations at 1550 nm. Another Er:fiber laser used

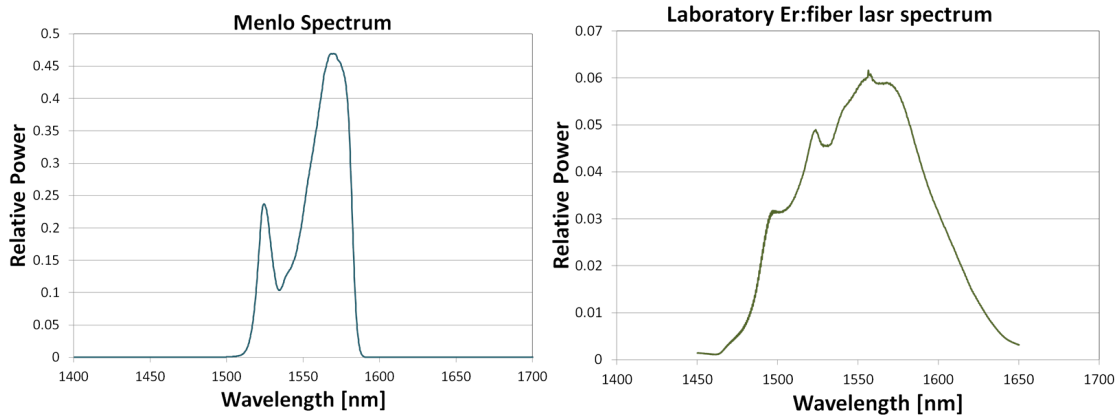


Figure 2.7: Frequency spectra of 1550 nm Er:Fiber lasers used in this work.

in this work was built in our laboratory; it has a 200 MHz rep-rate and  $\sim 70$  mW average output power [67]. This laser was used in some measurements of phase noise. The spectra for these two lasers are shown in Figure 2.7.

### 2.1.3 Photodetectors

The final phase of the optical-to-microwave conversion process is the conversion of an optical signal into an electronic signal using a photodetector. The photodetectors used here are semiconductor devices operating in the 980 nm and 1550 nm wavelength ranges of the femtosecond lasers. Most of the time, commercially available, prepackaged units with fiber pigtailed for input optical signal and microwave connectors for the output are used for work with microwave generation. Some important criteria for these devices are their bandwidth and their power handling. Since we are interested in generating signals in the 10 GHz range, the bandwidth, or speed, of the photodiode must be greater than that. Typically we use devices with a bandwidth of 12 GHz and above. An average device might generate around -10 dBm of output power and 10 mA of photocurrent. However, some state-of-the-art photodiodes tested in this work feature higher power handling, up to 15 dBm or more and over 15 mA of photocurrent, with optimal operating conditions. Some of these are special packaged, commercial devices, and some are still in development in the lab, unpackaged wafers that must be coupled to and probed directly from the chip. Greater detail about

the specific devices used in this work is presented in the next chapter.

Within the photodetector, the optical pulse train is mixed/beat together, producing a corresponding electronic pulse train. In the frequency domain, this produces another comb, a series of discrete tones at harmonics of the pulse repetition rate with the first tone at the repetition rate of the laser (see Figure 1.1). For example, a 1 GHz pulse train coming out of the Ti:S laser will produce tones at 1 GHz, 2 GHz, 3 GHz, and so on, after photodetection. For the Er:Fiber input, the resulting comb teeth are at 250 MHz, 500 MHz, 1 GHz, 1.250 GHz, etc. The comb will continue up to the bandwidth of the photodiode and will then taper off (as seen in Figure 1.1).

The ultimate generation of a microwave signal is achieved by using an electronic bandpass filter to pick out the desired frequency. In this work, the frequency of interest is 10 GHz; however, in principle one could generate a signal as low as 250 MHz and as high as  $\sim 20$  GHz (given the bandwidth of our fastest photodiodes used in this research (see Section 3.2.1)). Most importantly, by locking to the femtosecond frequency comb and photodetecting the output, the optical frequency is now an accessible microwave signal.

Compared to the complexity of the optical frequency reference and femtosecond laser frequency comb systems, photodetection of this ultimate stable signal seems like the most straightforward operation. Surprisingly, however, it is actually the significant source of noise in the optical-to-microwave scheme. The noise limitations of the other parts of the system have been carefully studied over the years and reduced as much as possible, but photodetection in this context has not been thoroughly characterized until very recently. In the next section, the noise limitations of each system will be discussed, and we will show how photodetection noise has now become the primary concern for the generation of low phase noise microwaves using this technique.

## 2.2 Noise Limitations

The noise limitations of the optical-to-microwave scheme are discussed in the following sections.

### 2.2.1 Optical Reference Noise

The atoms in an optical frequency reference provide the long-term ( $> 1$  s) timing stability desired for an actual clock signal; however, trapping and probing of atoms is noisy and makes the short-term stability insufficient for low-phase noise signals, which are measured on time scales less than one second. Therefore, as mentioned in Section 2.1.1, the CW laser locked to a Fabry-Perot reference cavity is used as the actual optical frequency reference for this application. The FP cavities are constructed of two parallel, highly reflecting mirrors, and the frequency of the cavity is given by the distance between the two mirrors. Refractive index changes in air can also cause shifts in the resonance. Therefore, to maintain a highly stable frequency, careful attention to environmental isolation is required to keep the cavity length fixed.

The highly reflective mirrors are mounted to a rigid spacer with a longitudinal bore, as shown in Figure 2.2b. These spacers are blocks of material such as ultra-low expansion (ULE) glass, with a coefficient of thermal expansion (CTE) on the order of  $10^{-8}/\text{K}$ . The temperature excursions of the cavity are usually held constant to a few mK over a period of one day [35][33][72][36]. The level of temperature control can be relaxed somewhat if the cavity temperature is set to a point where the CTE passes through zero [73][33][72]. In this case, the sensitivity to temperature changes of a few Hz/mK ( $10^{-14}/\text{mK}$ ) has been reported [72]. Even the laser's relative intensity noise (RIN) must be stabilized to reduce thermal instabilities of the cavity length due to heating of the mirrors.

Cavities must be held in vacuum to eliminate shifts in resonance caused by refractive index changes in air. Acoustic and seismic isolation is achieved with sound damping enclosures and isolation platforms, as well as mounting designs that exploit cavity symmetry to further reduce vibration sensitivity [74][75][36][73][76]. In a laboratory environment, vibration sensitivity can be reduced to near the fundamental noise set by Brownian motion of the cavity [73]. New cavity designs, as well as real-time measurement and cancellation of vibration noise, are also being pursued toward enabling Hz-level linewidth optical references beyond a laboratory setting [77][78].

With environmental effects taken into consideration, the fundamental stability limit of the

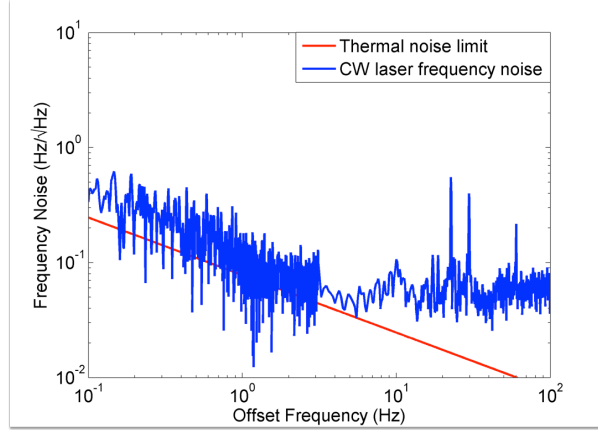


Figure 2.8: Frequency noise spectrum for the CW laser in the Ytterbium lattice clock (blue) compared to the theoretical estimate of the thermal noise limit (red).

cavities becomes Brownian thermal mechanical fluctuations in the Fabry-Perot cavity mirrors [33]. Thermal fluctuations in the mirror material can make tiny, yet significant, changes to the cavity length. Choice of length of the cavity and spot size on the mirrors all affect the Brownian noise limit. The thermal noise limit decreases for longer cavities, since thermally-induced mirror displacements represent a smaller fraction of cavity length; also, a larger spot size on the mirror is advantageous, since mirror displacements are averaged over a larger area. Mirror material, including anti-reflection coatings, plays a significant role as well [79]. Figure 2.8 shows a frequency noise spectrum for the CW laser compared to the theoretical estimate of the thermal noise limit for the reference cavity to which the 578 nm Yb clock light is stabilized.

The phase noise of the CW laser is also determined by the fidelity of the Pound-Drever-Hall (PDH) lock to the cavity [57]. For time scales 1 s and longer, it is relatively straightforward to lock the laser to be cavity-limited. For the shorter time scales considered for ultra-low phase noise microwaves, noise in the PDH locking servo has a significant contribution to the phase noise of the CW laser. Technical noise sources, such as noise from in-loop electronic amplifiers, residual amplitude modulation, and remaining laser RIN at the PDH modulation frequency often limit performance [33][74][36][72][73].

Limited by fundamental thermal fluctuations in the cavity and the lock to the CW laser, the

phase noise on the optical carrier has potential for extraordinarily low noise, and illustrates the power of this approach. A comparison of two CW lasers stabilized to independent reference cavities with a PDH lock can achieve phase noise of -103 dBc/Hz at 1 Hz, scaled to 10 GHz.

### 2.2.2 Femtosecond Laser Frequency Divider Noise

One fundamental source of noise inside a femtosecond frequency divider is noise on the optical pulse trains themselves. Recent experiments using all-optical techniques have analyzed the timing jitter on pulses out of Ti:S and Er:fiber lasers [37][38]. The outputs of two phase locked, nearly identical lasers are combined then compared in two arms using a balanced optical cross-correlator; this technique compares the temporal overlap of the two signals to determine the phase error between the pulse trains. This all-optical method is not limited by photodetector noise such as shot or thermal noise, as will be described in Section 2.2.4, and so represents only fundamental noise on the optical pulse train. For Ti:S, a timing error of less than 13 as was demonstrated from d.c. to 41 MHz, the Nyquist frequency of the pulse train, corresponding to -203 dBc/Hz phase noise above 1 MHz when scaled to a 10-GHz carrier [37]. In Er:fiber from 10 kHz to 38.8 MHz, timing jitter is 70 as with phase noise of -200 dBc/Hz at 10 MHz scaled to a 10-GHz carrier [38]. While timing jitter is lower for Ti:S lasers than Er:fiber lasers due to their much shorter pulse width, both are below the fundamental noise limits of photodetection, as we will see, making this less of a substantial problem when considering the full optical-to-microwave generation process.

Two other significant sources of noise in the femtosecond laser frequency divider are fluctuations of  $f_0$  and  $f_b$ . The offset frequency  $f_0$  is particularly sensitive to amplitude noise, which is a prominent characteristic of the pump laser. The offset frequency can be stabilized using a phase lock to control the fluctuations of the laser pump power; feedback to an AOM in the laser pump beam or to the laser pump current can yield hundreds of kHz of bandwidth. Unenclosed beam paths and pump laser beam pointing instability cause index fluctuations, also resulting in noise on  $f_0$ . Instabilities of the laser cavity length contribute to noise in  $f_b$ . In free-space lasers like Ti:S, slow drifts in the laser cavity length are minimized by temperature stabilization of the

laser baseplates, but residual noise in  $f_b$  is also caused by seismic and acoustic disturbances of the laser cavity as well as coupling of pump-induced amplitude noise to phase noise inside the laser. For both  $f_0$  and  $f_b$ , the fidelity is ultimately limited by the signal-to-noise (SNR) on the detected signals.

Other significant noise sources in the femtosecond frequency divider can be challenging to eliminate. While amplitude fluctuations of the pump laser can be subdued with a phase lock, we will show in later chapters how these amplitude fluctuations lead to significant noise due to the photodetector. Amplified spontaneous emission (ASE) is a fundamental source of noise in the pump laser. Femtosecond lasers with high intracavity power and short pulses, such as Ti:S and solid-state lasers with lower cavity losses, will have less ASE than a fiber-based laser with losses sometimes exceeding 50% [61].

Outside of the laser itself, another source of noise is non-linear fibers used to spectrally broaden the signal to achieve an octave-spanning spectrum in the Ti:S laser [61]. These fibers, such as microstructure fiber or highly-nonlinear fiber, amplify both the technical laser noise and the ASE in the outgoing signal.

### 2.2.3 Fiber Link Noise

In most cases, the optical frequency reference is not sitting next to the frequency divider; therefore, transmission of the optical reference signal is through some length of optical fiber. For systems located more than a few meters apart, the phase noise of the signal is degraded by path length fluctuations that cause Doppler shifts in the transmitted signal, so stabilization of the fiber path length is necessary to maintain the integrity of the signal.

Considerable effort has gone into phase-stabilized fiber links for both CW optical and modulated optical (for microwave distribution) signals [80][81][82][83][84]. The schematic for connecting to a CW optical reference is shown in Fig. 2.9. The phase of the optical frequency reference before entering the fiber is compared to the phase after one round trip. This information is acquired by reflecting a small amount of light from the frequency divider end back through the fiber path.

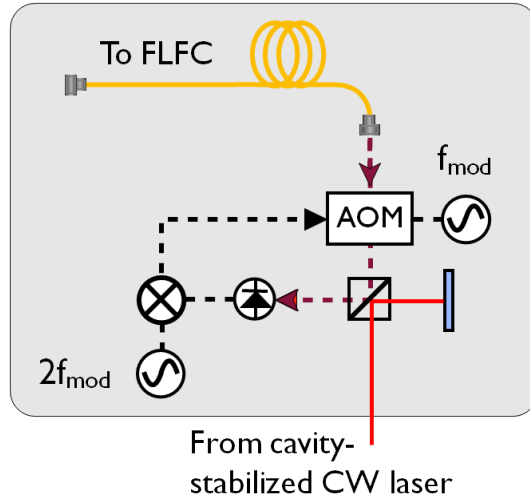


Figure 2.9: Schematic of phase-stabilized fiber link from cavity-stabilized CW laser to femtosecond laser frequency comb.

Phase comparison is performed with a Michelson interferometer where the fiber link forms one arm, referenced against a short free-space path. A photodetector at the interferometer output generates an error signal, which is used to shift the phase of the transmitted signal via an AOM.

While km-long fiber links can be stabilized to a level that can satisfactorily transmit lasers for optical clock comparisons, this method may degrade the phase noise of a derived microwave signal. For example, [81] reports a 7 km link instability of  $< 10^{-17}$  at one second, more than an order of magnitude lower than the best optical references shown to date. However, the residual phase noise at 1 kHz offset of this same signal (appropriately scaled to 10 GHz) is higher than the residual phase noise of our frequency combs and photodetectors, thus would limit the phase noise of the generated microwave signal. In the work presented here, optical frequency references and femtosecond dividers are separated by tens or hundreds of meters of optical fiber, so the resulting signals meet the desired criteria of low noise.

#### 2.2.4 Photodetector Noise

Ideally, the conversion from a photon into an electron inside a semiconductor photodiode is a one-to-one, or linear, process; that is, one photon will generate one corresponding electron

within the normal time response of the material. However, as we will see in detail in Section 4.2, a photodiode is neither 100 % efficient nor proportionally linear; photons coming in might not enter the semiconductor or generate an electron at all, or the time delay may increase as the number of photons increases. Various micro- and macroscopic processes at the semiconductor level disrupt or interfere with this conversion and lead to a power dependence of the optical to electronic process. While there are many effects inside the material, we will consider in depth three distinct noise sources that cause fluctuations in the timing of the detected pulse: thermal noise, shot noise, and amplitude to phase conversion.

Thermal noise (often referred to as Johnson or resistive noise) is associated with random fluctuations of the current across resistive elements of the photodetection circuit (e.g., the load resistor of the photodiode) [85][86]. It is a white noise process, meaning it is essentially flat across the frequency spectrum. Shot noise is related to the randomness of the incident photon stream [87][88]. Like thermal noise, it is a white noise process, and due to the random nature of photons, it is a fundamental limit for an optical process. Within the system we are exploring, shot noise dominates over thermal noise as optical power, and the photocurrent, increases.

Amplitude-to-phase conversion is an observed effect where amplitude noise on the signal incident on the photodiode is converted into phase noise on the outgoing signal [45][89][81]. Considering the above-mentioned prevalence of amplitude noise on the pump laser of the frequency divider, this is a critical effect on the overall stability of an optically-generated microwave signal.

While the noise limitations in the optical reference and femtosecond frequency divider are generally understood and are being improved, noise due to photodetection has become a primary concern as this optical-to-microwave method of generating low noise signals has developed. Understanding and reducing the effect of photodetector noise will play a key role in the viability of this method. In the next few chapters, these noise effects will be described in more detail and systematically characterized in the context of the optical-to-microwave generation process.

## Chapter 3

### Semiconductors, Photodetection, and Devices

Photodetection can be a significant source of noise in the optical-to-microwave conversion process, yet because of the apparent simplicity of converting photons to electrons its importance has often been overlooked. However, in order to achieve unprecedented low phase noise signals at 10-GHz via optical to microwave frequency division, it is necessary to address the issue of photodetector noise in depth. This thesis will show that a thorough characterization of photodetector noise limitations allows the construction of a state-of-the-art, low noise photonic oscillator by choosing photodetectors that have the best (lowest) noise performance in the desired operating regime. The results can also be used by photodiode manufacturers to aid development of the next generation of photodetectors for this and similar applications.

In order to strategically construct new or choose existing photodetectors with the desired noise performance, it is important to have a basic working model of a semiconductor photodiode and the primary noise processes that arise from them. A basic semiconductor model is presented below, and the basic noise processes discussed in this thesis will be connected to this model in Chapter 4.

#### 3.1 Introduction to Semiconductors and Photodiodes

Conductors are materials, like metals, where electrons flow freely through the material; this is due to the loose bonding of the valence electron to the rest of the atoms in the metal. Conversely, insulators inhibit the flow of electrons, as they are more tightly bound in their energy states in the

atoms.

A semiconductor is a crystalline or amorphous solid with conductivity somewhere between that of a conductor or insulator. The conductivity of the material can be changed by temperature, by illuminating it with light, or by doping of the original material with other elements. Silicon (Si) is the primary semiconductor material; however, other materials such as germanium (Ge) and gallium arsenide (GaAs) are often used depending on the application [90].

An individual atom has discrete energy levels that are filled with electrons. However, in proximity to a great number of atoms, such as in a solid, the fields of the individual atoms begin to interact with each other. Electrons in the lowest energy levels are shielded from the external effects of other atoms and maintain their energy levels; however, the highest energy states of all the atoms broaden into many closely spaced discrete levels that form energy bands. Likewise, valence electrons are no longer bound to one particular atom but are held within and move between these energy bands based on their energy [91].

The two energy bands within a semiconductor are the valence band and the conduction band. The conduction band is the higher energy band, and the valence band is below it. These two bands are separated by an energy bandgap ( $E_g$ ). This bandgap energy differs by material; notably, for Si,  $E_g = 1.11$  eV ( $\lambda = 1.15 \mu\text{ m}$ ), and for GaAs,  $E_g = 1.42$  eV ( $\lambda = 0.87 \mu\text{ m}$ ) [90].

At the temperature of absolute zero, all quantum states in the valence band of a semiconductor are completely filled with electrons with none in the higher conduction band. As the temperature increases, some electrons are thermally excited into available quantum states in the conduction band [91]. This electron becomes a mobile charge carrier, free to drift through the material. Likewise, the absence of an electron in the valence band leaves an empty state called a “hole.” Since electrons in the valence band are able to move in and out of this new available state leaving another empty state behind, a hole can be thought of as a positive charge carrier analogous to the electron, free to drift through the valence band [90].

Introducing small amounts of other materials (called dopants) into the crystalline structure of another semiconductor material can dramatically change the properties of the semiconductor.

A doped semiconductor is called extrinsic. An n-type semiconductor is one that is doped with materials with excess valence electrons, or donors, giving a predominance of mobile electrons. Similarly, a p-type semiconductor is one with dopants having few valence electrons, called acceptors, generating a predominance of holes. Undoped semiconductors are called intrinsic materials [92].

### 3.1.1 P-N and P-I-N Junctions

When differently doped semiconductor materials are placed in contact with each other, the corresponding junction can change the functionality of the material by influencing the distribution and movement of charge carriers in the semiconductor [93]. One of the most important junctions for optical and photonic applications is the p-n junction, where a p-type material is placed in contact with an n-type material. A depiction of the behavior of electrons and holes in a p-n junction is shown in Figure 3.1. The electrons in the n-type region diffuse toward the holes in the p-type region and recombine with a hole, leaving behind positively charged ionized donor atoms in the n- region near the boundary. Conversely, the holes in the p-type region diffuse toward the electrons in the n-type region and recombine with an electron, leaving behind negatively charged ionized acceptor atoms in the p-region near the boundary. This region around the boundary left with fixed charged ions and practically no mobile charge carriers is called the depletion region. The thickness of the depletion layer in each region is proportional to the concentration of dopants in the region; that is, if the doped region is very highly doped, the depletion layer is very thin. If the doped region is very lightly doped or an intrinsic material, the depletion layer is very wide.

Due to the fixed positive and negative charges within the depletion layer and on either side of the boundary, a fixed electric field is generated between the p- and n- regions [93]. A corresponding potential difference  $V_0$  is also induced, resulting in the p-type region being at a higher potential than the n-type region. This shifts the valence and conduction bands for each region; within the depletion region, there is a “bending” of the energy levels from one region to another (see Figure 3.2).

As more mobile carriers diffuse and recombine in the depletion region, the electric field grows

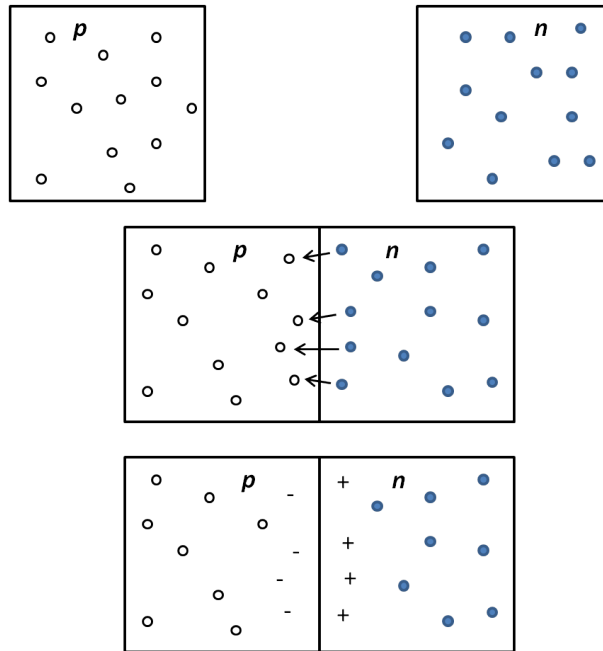


Figure 3.1: A depiction of electron and hole recombination in a p-n junction. White dots represent holes, blue dots represent electrons.

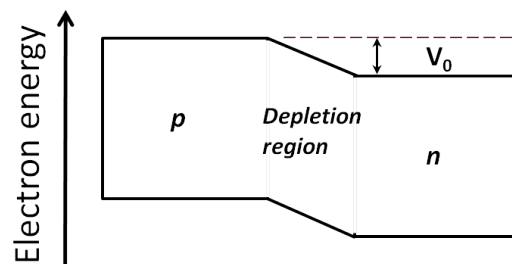


Figure 3.2: The bending of energy levels between the p-type and n-type regions.  $V_0$  is the induced potential difference.

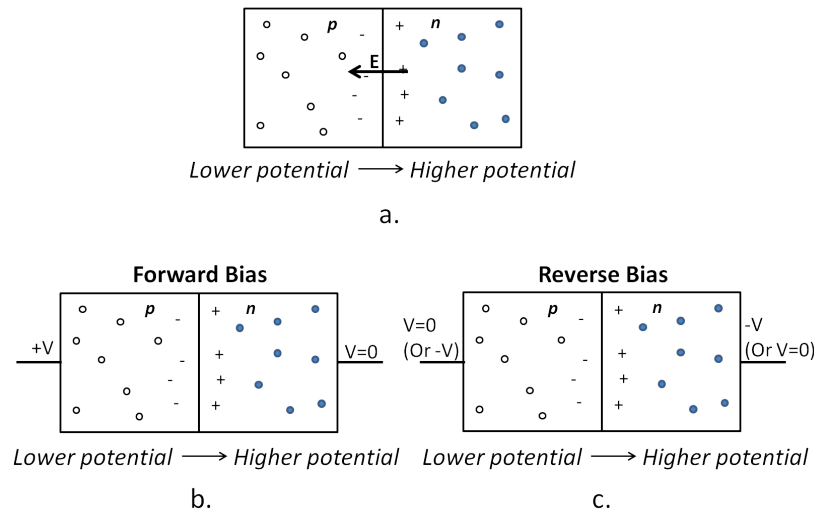


Figure 3.3: a. The intrinsic electric field in the intrinsic region. b. Forward biasing of the p-n junction allows current to flow across the junction. b. Reverse biasing of the p-n junction reinforces the internal voltage bias, impeding the flow of majority carriers.

stronger in magnitude. Mobile electrons in the n-type region and mobile holes in the p-type region are forced to stay in their region by the opposing  $E$  field and potential difference (Figure 3.3(a)). In this state, no net current flows across the junction.

In order to force current across the junction, an external potential difference, or bias voltage, and a resistor can be applied across the junction. Forward biasing applies a positive potential to the p-region, counteracting the intrinsic potential difference from the internal electric field from the depletion layer (Figure 3.3(b)). The decrease in the potential energy level across the junction allows current to flow again across the boundary (electrons flowing from higher to lower potential or from the p-region to the n-region). Reverse biasing applies a negative potential to the p-region, reinforcing the internal potential difference from the internal electric field, impeding the flow of majority carriers (Figure 3.3(c)). Essentially, a p-n junction acts like a diode, allowing current flow through the forward direction and blocking current in the reverse direction.

Because the relative shape of the depletion region, the location of the charges on either side of it, and the corresponding electric field, the junction of the p-n diode can be roughly modeled as a parallel plate capacitor. If  $A$  is the area of the junction,  $\ell$  the width of the depletion layer,

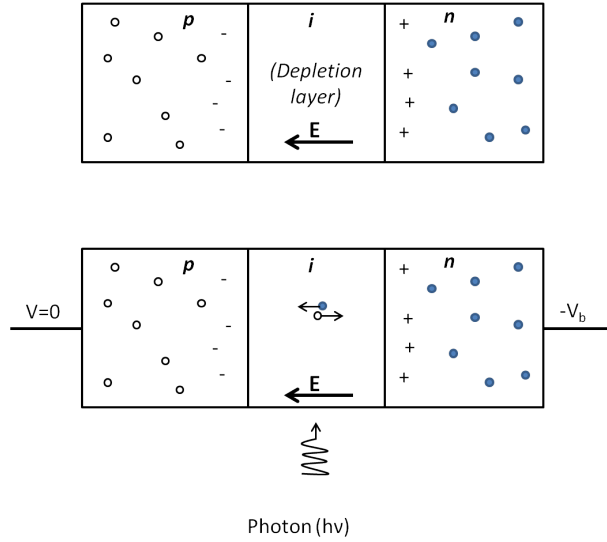


Figure 3.4: A depiction of the p-i-n junction and the generation of an electron-hole pair in the intrinsic region.

and  $\epsilon$  the permittivity of free space, then the capacitance  $C$  is given by  $C = \epsilon A / \ell$ . Moreover, the thickness of the depletion layer,  $\ell$ , increases with increasing reverse bias, thus also decreasing the capacitance [93]. This is important because a reduced capacitance and shorter  $RC$  response makes for faster response of charge carriers inside the diode to an external perturbation, such as a photon [93] [94].

A p-i-n junction, shown in Figure 3.4, is very similar to the p-n junction [93]. The p-type region is separated from the n-type region by a layer of intrinsic or very lightly doped material. Due to the inversely proportional relationship of the depletion layer thickness to the doping concentration, the depletion layer in a p-i-n semiconductor extends very far into the intrinsic region from both sides. A greatly expanded depletion layer will have multiple benefits when we consider these semiconductor devices as photodetectors. By adding this intrinsic layer, junction capacitance decreases and response time decreases, which is beneficial when using p-i-n semiconductors as photodiodes [95]. However, if the depletion layer is too thick, the response time eventually increases; therefore, a balance in construction of the diode must be found to optimize response time [96].

### 3.1.2 Photodetector Parameters

P-N and p-i-n semiconductors work well as diodes within a circuit. However, the way that their mobile charge carriers interact with light makes them powerful tools for photodetection. Before we discuss specific structures of the photodiodes, however, there are a few important parameters that describe their performance. Modifications to design and structure are made to most efficiently optimize as many of these parameters as possible for a given application.

Quantum efficiency,  $\eta$ , is the probability that a single photon incident on a semiconductor will generate an electron-hole pair [97]. More generally, however,  $\eta$  describes the ratio of incident photons (photon flux,  $\Phi$ ) to the generated electron-hole pairs contributing to photocurrent; therefore, it describes how well the photodiode converts photons into current-inducing electrons. Quantum efficiency is also wavelength dependent, as a semiconductor material has different absorption properties for different wavelengths of light.

Responsivity,  $\mathcal{R}$ , is the ratio of generated photocurrent to the incident optical power; it has units of amps per watt [A/W]). This is evidently related to quantum efficiency, since not all photons contributing to incident optical power will generate electron-hole pairs. Its relationship to quantum efficiency means that it is wavelength dependent as well. A device optimized for high responsivity at 1550 nm will most likely have lower responsivity at 980 nm, as will be demonstrated in Section 3.2. Loss of incident optical power through coupling, reflection, and diode size will also reduce  $\mathcal{R}$ . Likewise, reduction of electronic signal power at the output of the diode due to cable loss can reduce the measured photocurrent, thereby reducing the calculated responsivity if not accounted for. Sometimes, anti-reflection coatings for particular wavelengths will be used to minimize reflected light and increase responsivity and quantum efficiency.

No photodetector is fast enough to respond to the oscillations of a light field; rather, the response of photodiodes is to the average power of the incident light. The bandwidth, or speed, of the diode refers to how fast the diode responds to modulations of the power. The bandwidth of the detector is directly related to response time of the diode, which, as described in the previous

section, relates to the  $RC$  time constant of the circuit and the velocity of the charge carriers within the semiconductor material.

The size and dimensions of the diode—the cross-sectional area and the width of the depletion layer—affect the overall capacitance and the  $RC$  time constant. A smaller active area results in a smaller junction capacitance and reduced  $RC$  time constant, leading to increased response time and a faster diode. However, this also means a reduction in collected light. A wider depletion region collects more light but has a slower response time due to the time it takes charge carriers to move across the region. In the presence of the intrinsic electric field  $E$  inside the intrinsic region, a charge carrier has a mean drift velocity of  $v = \mu E$ , where  $\mu$  is the carrier mobility, which characterizes how fast the carrier can move through the semiconductor material [97]. For a depletion layer of width  $w$ , the transit time is  $w/v$ . For photodiodes with bandwidths of tens of gigahertz, typical response times are in the tens of picoseconds [97].

When the diode is reversed biased yet with no incident light, there are still charge carriers inside the material that can generate a current. This is called the dark current. While generally small, it is sometimes necessary to calibrate the photocurrent by subtracting the dark current.

Photodiodes are considered to be linear devices over a broad range of operation; that is, as the incident optical power increases, the corresponding generated photocurrent increases the same amount. On an atomic level, this means that as the number of incoming photons increases, charge-carrying electrons in the depletion region continue to be generated and move across the drift region at the same rate. However, this process is not infinitely sustainable; eventually, either the charge carriers will drift too slowly or the influx of photons will create so many charge carriers that the resulting density of charges in the drift region (called the space charge) produces its own electric field counteracting the intrinsic and bias-generated fields, slowing the motion of the charge carriers. This “space-charge screening” effect leads to saturation, where incident optical power continues to increase while the photocurrent stays the same or increases at a greatly reduced rate. This effect greatly contributes to noise in the detection of short optical pulses, and we will discuss saturation and noise in much greater detail in Chapter 4.

### 3.1.3 P-N and P-I-N Semiconductor Photodetectors

Most semiconductors exhibit the internal photoeffect; that is, when photons of sufficiently high energy are incident on the semiconductor material, the energy of the photon dislodges an electron from the valence band and excites it to the conduction band where it becomes a mobile charge carrier [98]. This process also generates the corresponding hole in the valence band. In the presence of an applied electric field, this mobile electron moves within the material, thereby inducing an electrical current in a circuit surrounding the semiconductor [98]. In this way, a semiconductor can be used as a photoelectric detector to convert a light signal into an electronic signal.

The properties of the p-n and p-i-n diodes make them particularly useful for photodetection. When reverse biased, there is no net current in the diode, neglecting dark current. When a photon impinges on either the p- or n-regions of the diode, an electron-hole pair is generated; however, they can only randomly drift in the region and eventually recombine, contributing no current [95]. However, if the photon is absorbed in the depletion layer, the generated electron and hole move under the influence of the intrinsic electric field. Thus a photocurrent is generated. Since a p-i-n diode has a much larger depletion region than a p-n diode, more light can be captured and converted into photocurrent [95].

Figure 3.5 shows the energy band structure of a p-i-n photodiode. Electrons and holes are generated in the intrinsic region; holes occupy the valence band below and electrons occupy the conduction band above. Both diffuse in accordance with the net electric field and corresponding energy levels. However, electrons drift faster than holes within the electric field [96]; the slow drift of the holes increases response time of a p-i-n diode and also saturation, an effect we introduce in the next section.

One could shine light perpendicularly to the diode and directly on the intrinsic region of a p-i-n diode to reduce transit time of electrons across the depletion region; however, quantum efficiency decreases in this configuration due to effects like reflection off the surface and electron-hole recombination near the surface [97] [94]. Often, to avoid this issue, a diode is p-side-illuminated

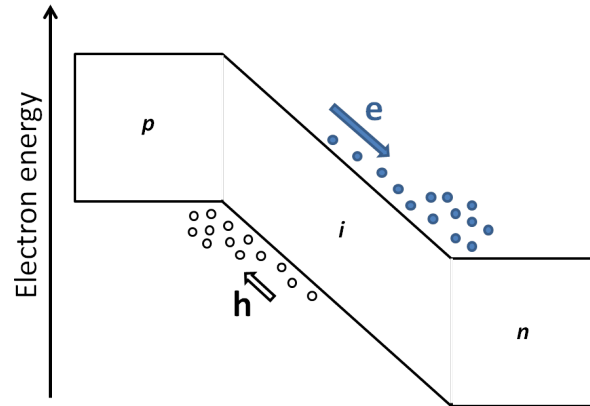


Figure 3.5: Energy band diagram of a p-i-n junction and the diffusion of electrons and holes in the intrinsic region.

(sometimes called top-illuminated); that is, the incident light is sent through the p-type region to be absorbed in the depletion layer. This device structure works if the absorption length of the light is longer than the width of the p-type region; otherwise, carriers created in the p-region recombine without contributing to the photocurrent. Also, an anti-reflection coating is sometimes applied to the illuminated side to optimize absorption at a certain wavelength.

### 3.1.4 Photodiode Structures

Given the basic p-n and p-i-n photodiode structure, there is a vast array of modifications that can be made to develop a photodetector optimized for a given application. The subset of devices capable of converting femtosecond laser pulses into a train of electronic pulses separated by frequencies on the order of a gigahertz is of interest to this work, primarily those with high bandwidth ( $>10$  GHz), higher power handling, and improved saturation. In order to characterize common noise properties of interest in this regime, we have focused on two different device structures for these measurements: dual-depletion region (DDR) InGaAs/InP p-i-n detectors and uni-traveling carrier (UTC) InGaAs/InP detectors. The DDR photodiodes are manufactured by Discovery Semiconductors, Inc. (DSC), and the UTC diodes were developed in the group of Prof. Joe Campbell in the Department of Electrical and Computer Engineering at the University of Virginia (UVA).

The basic designs of these two types of devices are described below.

### 3.1.4.1 Dual-Depletion Region Photodetectors

The Discovery Semiconductor photodiodes examined in this work share a basic dual-depletion region design optimized for operation around 1550 nm and 10 GHz [99][96]. In the basic p-i-n structure discussed above, the p- and n-type regions are separated by a single intrinsic layer forming the majority of the depletion region. Electron-hole pairs generated in this region drift under the influence of the bias-induced electric field to opposite sides of the junction. With increasing incident optical power, more charge carriers are generated inside the drift layer, leading to saturation as described above. The DDR structure uses two internal layers: one InGaAs absorption layer and a transparent InP drift layer. Photons travel through the p-type cap layer and generate electron-hole pairs in the absorption layer. Since the holes drift toward the p-type region, they must only travel across the absorption layer; therefore, their slowness is accounted for by the decreased transit distance. The electrons can then flow across the drift region at a higher velocity, and the total transit time in the device is optimized and the space-charge distribution is spread out to decrease saturation [96].

A schematic of the top-illuminated DDR structure is shown in Figure 3.6. The “mesa” shape of the diode minimizes the junction capacitance by reducing the cross-sectional area of one “plate” of the capacitor, thus also increasing the speed of the device [100]. However, since faster transit time requires a thinner intrinsic layer, these two parameters must be optimized for best response time for a given application (see Ref. [96]). A 5  $\mu\text{m}$  wide p+ metal ring contact sits on top of the cap layer to provide electrical contact to the diode. The diameter of the active area onto which the photons are incident varies between 30 and 60  $\mu\text{m}$  for these devices. The width of the total depletion region is 2.5  $\mu\text{m}$  [100]. To reverse bias these photodiodes, a positive voltage, typically 7 V or 9 V, is applied to the electrical contacts through external pins on the photodiode package.

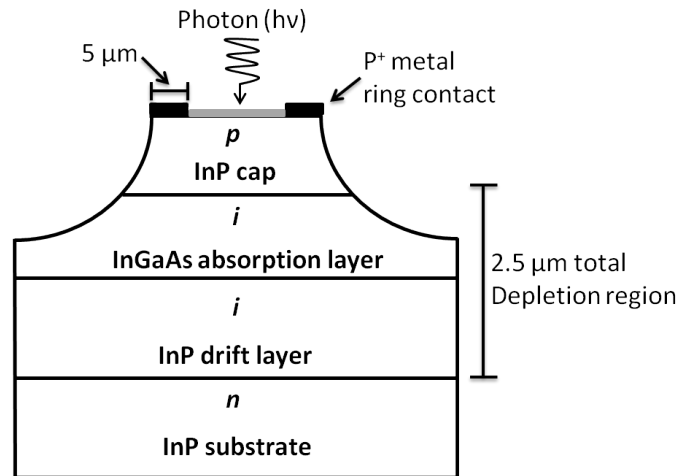


Figure 3.6: Schematic of mesa-shaped, top-illuminated DDR photodiode.

### 3.1.4.2 Uni-Traveling Carrier Photodetectors

The uni-traveling carrier (UTC) photodiode structure is designed to increase power handling, thereby also decreasing the saturation inside the detector [10][101][102]. Its design is quite similar to the DDR design; it includes two light absorption regions, one a p-doped absorber and the second a non- or lightly-doped, depleted collection layer. This reduces the traveling time of electrons in the absorption layer, while holes respond more quickly [10]. Therefore, the photoresponse of UTC diodes is dominated by electron transport, in contrast to a standard p-i-n structure where both electrons and holes contribute to the response and low-velocity hole transport dominates the performance [10]. The University of Virginia UTC diodes examined in this work are a more recent iteration, called the modified uni-traveling carrier, or MUTC, structure.

The energy band diagram of an MUTC diode is shown in Figure 3.7. The main difference in the MUTC structure is an undoped InGaAs layer inserted between the InP drift layer and the p-doped absorption layer [103] [104] [105]. This multi-layered structure, shown in Figure 3.8, is bottom-illuminated and allows for much higher power handling, increases the responsivity, and reduced saturation effects when layer widths are optimized [105]. An example of this multi-layered structure is shown in Figure 3.8. Because of the anode and cathode positions, a negative bias

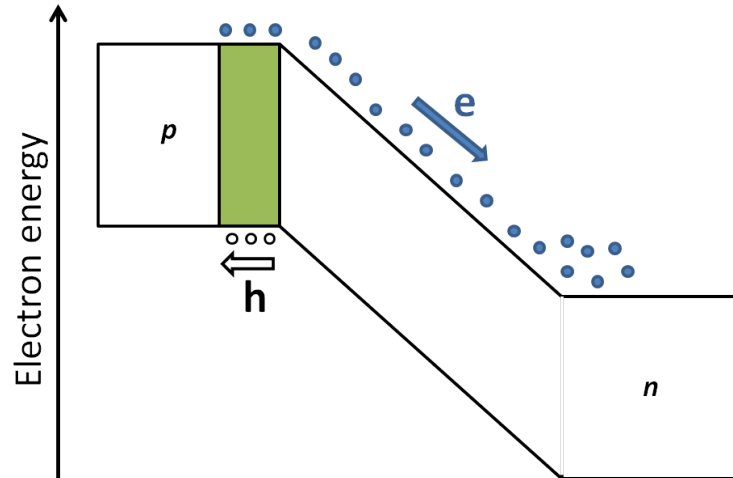


Figure 3.7: Energy band diagram of an MUTC photodiode.

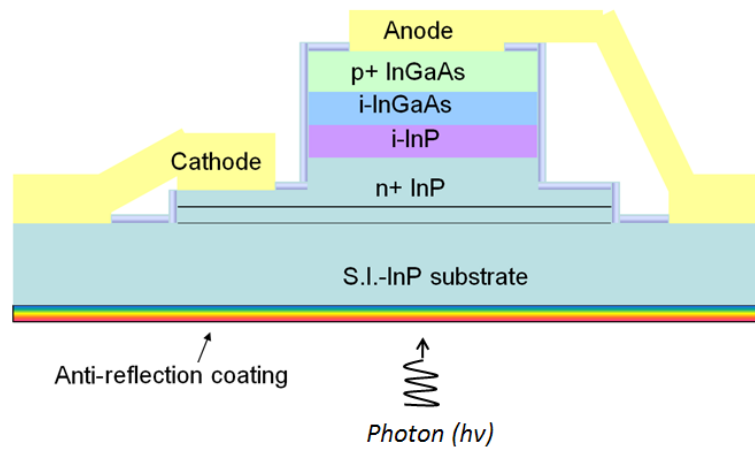


Figure 3.8: Example schematic for internal structure and electrical contacts for an MUTC photodiode..

voltage is applied to reverse bias these photodiodes; the method of electrically connecting to these diodes will be described in detail in Section 3.2.2.

### 3.2 Devices

The specific photodiodes used in this work are described and named in the following sections.

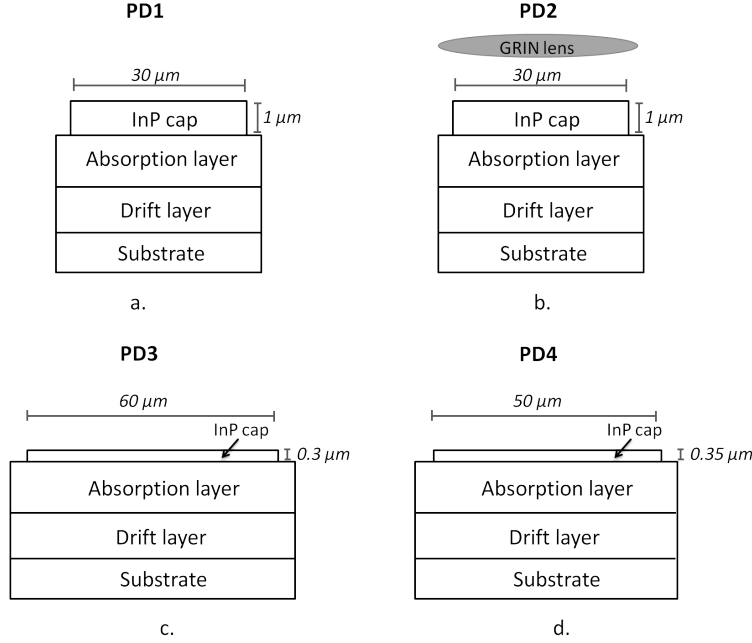


Figure 3.9: Differences in the physical structures of the four DSC photodiodes. a. PD1 with basic DDR structure, b. PD2 with GRIN lens for coupling, c. PD3 with larger active area and thinned InP cap layer, d. PD4 with intermediate sized active area and thinned InP cap layer.

### 3.2.1 DDR PIN Diodes

Four distinct photodiodes manufactured by Discovery Semiconductors, Inc. (DSC) are featured in this work, which we will refer to as PD1, PD2, PD3, and PD4. The basic structure of these four DDR diodes is almost identical. All are p-side illuminated InGaAs photodiodes with an InP cap layer, which helps reduce the dark current in the diode by reducing surface leakage current [106]. This cap layer is transparent at wavelengths greater than 1000 nm; however, there is considerable absorption in this layer at 900 nm where the Ti:Sapphire laser we employ operates. The photodiodes are packaged with coupling to a short ( $<1$  m) fiber pigtail having  $\sim 9$   $\mu\text{m}$  core. Additionally, they are internally terminated with a 50  $\Omega$  matching resistor, and the output microwave connection is via a coaxial (SMA) connector. They are externally reverse-biased up to 9 V by directly connecting a voltage source (either a voltage-controlled power supply or battery) to external pins on the package.

Table 3.1 lists the main characteristics of these diodes, and differences in their physical

Table 3.1: List of DSC diodes used in this work.

	Bandwidth	Responsivity @ 980 nm (PM Fiber)	Responsivity @ 1550 nm (SMF Fiber)	Notable Structure
PD1	22 GHz	0.3 A/W	0.8 A/W	SMF fiber
PD2	22 GHz	0.26 A/W	0.5 A/W	GRIN lens
PD3	12 GHz	0.34 A/W	0.6 A/W	Thinned InP cap layer
PD4	15 GHz	0.35 A/W	0.4 A/W	Thinned cap, medium size

structures are depicted in Figure 3.9. PD1 (SN300754) is the most basic device. It is an off-the-shelf, 22 GHz bandwidth, 30  $\mu\text{m}$  photodiode with an SMF-28 fiber pigtail (single mode at 1550 nm) and a 1  $\mu\text{m}$  thick InP cap layer. Responsivity is measured to be 0.3 A/W at 980 nm and 0.8 A/W at 1550 nm.

PD2, PD3, and PD4 exhibit modifications specifically engineered to improve certain aspects of the power handling and linearity. This series of modifications were facilitated by a Small Business Innovation Research (SBIR) grant between Discovery Semiconductors, Inc., and the Optical Frequency Measurements group at NIST specifically to develop photodiodes with increased performance for the generation of low phase noise signals. One common characteristic of these three devices is that two identical photodiodes with separate fiber coupling and microwave outputs are mounted inside of one single package. This matched pair of photodiodes with nominally identical response can be useful for applications relying on balanced photodetection to cancel common mode noise, which minimizes excess system phase noise in the system [107]. Figure 3.10a is a photograph of one of the dual-packaged photodiodes; Figure 3.10b is a schematic of the internal electrical connections and resistors. For the measurements described in this thesis, unless otherwise indicated, one of the two packaged diodes has been measured as a representative of the performance of both, as the performance of each was tested and found to be essentially identical to the other in the package.

The first new design was PD2. It features an integrated graded-index (GRIN) lens at the end of its SMF coupling fiber (see Figure 3.9). The GRIN lens shapes the optical beam to produce a more

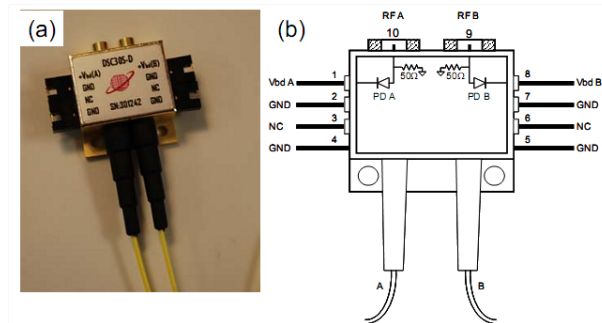


Figure 3.10: a. Photograph of a dual packaged DSC photodiode. b. Schematic of internal electrical connections and resistors.

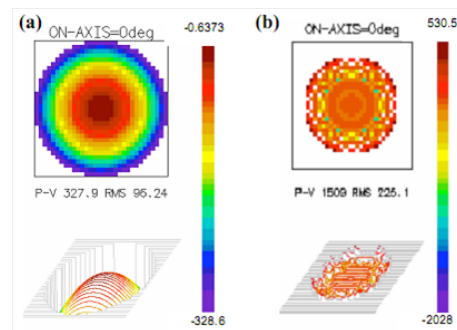


Figure 3.11: a. Gaussian distribution profile of the incident optical intensity for a typical SMF-coupled photodiode (red: higher intensity, blue: lower intensity). b. Flat top profile of the incident optical intensity due to GRIN lens coupling. From Ref. [108].

uniform illumination profile (flat-top rather than Gaussian) on the photodiode; this more effectively illuminates the whole photodiode and suppresses peak photocurrent density (see Figure 3.11) [100] [108]. In the spectral range of 900 nm, the responsivity is 0.26 A/W, and at 1550 nm it is 0.5 A/W. PD2 comes in two separate units—one with SMF-28 fiber pigtails for measurements at 1550 nm (SN301245) and another with polarization maintaining fiber (PMF) pigtails with a 6.6  $\mu\text{m}$  core that are single-mode at 980 nm (SN301244). PD2 with 980 nm PMF fiber was used with the Ti:Sapphire laser system, and PD2 with 1550 nm SMF-28 fiber was used with the Er:Fiber laser system. Both cases are simply referred to as “PD2” in context.

The second design, PD3, has regular coupling between the fiber and the semiconductor device (no lens). It is 60  $\mu\text{m}$  in diameter, 12 GHz bandwidth, and features a 0.3  $\mu\text{m}$  InP cap layer, compared to a 1  $\mu\text{m}$  thick layer in PD1 and PD2. Since 980 nm light, such as that from the Ti:Sapphire laser, is absorbed strongly in InP, a thinner InP cap layer reduces the absorption. The combination of larger diameter and thinned cap layer improves the responsivity (measured to be 0.34 A/W at 980 nm and 0.6 A/W at 1550 nm) and power handling of this photodiode. PD3 also comes in two separate units, one with standard single mode fiber pigtails for 1550 nm (SN900001) and another with PMF pigtails at 980 nm (SN900002); each unit is used at the appropriate wavelength and denoted simply as “PD3” in context.

The final design, PD4, is very similar to PD3. It has an InP cap layer of 0.35  $\mu\text{m}$ , but the device size is smaller, 50  $\mu\text{m}$  instead of 60  $\mu\text{m}$ , yielding a slightly higher bandwidth of around 15 GHz. Responsivity is 0.35 A/W and 0.4 A/W for 980 nm and 1550 nm, respectively. Two units with fiber pigtails for 980 nm (SN502337) and 1550 nm (SN502336) are likewise available for this design.

The basic setup for connecting the photodiodes to the laser source is shown in Figure 3.12.

### 3.2.2 Uni-traveling carrier diodes

A total of four UTC diodes from the University of Virginia (UVA) were used at different times during this research—HD-MUTC1, MUTC3, MUTC4, and HD-MUTC4. All are the modified

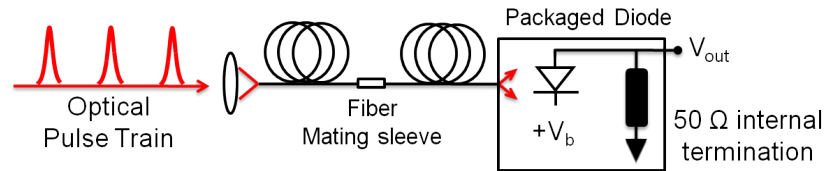


Figure 3.12: Schematic for the basic setup for connecting DSC diodes to a laser source.

uni-traveling carrier (MUTC) structure, yet feature distinct differences in design to produce different characteristics. These diodes were developed for telecom wavelengths and not specifically for 980 nm; however, the diodes were tested with both laser systems.

These diodes are designed by UVA and manufactured externally to specification. Many individual diodes of seven different sizes are fabricated on a single wafer in a repeating pattern. Figure 3.13a shows the basic repeating block of these seven different sizes—20  $\mu\text{m}$ , 28  $\mu\text{m}$ , 34  $\mu\text{m}$ , 40  $\mu\text{m}$ , 48  $\mu\text{m}$ , 56  $\mu\text{m}$ , and 68  $\mu\text{m}$ , referring to the diameter of the active area. A top view of an individual photodiode unit is shown in Figure 3.13b; the actual photodiode device is the small circle at the top, shown in Figure 3.13c. The rest of the structures around the actual diode are the electrical contacts on the top surface of the wafer; the bottom surface of the wafer, which is the incident surface for photons since these diodes are bottom-illuminated, is smooth and AR coated, as illustrated in Fig. 3.8. Since the diodes are not individually packaged and are used directly on the chip, the wafer is diced into smaller sections around 1  $\text{cm}^2$  in size, and contact is made with an individual device on the chip.

The schematic for connecting these diodes to a laser source and generating a microwave signal is shown in Figure 3.14. To access an individual device, a single wafer is mounted onto an ell-shaped aluminum mount, as seen in Figure 3.15. The mount is securely fastened to an optical table. The top of the mount is milled to a thinner width, and a small hole,  $\sim 5$  mm in diameter, is drilled through this thinner layer. A wafer is mounted with conductive thermal paste surrounding the small hole; the paste provides enough adhesion to hold the wafer as it rests upon the small lip created by the milling, yet still easily removed at a later time. In this configuration, a number of

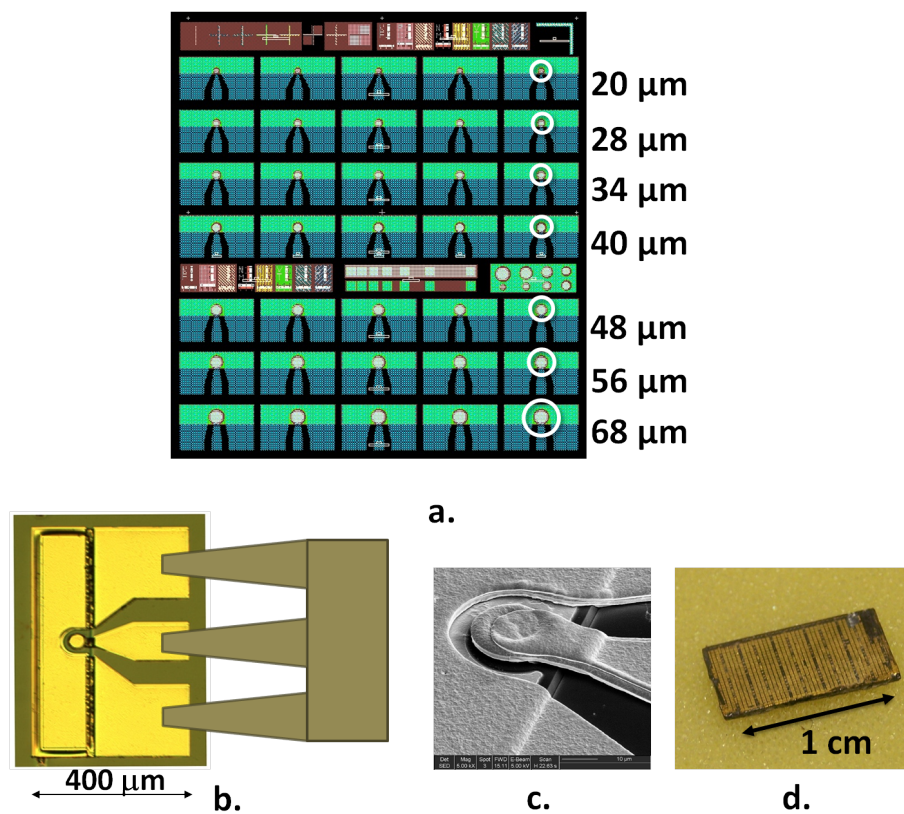


Figure 3.13: a. Layout of different sized MUTC devices on a wafer (active area circled), b. An individual device and depiction of microwave probe on electrical contacts, c. SEM scan of active area of device, d. Photo of actual wafer piece used in experiments.

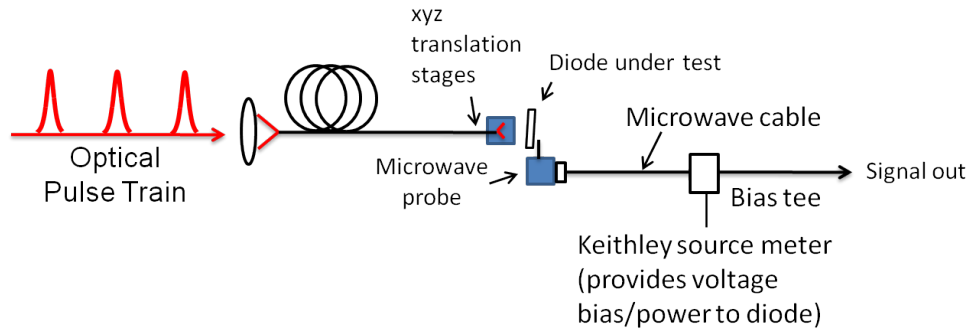


Figure 3.14: Schematic for the basic setup for connecting MUTC diodes to a laser source and a microwave probe.

devices on the wafer overlap with the through-hole, allowing an optical fiber tip to be brought close to the bottom surface of the wafer to illuminate a diode (Figure 3.15b). The metal contacts of the photodiode circuit are on the opposite surface of the wafer, and an air coplanar (ACP) microwave probe (Cascade Microtech ACP65-GSG-150) is used to make electrical contact with the diode. To align the microwave probe with a diode of the desired size, a CCD camera with a 4x lens is focused onto the top surface of the wafer, with the magnified view of the wafer projected on a computer monitor. With the microwave probe mounted onto a three-dimensional translation stage, the three probe tips can be aligned with the electrical contacts of the photodiode circuit, as illustrated in Fig. 3.13b. The microwave probe is connected to a bias tee (Picosecond Pulse Labs 5543) through a 40 GHz microwave cable. The DC port of the bias tee is connected to a Keithley 2400 current source meter where the bias voltage across the photodiode is set. The RF port of the bias tee provides the output microwave signal.

The incident optical signal is then aligned to the chosen photodiode. The fiber tip, mounted to a three-dimensional translation stage, is optimally aligned with the active area of the device by maximizing the photocurrent signal, which is shown on the Keithley Sourcemeter.

As mentioned, each wafer has seven diameters of the same MUTC structure: 20  $\mu\text{m}$ , 28  $\mu\text{m}$ , 34  $\mu\text{m}$ , 40  $\mu\text{m}$ , 48  $\mu\text{m}$ , 56  $\mu\text{m}$ , and 68  $\mu\text{m}$ . The smaller diodes are higher bandwidth but not as reliable for coupling light efficiently and are easily damaged at higher photocurrents. The active

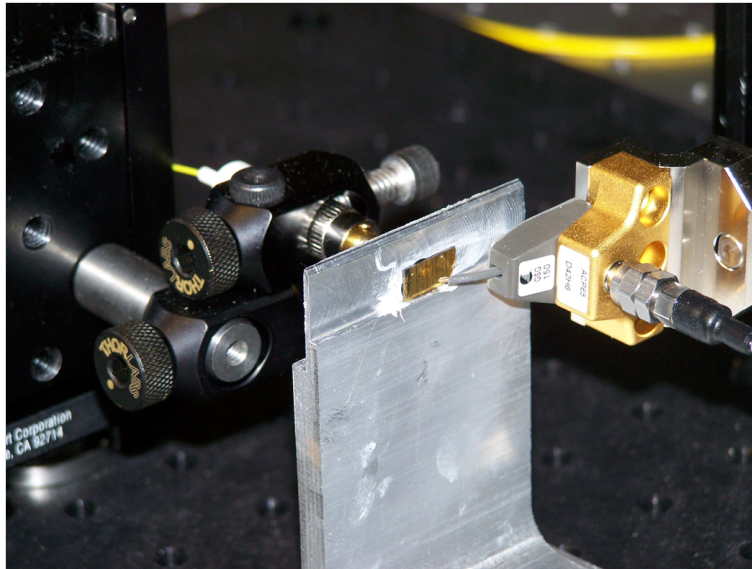
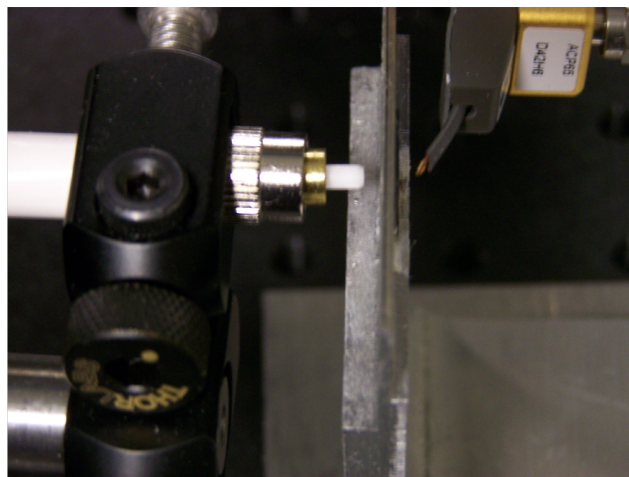
**a.****b.**

Figure 3.15: Photographs of the MUTC diode setup. a. A wafer mounted on the aluminum mount, with the microwave probe tip near the top side of the wafer. b. Side view of optical fiber pointed to the underside of the diode through a drilled hole in the mount and the microwave probe tip near the top side of the wafer.

areas of the larger diodes are generally larger than the beam width, allowing most of the incident light to be coupled onto the diode, but result in a slower device. The speed (bandwidth) of the PD can be determined from the RC constant. This approach works for PDs with bandwidth smaller than 30 GHz. The serial resistance is usually constant ( $\sim 2$  or  $3 \Omega$ ) and much smaller than the  $50 \Omega$  load resistor. The capacitance of the PD can be measured with a static C-V test and usually has a linear relationship with device size. Most of the analysis presented here was done on the mid-sized 34- and 40- $\mu\text{m}$  diodes, which provide the optimal balance of both bandwidth and ease of coupling. The bandwidth of these devices is around 15 GHz. The diode size will be noted in each measurement description.

Figure 3.16 shows the detailed internal structure of each of these diodes, and Table 3.2 lists the responsivities and notable structures of these four diodes. The two regular MUTC diodes, MUTC3 and MUTC4, are designed for high power and high speed. A thick absorber layer increases responsivity, and an added “cliff layer” boosts the internal semiconductor electric field to combat space charge effects, producing a larger saturation current. A thick InP drift layer and graded doping in the absorber both lead to higher speeds. However, this also requires a higher voltage bias to fully deplete, leading to larger heat generation. And the general light doping in the MUTC absorber leads to lower linearity. MUTC3 has responsivity 0.28 A/W at 980 nm and was not measured at 1550 nm. A later version of this diode was also AR coated at 980 nm. MUTC4 is a newer design; it is AR coated at 1550 nm. Responsivity was measured to be 0.23 A/W at 980 nm and 0.28 A/W at 1550 nm.

The “HD” diodes are highly doped in the InGaAs absorber to directly increase linearity by reducing the capacitance and responsivity’s dependence on voltage. However, this leads to overall low responsivity and lower speeds at high photocurrent. HD-MUTC1 has responsivity of 0.22 A/W at 980 nm and 0.4 A/W at 1550 nm. A later version of HD-MUTC1 was AR coated at 980 nm for measurements specifically with the Ti:S laser. HD-MUTC4 is a newer design; it is AR coated at 1550 nm, and responsivity was measured to be 0.23 A/W at 980 nm and 0.28 A/W at 1550 nm.

Table 3.2: List of MUTC diodes used in this work.

PD	Responsivity @ 980 nm	Responsivity @ 1550 nm	Notable Structure
MUTC3	0.28 A/W	not measured	High power and high speed
MUTC4	0.34 A/W	0.6 A/W	High power and high speed
HD-MUTC1	0.22 A/W	0.4 A/W	High linearity
HD-MUTC4	0.23 A/W	0.28 A/W	High linearity

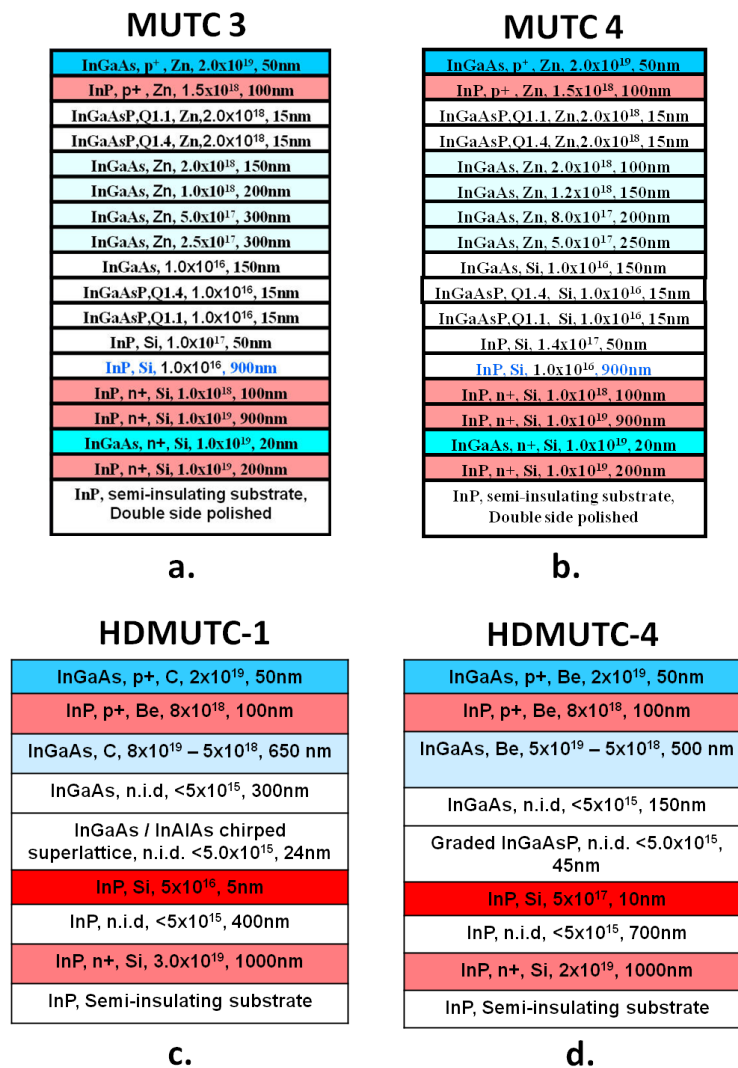


Figure 3.16: Internal structures of a. MUTC3, b. MUTC4, c. HD-MUTC1, and d. HD-MUTC4.

## Chapter 4

### Noise Characterization and Photodetection

Before we discuss low phase noise signals and the noise properties of photodetectors in depth, it is important to understand what is meant by time and frequency stability and phase noise. The first section of this chapter describes the conventional methods of quantifying phase noise and timing stability, and Section 4.2 describes the physical models of the photodetector noise effects introduced in Chapter 3.

#### 4.1 Introduction to Noise–Frequency Stability in the Time and Frequency Domains

Frequency stability can be considered the degree to which an oscillating signal reproduces an ideal signal over many cycles [109]. Given a frequency source with a sine wave output signal, the ideal voltage output is

$$V(t) = V_0 \sin(2\pi\nu_0 t), \quad (4.1)$$

where  $V_0$  is the nominal peak amplitude voltage of the signal,  $\nu_0$  is the nominal frequency of the signal, and  $2\pi\nu_0 t$  is the phase. In reality, there will be natural fluctuations in both the amplitude and the phase of the signal:

$$V(t) = [V_0 + \epsilon(t)] \sin[2\pi\nu_0 t + \phi(t)], \quad (4.2)$$

where  $\epsilon(t)$  is amplitude deviation and  $\phi(t)$  is phase deviation. While fluctuations in amplitude do occur, we are particularly concerned with fluctuations of phase for this application; therefore,

the following analysis will focus on the developing the characterization of phase fluctuations and stability given by  $\phi(t)$ .

A frequency measurement must involve two oscillators. It is impossible to purely measure only one oscillator; an oscillator is considered to be stable relative to another one, ideally if possible one that closely represents the ideal signal (Eq. 4.1) [109]. This is called the reference oscillator.

Most frequency counters are sensing the zero-crossing of a signal where it is most sensitive to phase fluctuations [109]; therefore, it is convenient to define instantaneous frequency as the derivative of the total phase [110]:

$$\nu(t) = \nu_0 + \frac{1}{2\pi} \frac{d\phi}{dt}. \quad (4.3)$$

The phase can be defined in terms of a time-dependent function of  $x$ :

$$x(t) = \frac{\phi(t)}{2\pi\nu_0} \quad (4.4)$$

The time derivative of  $x(t)$  is called fractional frequency,  $y(t)$ . It is a dimensionless quantity defined as the fractional frequency difference of an oscillator with signal  $\nu(t)$  with respect to a reference oscillator having the same nominal frequency,  $\nu_0$ , of the oscillator [110]:

$$y(t) = \frac{\Delta f}{f} = \frac{\nu(t) - \nu_0}{\nu_0} = \frac{1}{2\pi\nu_0} \frac{d\phi}{dt} = \frac{dx}{dt}. \quad (4.5)$$

Since no measurement system has infinite bandwidth, it is actually impossible to measure instantaneous frequency directly [109]. In practice,  $y(t)$  is measured once at a time  $t$  and then again at  $t + \tau$ , where  $\tau$  is the time between measurements, or the averaging time. The averaging time can be any duration, picoseconds or days, whatever is appropriate for the measurement. This yields an average fractional frequency between the two measurements:

$$\bar{y}(t) = \frac{x(t + \tau) - x(t)}{\tau}. \quad (4.6)$$

A set of  $N$   $y(t)$  points taken over a given time  $T$  is used for both time and frequency stability analysis.

There are several ways of obtaining a set of fractional frequency data [109][111]. The time difference method, two frequency signals compared in a time-interval counter, is commonly used and

straightforward but lacks great precision. Other methods, such as the beat-frequency method and the phase bridge methods offer greater precision in determining phase fluctuations. Our methods of generating fractional frequency fluctuations will be described in the context of each measurement.

#### 4.1.1 Time Domain Representations of Frequency Stability—The Allan Variance

Given a set of  $y(t)$  data, time stability analysis can be done using one of many statistical variances developed specifically for precision oscillators. The standard statistical variance could be used; however, it is divergent for some types of oscillator noise [110]. Hence, another method was developed to account for this phenomenon. This statistic, the Allan Variance (Avar), is now the scientific standard for this application, though others have been developed based on similar principles addressing different issues related to clock stability [110].

The Allan Variance is given by

$$\sigma_y^2(\tau) = \left\langle \frac{1}{2}(\bar{y}(t + \tau) - \bar{y}(t))^2 \right\rangle \quad (4.7)$$

where the brackets “ $\langle \rangle$ ” denote a time average [111]. Avar gives the level of fractional frequency stability as a function of averaging time. It is often cited as a level of instability at a particular time, often at one second, meaning the instability between two observations one second apart.

Other variances based on the Allan Variance method have been developed to improve upon some aspects of the Avar, such as better statistical confidence and handling of longer data sets [110][112]. Avar also cannot differentiate between certain noise types (discussed in Section 4.1.3), and some other variances have been created to solve that issue. However, the Allan Variance remains a robust and reliable tool for analysis of timing stability.

While time domain statistics are beneficial for describing longer-term phase fluctuations, shorter term stability is of even greater interest in the generation of 10 GHz signals. This regime is best described by the frequency domain representation of stability.

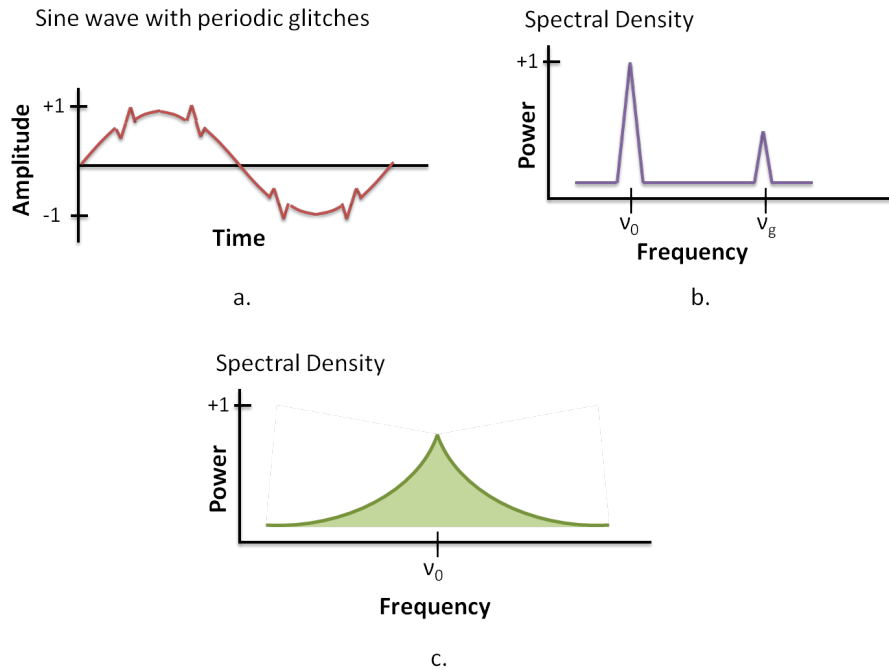


Figure 4.1: a. A sine wave of frequency  $\nu_0$  with periodic glitches at  $\nu_g$ , b. Plot of spectral density for the sine wave in (a), c. Spectral density with noise pedestal for a typical noisy signal.

#### 4.1.2 Frequency Domain Representations of Frequency Stability— $\mathcal{L}(f)$

Signal stability can also be characterized in the frequency domain using spectral analysis of the frequency fluctuations. Consider a perfect sine wave  $V(t)$  of frequency  $\nu_0$  perturbed by some sort of glitch evenly spaced in time (see Figure 4.1a). There is a frequency associated with the signal itself,  $\nu_0$ , and a frequency associated with the periodic glitches,  $\nu_g$ . If we plot rms power of the signal versus frequency, called the power spectrum, we see a large amount of the signal power at the main frequency  $\nu_0$  and a smaller yet significant portion at  $\nu_g$  (Figure 4.1b).

In reality, even more complex perturbations to the signal exist than demonstrated above. Additionally, some noise causes the instantaneous frequency to jitter around the carrier frequency [111]. This leads to a noise pedestal around  $\nu_0$ , as depicted in Figure 4.1c.

To see the amount of signal power going into every “glitch” frequency causing instability of the original signal, Fourier expansion is used to break the signal down into all its spectral components; conversely, the superposition of all the Fourier frequency components reproduces the

original signal. The difference between the carrier frequency and the frequency component is called the Fourier frequency. If the power spectrum is normalized so that the total area under the curve is equal to one, this plot is called the power spectral density.

The power spectrum of the whole signal  $V(t)$  is called the RF spectrum, often in units of watts/Hertz; this is the output given by an RF spectrum analyzer. This spectrum includes both fluctuations of amplitude,  $\epsilon(t)$ , and phase,  $\phi(t)$ , but it is not generally possible to distinguish between the two on the output of the RF spectrum analyzer. The RF spectrum also includes the carrier frequency. The total RF spectra can be separated into the two separate components—spectral density of  $\epsilon(t)$ , called the AM power spectral density, and spectral density of phase fluctuations  $\phi(t)$  [109].

Since we are primarily interested in the phase fluctuations, we define  $S_\phi(f)$  to be the spectral density of phase fluctuations at a Fourier frequency  $f$ , given by Fourier analysis of the fractional frequency fluctuations  $y(t)$  of our signal [109]. This is to be distinguished from the power spectrum; it is in units of radians<sup>2</sup>/Hertz and contains information about noise that is offset in frequency from the fundamental carrier frequency.

Similar to phase fluctuations between two oscillators,  $S_\phi(f)$  can be measured using a reference oscillator in a phase bridge measurement system [111]. Two oscillators are compared by setting the two signals in phase quadrature (that is, 90 degrees out of phase) and mixing the two outputs. The two oscillators are held in phase lock, assuring long-term matching of the two frequencies, or the output of one oscillator is split resulting in identical signals in both arms (shown in Figure 4.2). The resulting output phase fluctuations between the oscillators appears as voltage fluctuations from the mixer. This gives  $V_{RMS}(f)$ , the root-mean-squared noise voltage in a 1 Hz bandwidth at Fourier frequency  $f$ . The sensitivity of the mixer,  $k_d$  (units of volts per radian), is the conversion factor that tells how much phase fluctuation is translated into the output voltage fluctuations in the mixer. This quantity can be measured by determining the slope of the sinusoidal mixer output passing through zero volts (shown in Figure 4.2).

The phase bridges used in this work will be described for each measurement. It is important

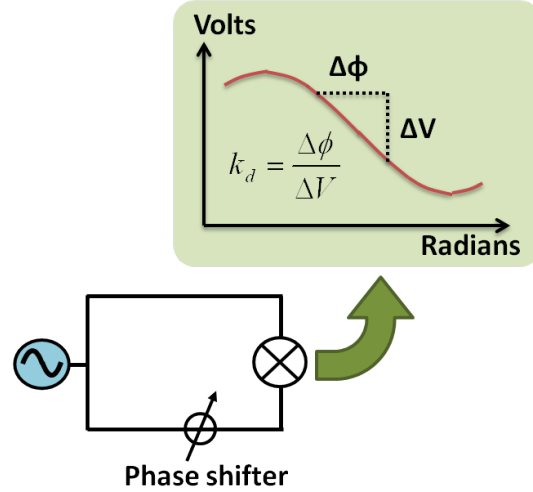


Figure 4.2: Phase bridge with one split oscillator signal. Gain,  $k_d$ , can be determined from slope of mixer output.

to note that the output is noise power associated with two oscillators; for a comparison between two similar yet uncorrelated oscillators, the noise of one oscillator can generally be assumed to be half of the result.

For small deviations in phase ( $\delta\phi \leq 1$  radian), we then have spectral density of phase given by

$$S_\phi(f) = \left[ \frac{V_{RMS}(f)}{k_d} \right]^2. \quad (4.8)$$

This is in units of radians<sup>2</sup>/Hz. Spectral density of phase can be related to the spectral density of fractional frequency fluctuations,  $S_y(f)$ , as [109]

$$S_y(f) = \left( \frac{f}{\nu_0} \right)^2 S_\phi(f). \quad (4.9)$$

$S_\phi(f)$  and  $S_y(f)$  are both single-sideband, double-sided spectra. This means they include information for Fourier frequencies above and below the carrier (positive and negative frequencies) but have folded the negative frequencies over onto the positive frequencies. Since the spectrum is nominally symmetric about the carrier, this amounts to doubling the noise power from Fourier frequencies  $0 < f < \infty$ .

Single-sided, single sideband noise is given by the quantity  $\mathcal{L}(f)$ ; it is simply defined as half

of  $S_\phi(f)$ .

$$\mathcal{L}(f) = \frac{1}{2}S_\phi(f). \quad (4.10)$$

When the noise power is small,  $\mathcal{L}(f)$  can also be thought of as a “noise to signal” ratio, as it compares the level of the noise to the level of the carrier. It is also typically converted from linear into logarithmic scale:

$$\mathcal{L}(f) = 10 \log \left[ \frac{1}{2}S_\phi(f) \right] = 10 \log \left[ \frac{P_{noise}}{P_{signal}} \right]. \quad (4.11)$$

### 4.1.3 Power Law Scale and Noise Types

Within an oscillator, there may be non-random and random fluctuations in the fractional frequency. Non-random fluctuations are deterministic effects that can in many cases be predicted and even removed. This could include naturally occurring frequency drift of the oscillator or external effects like temperature-induced change in frequency. Random fluctuations, on the other hand, are not systematic; however, most of these fluctuations naturally fall into separate and distinct categories of noise processes that can actually be distinguished and modeled in frequency with spectral density and in time with the Allan Variance. The five most common noise types are random walk in frequency (RWFM), flicker in frequency (FLFM), white noise in frequency (WHFM), flicker in phase (FLPM), and white noise in phase (WHPM).

In terms of spectral density of frequency fluctuations,  $S_y(f)$ , these noise types can be modeled by the power-law equation

$$S_y(f) = h_\alpha f^\alpha, \quad (4.12)$$

where  $\alpha$  is an integer designating the particular noise type and  $h_\alpha$  describes the corresponding noise level. In general, since multiple noises can be present at a given time, a plot of  $S_y(f)$  represents a linear combination of all the power-law processes in the signal. It is possible to have all five noise types present from a single oscillator; however, it is much more common to have only two or three that are dominant [109]. These noise processes follow a power-law structure; that is, on a log-log plot, each one lies along a line of a different slope, given by  $\alpha$ . For the five noise types,  $\alpha = -2, -1,$

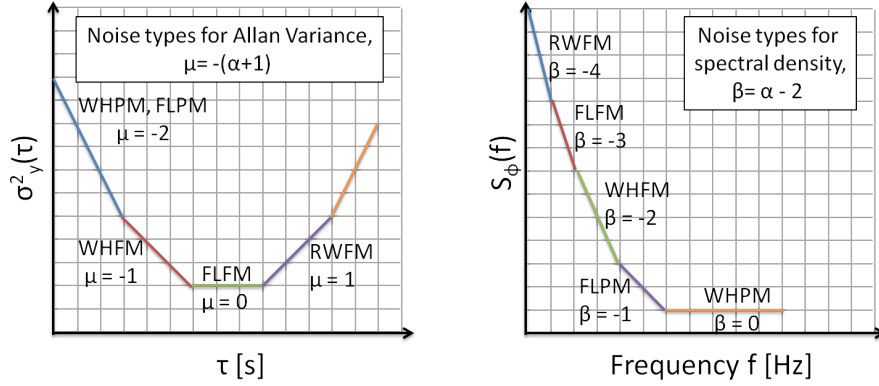


Figure 4.3: Power law noise types for a. Allan Variance in the time domain, and b. spectral density in the frequency domain.

0, 1, and 2 for RWFM, FLFM, WFM, FLPM, and WHPM, respectively. The power law exponent for  $S_\phi(f)$  is  $\beta$ , where  $\beta = \alpha - 2$ . In the Allan Variance representation, these same noise types are manifest as  $\sigma_y^2 = \tau^\mu$ , where  $\mu = -(\alpha + 1)$  [110]. Plots of these noise types for the Allan Variance and  $S_\phi(f)$  are shown in Figure 4.3.

As shown in Figure 4.3a, WHPM and FLPM are indistinguishable using the Allan Variance. As mentioned in Section 4.1.1, other variances have been developed that can make this distinction, but this disambiguation is not necessary to the work presented here.

It is possible to translate from the frequency domain and spectral analysis to the time domain and the Allan variance using the random noise model of Figure 4.3. However, in this work, any presentations of time or frequency domain have been measured separately, and such a conversion is not necessary here.

## 4.2 Noise in Photodetectors

In Chapter 2, the main noise characteristics of photodetectors were introduced. In the following sections, we focus our discussion on the details of noise processes associated with the detection of a repetitive train of short (e.g. picosecond or shorter) optical pulses, such as those emitted from a mode-locked laser.

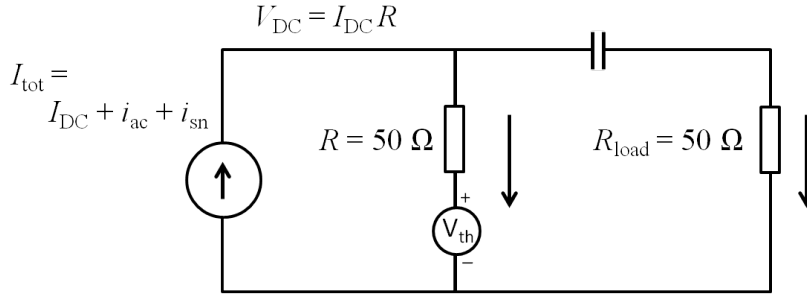


Figure 4.4: Schematic of current source, thermal source, and resistors in a typical photodetection circuit.  $I_{DC}$  is the average DC photocurrent,  $I_{ac}$  is the signal current,  $i_{sn}$  is the shot noise current,  $V_{th}$  is the thermal noise voltage source intrinsic to the  $50\ \Omega$  resistor.

#### 4.2.1 Thermal Noise

Thermal noise (often referred to as Johnson or resistive noise) is associated with random fluctuations of the current across resistive elements of the photodetection circuit [85][86]. Thermal noise is a white phase noise process (WHPM of Fig. 4.3), meaning it is flat across the frequency spectrum and not frequency dependent. The relevant resistance in the photodiode system includes the load resistor of the photodiode and an external circuit or component, both typically  $50\ \Omega$ . The thermal noise can be determined by analyzing a simple schematic of a photodetection circuit, shown in Figure 4.4 using Kirchhoffs law.

The internal resistor acts as a thermal noise voltage source,  $V_{th}$ . Voltage fluctuations in a one Hertz bandwidth, similar to noise voltage out of a mixer in the above described phase bridge, are given by the single-sided, double-sideband power spectral density  $V_{th}^2$ :

$$V_{th}^2 = 4k_B T R, \quad (4.13)$$

where  $k_B$  is Boltzmann's constant ( $1.38 \times 10^{-23}$  J/K),  $T$  is the temperature (room temperature, 300 K), and  $R$  is the resistance. Because the photocurrent flows across the two  $50\ \Omega$  resistors, only half the total voltage drops across the photodetector resistor, resulting in a factor of four reduction in the spectral density and also the noise power (proportional to the square of the voltage). Since thermal noise is independent of the signal, the noise power contains both amplitude and phase fluctuation in equal amounts. To consider only the result of phase fluctuations, the noise power is

halved yet again, yielding

$$P_{th} = \frac{1}{2}k_B T. \quad (4.14)$$

For a total signal power  $P_0$ , the final single-sided thermal noise is given by  $\mathcal{L}(f)$  as a noise-to-signal ratio:

$$\mathcal{L}_{th}(f) = \frac{k_B T}{2P_0}, \quad (4.15)$$

or, in log scale in units of dBc/Hz,

$$\mathcal{L}_{th}(f) = 10 \log \frac{k_B T}{2P_0} \times 1000 = -177 - 10 \log P_0. \quad (4.16)$$

where  $P_0$  is in units of milliwatts. For a 10-GHz signal, as measured on a microwave spectrum analyzer, with  $P_0 = -20$  dBm, the single-sided thermal noise is -157 dBc/Hz. For a stronger 10 dBm signal, thermal noise would be -187 dBc/Hz.

#### 4.2.2 Shot Noise

Shot noise is related to the randomness of the incident photon stream [87][88]. Like thermal noise, it is a white phase noise process and not frequency dependent. Due to the discrete nature of photons, it is a fundamental limit for an optical process. The random fluctuations in photon arrival times creates a shot noise photocurrent:

$$i_{shot} = \sqrt{2eI_{DC}BW}, \quad (4.17)$$

where  $e$  is the fundamental electron charge ( $1.6 \times 10^{-19}$  C),  $I_{DC}$  is the average signal photocurrent, and BW is the bandwidth. This produces a single-sided, double-sideband power spectral density of current variance, defined within a 1-Hz bandwidth, of

$$\overline{i_{shot}^2} = 2eI_{DC}. \quad (4.18)$$

Shot noise power is given by

$$P_{shot} = \overline{i_{shot}^2} R. \quad (4.19)$$

As with thermal noise, with the given resistance the shot noise power is decreased by a factor of four. Also similarly, the noise power due to shot noise contains fluctuations to amplitude and phase equally, so fluctuations in phase will be half the total noise power.

$$P_{shot} = \frac{eI_{DC}R}{4}. \quad (4.20)$$

Finally, the single-sideband phase noise due to shot noise is given by

$$\mathcal{L}_{shot}(f) = 10 \log \left[ \frac{P_{shot}}{P_0} \right] = 10 \log \left[ \frac{eI_{DC}R}{4P_0} \right], \quad (4.21)$$

where  $P_0$  is the signal power in milliwatts, and  $P_0 = 2I_{DC}R$ . Finally, combining Eq. 4.16 and Eq. 4.21 yields the following expression for the phase noise arising from both the thermal and shot noise processes:

$$\mathcal{L}_{shot}(f) = 10 \log \left[ \frac{2k_B T + eI_{DC}R}{4P_0} \right]. \quad (4.22)$$

It is important to note that the signal power increases as photocurrent squared while the noise power increases linearly with photocurrent. Thus, as the average photocurrent increases,  $\mathcal{L}_{shot}$  will decrease. Therefore, it is advantageous to operate at a higher photocurrent to decrease the shot noise limited noise floor. In Figure 4.5, thermal noise power at room temperature and shot noise power are plotted as a function of photocurrent. Thermal noise dominates for photocurrent less than 0.5 mA, so operating at higher photocurrents sets the white noise floor of the signal at the shot noise limit. With this in mind, we limit further analysis of overall photodiode performance to shot noise and amplitude-to-phase conversion (discussed in detail in the following section).

In theory, as long as microwave power continues to increase from the photodetector, the shot noise limited  $\mathcal{L}(f)$  would continue decrease. However, after a certain amount of optical power is incident on the diode, the diode can no longer produce a corresponding amount of microwave power. This effect is called saturation. Once the photodiode is saturated, it is not possible to further reduce the shot noise or thermal noise floor of the generated microwave signal by increasing the optical power [43]. With saturation of the microwave power, the detector bandwidth also decreases, so that the shot noise power in the region of 10 GHz also decreases; thus, the signal-to-noise ratio is fixed at a constant value.

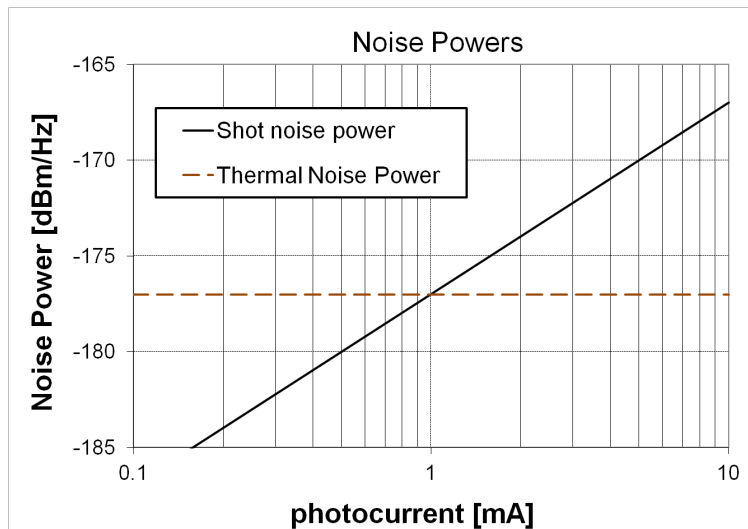


Figure 4.5: Plot of thermal and shot noise powers, from Eq. 4.15 and Eq. 4.20.

According to the semiconductor model, saturation is predominately caused by the space-charge screening effect. The basic photodetection process means that photons are converted into electrons inside the absorption region of the diode. Due to their charge, a large number of electrons inside the photodiode generate an area of charge density that in turn produces its own electric field. At low incident optical power, the electric field created by the bias voltage in the absorption region is larger than the electric field produced by the space charge. However, as optical power is increased, more photons are coming into the photodiode, producing more electrons and adding to the space charge. The resulting space charge electric field becomes large enough that it begins to interfere with the bias field in the region. Thus, the influence of the bias field decreases, reducing the velocity of electrons moving in the material. The rate of increase of the output power diminishes, an effect called compression. If incident signal power continues to increase when microwave power goes into compression, then the overall shot noise will increase as well.

A high linearity or high power handling photodetector can handle higher levels of incident peak power before signal compression, making it good choice for reducing the shot noise limit. Figure 4.6 shows the 10 GHz signal power verses photocurrent for the four DSC diodes used in this thesis. Note that the 10 GHz power shows the expected “linear” dependence at lower photocurrents

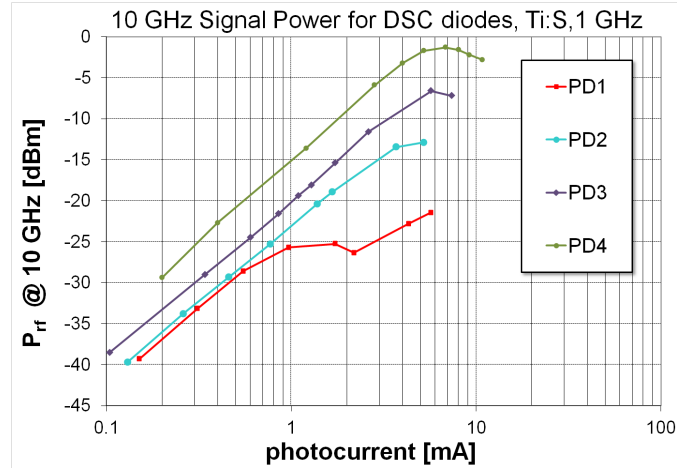


Figure 4.6: Plots of 10 GHz signal power vs. photocurrent for the four DSC photodiodes.

where it increases proportional to the square of the photocurrent. Then at photocurrents between  $\sim 2$  and 5 mA (depending on the specific photodiode), there is a roll-off as photocurrent increases. This is the signal compression due to saturation. It is clear that the design modifications made to later devices (GRIN lens, PD2; larger device, PD3; thinned cap layer, PD4) achieve significant improvement in signal size and compression.

Repetition rate also plays a key role in saturation. Given the same average optical power, a lower repetition rate pulse has a higher energy per pulse than a higher repetition rate pulse, resulting in more rapid saturation of the microwave signal from the photodiode detecting the repetition rate (Figure 4.7) [113]. For the same average output power, a higher repetition rate mode-locked laser such as Ti:Sapphire with  $f_{rep} \sim 1$  GHz has an advantage over a mode-locked laser with a repetition rate of hundreds of megahertz (such as the Er:Fiber laser described in Section 2.1.2 with  $f_{rep} \sim 250$  MHz) in terms of saturation. This drawback for lower-repetition rate lasers can be overcome by multiplication of the pulse repetition rate, which will be described in detail in Section 5.2.1.

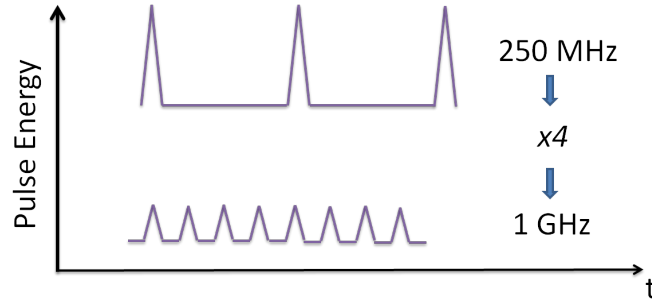


Figure 4.7: Pulse energy for a 250 MHz pulse train compared to a frequency multiplied pulse train at 1 GHz, assuming the same average power.

### 4.2.3 Amplitude to Phase Conversion

Besides the fundamental shot noise of the photocurrent, the conversion of laser amplitude noise into electronic phase noise during photodetection has been previously identified as a prominent and limiting noise source [43] [44] [45] [46] [47] [114] [27]. We have seen that due to the space charge screening effect, when the incident optical power is increased, a broadening of a PDs electrical pulse is observed due to a delay in the transmission of photocarriers generated by the incident pulse train across the photodiode [43][115][44][46]. This indicates that fluctuations in signal power (amplitude) have an influence on the overall phase of the PD's output signal. This amplitude-to-phase (AM-to-PM) conversion greatly impacts the conversion of an otherwise stable optical pulse train to a microwave signal, especially since the femtosecond lasers can have significant fluctuations in power.

We define an AM-to-PM coefficient,  $\alpha$ , to characterize this conversion. It is defined as the induced RMS phase variation on the measured repetition rate or a harmonic thereof ( $\Delta\phi$ , in radians) arising from a fractional power fluctuation ( $\Delta P/P_0$ ). Since the energy,  $E_0$ , of the pulse is proportional to power, the AM-to-PM coefficient is sometimes identically defined in terms of  $\Delta E/E_0$  [116].

$$\alpha \equiv \frac{\Delta\phi}{\Delta P/P_0} = \frac{\Delta\phi}{\Delta E/E_0}. \quad (4.23)$$

Time delay, or changes in phase of a signal, due to changes in the incident optical power are observed in the time-domain impulse response of the photodiode (Section 5.1). A simple model

of AM-to-PM conversion has been built in Ref. [116] based on the roughly asymmetric triangular shape of the impulse response [45]. The current is modeled as

$$i(t) = \begin{cases} i_{max} \cdot \left(1 - \frac{t}{\tau}\right) & \text{for } 0 < t < \tau \\ 0 & \text{otherwise} \end{cases} \quad (4.24)$$

with  $i_{max}$  modeled with double exponential growth with  $E$ :

$$i_{max} = i_0 \cdot \left(1 - A_1 \cdot e^{E/E_1} - A_2 \cdot e^{-E/E_2}\right), \quad (4.25)$$

where  $A_1 + A_2 = 1$ , and  $A_1$ ,  $A_2$ ,  $E_1$ , and  $E_2$  can be found experimentally by a double-exponential fit of the peak photocurrent. The dependence of  $\tau$  with  $E$  can be determined with energy conservation (see [116]).

Fourier analysis of  $i_{max}$  relates the tangent of the phase  $\phi(t)$  to the current,  $i(t)$  as

$$\tan[\phi(t)] = \int_{-\infty}^{\infty} i(t) \sin(\omega t) dt / \int_{-\infty}^{\infty} i(t) \cos(\omega t) dt, \quad (4.26)$$

which leads to

$$\phi(\omega) = \arctan \left[ \frac{\omega\tau - \sin(\omega\tau)}{1 - \cos(\omega\tau)} \right]. \quad (4.27)$$

Differentiating  $\phi(t)$ , the AM-to-PM conversion factor  $\alpha$  can then be expressed as

$$\alpha = \frac{\omega\tau \sin(\omega\tau) + 2 \cos(\omega\tau) - 2}{2\omega\tau \sin(\omega\tau) + 2 \cos(\omega\tau) - \omega^2\tau^2 - 2} \times \frac{\omega d\tau}{dE/E}. \quad (4.28)$$

The conversion factor's dependence on the angular frequency  $\omega$  is interesting in that, for pulse energies such that  $\omega\tau/2$  is a solution of  $\tan(x) = x$ ,  $\alpha$  goes to zero. These “nulls” predicted in this model are actually consistently observed in measurements of  $\alpha$  (see Section 5.3). These nulls occur above the saturation photocurrent of the photodiode, where the time response (shown for the photodiodes used in this work in Section 5.1) exhibits the strong asymmetrical triangular shape assumed by the model. The nulls are also observed to increase in number with a decrease in repetition rate, which will also be discussed in Section 5.3.

Section 5.3 describes various AM-to-PM conversion measurement methods, and this effect, including the magnitude of  $\alpha$  and null points, is carefully measured and characterized for the photodiodes. The ultimate effects of amplitude fluctuations on phase noise will be shown in Chapter 6.

## Chapter 5

### Characterization of Photodetector Noise

In this chapter, the basic performances of a variety of photodetectors used for optical-to-microwave conversion are described in detail. The effects of both saturation and amplitude to phase conversion are measured and quantified using both time and frequency domain techniques. Since saturation and the reduction of total signal size are generally undesirable effects, filtering techniques are introduced to reduce the pulse peak power and alleviate saturation. AM-to-PM conversion is of concern, particularly using laser sources with high amplitude noise, so ways of minimizing this effect are explored. Photodiodes with favorable noise properties can be used in the microwave generation scheme to reduce overall noise in the optical-to-microwave conversion process.

#### 5.1 Impulse Response

When a photodiode is illuminated by an optical pulse with duration significantly less than the photodiode response time, its output is the time-domain electrical impulse response. The shape of the pulsed output—primarily characterized by the peak output power, center of mass, and the pulse width—gives information about how the pulsed signal is handled inside the photodiode. The total energy of the photons absorbed from the incident optical pulse that impinge upon the photodiode is conserved in the photoconversion process; however, non-linearities in the photodiode lead to saturation, temporal broadening and a time delay of the electrical pulse generated in the absorption layer. A broadening of the pulse or shift in the center of mass as the incident power is increased is a

clear indication of the saturation effect. Likewise, an increase in output voltage or decrease in pulse width for an increasing incident power is an indication of the efficacy of modifications in internal structure of the photodiode. Changes in bias voltage also influence the pulse shape; increasing the bias and the resulting static field inside the semiconductor compensates for the increase in space-charge screening up to the point that too much voltage can result in electrical breakdown, which destroys the diode. Even qualitative comparison of the impulse response between these different situations allows us to pick the ideal photodiode and operating parameters for the given operating conditions. This is confirmed by more rigorous analysis involving the Fourier transformation of the impulse response. This approach provides specific information about the electrical phase at a chosen frequency (and its dependence on optical power), which leads to important quantification of the coupling between amplitude fluctuations and phase noise.

Impulse responses are measured with a 20-GHz sampling oscilloscope, an Agilent Infiniium DCA-J 86100C. The laser's repetition rate is phase-locked to a synthesized signal at  $f_{rep}$ , and that signal is used to trigger the oscilloscope. The DSC photodiodes are connected to the laser source as in Figure 3.12 with the voltage output going directly to the oscilloscope with the SMA connector to eliminate loss in microwave cables. If the peak voltage of the signal exceeds the limit of the oscilloscope, a microwave attenuator between 3 and 10 dB is used between the photodiode and oscilloscope, and the magnitude of the impulse response is corrected to account for this loss. A neutral density filter wheel is placed in the Ti:S beam path before the coupling to optical fiber to attenuate the optical power on the photodiode. The incoming optical pulse duration for the Ti:S laser is approximately 1 ps. For the DSC photodiodes, it is worth noting that the photocurrent is divided between two  $50\ \Omega$  resistors—one inside the diode and one inside the oscilloscope. If the diodes were not internally terminated and all the photocurrent went across the  $50\ \Omega$  of the oscilloscope, the voltage would be twice as large.

Figure 5.1 shows impulse responses at increasing optical powers for PD1, PD2, and PD3 as measured on the Ti:S laser with 1 GHz repetition rate. The plots illustrate the changes in peak voltage and pulse width between the three photodiodes having different diode sizes/bandwidths

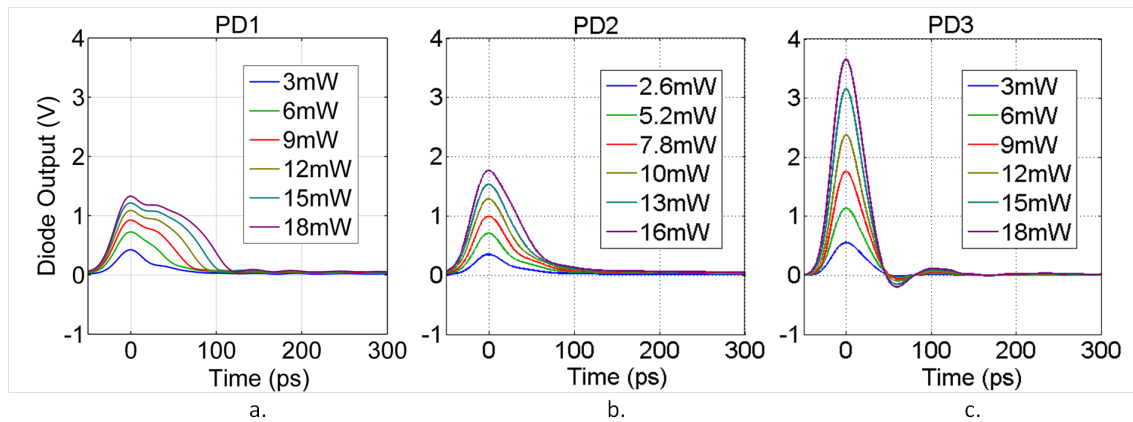


Figure 5.1: a-c. Impulse responses for the three photodiodes in increasing optical power steps (note optical power can be converted to photocurrent by multiplying by responsivity given in Table 3.1). The output voltage is measured across the  $50\ \Omega$  input impedance of the sampling scope.

as well as external modifications. The plots of PD1 were measured at a bias voltage of 7 V and PD1 and PD2 at a bias voltage of 9 V. As incident power increases, the pulse's center of mass shifts and the pulse width increases, most notably for PD1 and PD2. The pulse width (FWHM) of PD1 is close to 30 ps with 3 mW of optical power, but broadens to over 150 ps at 18 mW with a peak amplitude of 1.3 V. This time shift is evidence of a saturation-induced phase delay happening within the photodetector. This would be expected for a photodiode that saturates quickly as incident power increases. PD2 goes from about 20 ps at 2.6 mW to nearly 50 ps at 16 mW with 1.75 V peak voltage. With the GRIN lens coupling into the diode, PD2 shows less broadening and a slightly higher peak amplitude, an indication that the more uniform illumination of the diode has improved the saturation somewhat. PD3 shows less phase delay than PD1 and PD2, gaining only two or three picoseconds of width and staying near 30 ps at 3 mW up through 18 mW. It also exhibits a higher output voltage with a given optical power, reaching 3.6 V at 18 mW. This shows that the structural differences in the photodiodes decrease the peak current density and reduce the saturation-induced delays, which ultimately give rise to AM-to-PM conversion [45] [46] [117].

Similar measurements were made with the UTC photodiodes from the University of Virginia with the 1550 nm Er:Fiber laser. The MUTC photodiodes are connected to the laser source as in Figure 3.14 with an in-line fiber attenuator before the diode for power control. The voltage output

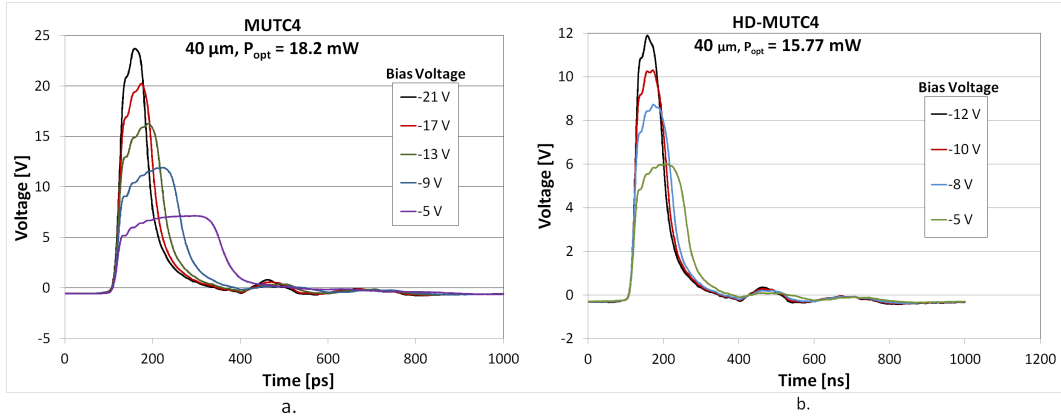


Figure 5.2: Impulse response for a. MUTC4, 40  $\mu\text{m}$  diode, incident optical power  $P_{opt} = 18.2 \text{ mW}$ , b. Impulse response for HD-MUTC4, 40  $\mu\text{m}$  diode, incident optical power  $P_{opt} = 15.77 \text{ mW}$ .

coming from the bias tee passes through approximately 2 m of DC-50 GHz microwave cables. The pulsewidth of the incoming pulses is around 1 ps. In most cases, due to the high output of these diodes, the peak voltage exceeds the limit of the oscilloscope, and 20 to 30 dB of attenuators are used at the oscilloscope input. The loss through these cables, the bias tee, the cable from the probe tip, and any attenuators has been removed. Also, since these photodiodes are not internally terminated, the voltage is generated by all the AC photocurrent across the internal 50  $\Omega$  resistor of the oscilloscope.

Figure 5.2a shows the effects of increasing the bias voltage across MUTC4 for 18.2 mW of 1550 nm, 250 MHz repetition rate light from the Er:Fiber laser. The uni-traveling carrier (UTC) diodes are built to handle high bias voltage, which offsets the space charge screening due to higher input power. As bias voltage increases, pulse width decreases, from 300 ps at  $V_b = -5 \text{ V}$  to 50 ps at  $V_b = -21 \text{ V}$ , and peak voltage increases from 7 V to 23.5 V. This plot also demonstrates the effects of the internal structure of the modified UTC diodes. As described in Section 3.2.2, the MUTC structure is designed for high power and high speed; as a result, the added “cliff layer” produces a larger saturation current that must be counteracted by high bias voltage. This effect is seen clearly in the impulse response.

Likewise, the highly doped, or HD, MUTCs are built for higher linearity, but this is at the

expense of responsivity. This impulse response plot for HD-MUTC4 in Figure 5.2b shows that the pulse width is not as wide as the regular modified UTC shown in Fig. 5.2a. At  $V_b = -5$  V, the pulse is around 150 ps, and at  $V_b = -12$  V is about 65 ps. However, it is also clear that the peak voltage is not as large, though the incident optical power is only 2.5 mW less. For 18.2 mW and  $V_b = -13$  V, MUTC4 has a peak voltage of 16 V, while HD-MUCT4 has a peak voltage of just under 12 V at  $V_b = -12$  V. This is to be expected of a lower responsivity photodiode.

Impulse response is a tool for directly observing saturation and linearity in the time domain. It will also be shown in Section 5.3.3.1 how the impulse response can be used directly for analysis of amplitude-to-phase conversion.

## 5.2 Saturation and Repetition Rate

In the preceding section, we saw the effects of saturation in the time domain with the impulse response. Saturation can also be manifest in the frequency domain, particularly as the microwave power in a particular harmonic is observed to no longer increase as the optical power onto the photodiode is increased.

The repetition rate of the frequency divider plays a large role in saturation. For a lower repetition rate, the energy per pulse is larger, causing more rapid saturation of the microwave signal from the photodiode [118] [113]. A higher repetition rate spreads the energy over more frequent, less energetic pulses, and reduces saturation. Mode-locked frequency dividers with a repetition rate on the order of a gigahertz, such as Ti:S, have an advantage in this regard to fiber lasers with rep rates on the order of tens to a few hundred megahertz. This drawback for fiber lasers can be overcome by multiplication of the pulse repetition rate. Similar techniques can also be done for Ti:S, further improving its performance as well.

### 5.2.1 Reduced photodiode saturation with Er:Fiber laser via rep rate multiplication

As described in Chapter 2, Er:Fiber lasers are limited to lower repetition rates primarily due to the long fiber laser cavities required to attain sufficient gain. Low repetition rates cause faster saturation in photodiodes, but improvement in photodetection performance has been achieved by increasing the mode spacing with cavity filtering and rep rate multiplication [113] [119]. The two methods for multiplying the repetition of an Er: fiber laser–Fabry-Perot cavities and cascaded Mach Zehnder Interferometers–are discussed below.

### 5.2.2 Fabry-Perot filter cavity

Figure 5.3 shows the scheme of a Fabry-Perot mode-filtering cavity. The cavity is composed of two concave mirrors with a radius of curvature of 50 cm and a reflectivity of 97%, corresponding to a finesse of about 100. For a free spectral range (FSR) of 5 GHz, the mirror separation (cavity length) is set at about 3 cm. In order to obtain a large transmission signal, the input beam profile is optimized with lenses to match the lowest order spatial cavity mode (TEM<sub>00</sub>). One mirror of the cavity is glued to a ring-shaped piezoelectric transducer (PZT), which enables cavity length control using a tilt lock [120]. A pick-off mirror with a reflectivity of a few percent is used to direct light reflected from the cavity onto a quadrant detector, which gives an error signal based on the spatial mode distribution of the reflected optical signal. This is used for locking the cavity length to a harmonic of the laser repetition rate. This method avoids the additional modulation of the cavity length (or input laser) as required by a dither lock.

With the 250 MHz input of the Er:Fiber laser, the resulting output of the cavity filter is a thinned frequency comb with only one out of every twenty input modes transmitted. In the time domain, this corresponds to a 4-ns pulse circulating in the cavity multiple times to produce a 5-GHz repetition rate (200 ps) signal (see Figure 5.4).

While this method does produce the desired higher repetition rate signal, it is rather ineffi-

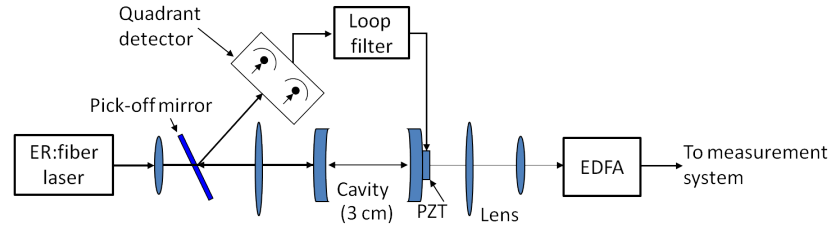


Figure 5.3: Schematic of Fabry-Perot (PF) cavity. EDFA is an erbium doped fiber amplifier.

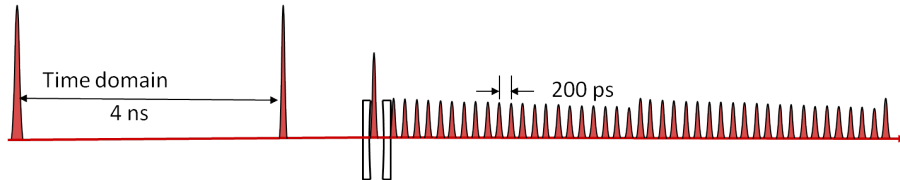


Figure 5.4: Depiction of the multiplication of the 250-MHz Er:f pulse rate inside a 5 GHz FP cavity.

cient. In the ideal case, for a 250-MHz input, the 5-GHz cavity transmits only 5% of the incident power [113]. Additional loss results from coupling back into optical fiber and a trade-off between high transmission of the TEM<sub>00</sub> mode and good error signal. The error signal of the tilt lock is obtained from interference between the TEM<sub>00</sub> mode and a higher-order mode of the cavity. Thus, a larger slope of error signal (and higher signal-to-noise ratio of the control loop) corresponds to more power coupled into the higher order mode. Consequently, to avoid degradation in system performance from limited signal-to-noise in the control loop, the coupling to the TEM<sub>00</sub> mode is decreased to provide improvement of error-signal sensitivity. As a result of these effects, only 1.2 mW of the incident 90 mW optical power is coupled into the fiber after the cavity. A commercial erbium-doped fiber amplifier (EDFA), shown in Figure 5.3, is used to subsequently increase the optical signal.

### 5.2.3 Mach-Zehnder Interferometer

Another repetition rate multiplication scheme is based on a series of cascaded Mach Zehnder Interferometers (MZI), which split the input and then delay and temporarily interleave the pulse trains from the two interferometer arms (see Figure 5.5) [119] [121] [122]. Here, standard four-port

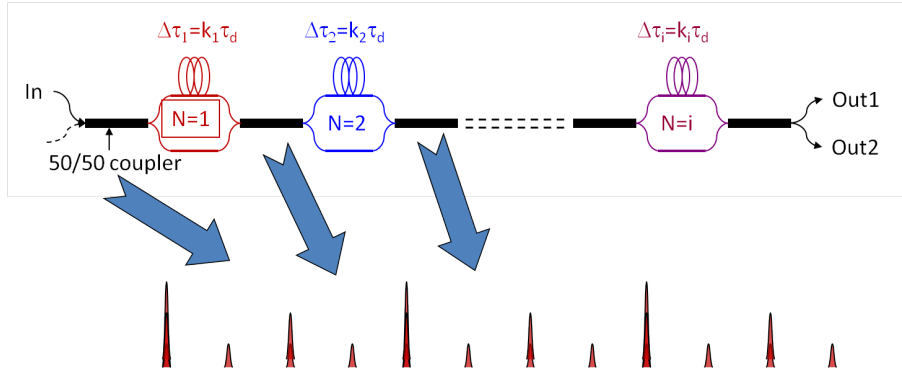


Figure 5.5: Schematic of fiber-based Mach-Zehnder interferometer (MZI) for multiplication of the repetition rate.

50/50 fiber couplers are employed with the two outputs of each stage serving as the inputs to the next stage. As a result, even with inexpensive off-the-shelf couplers, the transmission efficiency from a single output after a few stages can easily reach greater than 40%, which is much greater than that of the mode-filtering cavity approach. In principle, the second output could drive a second photodiode, and the signals could be summed electronically to potentially recover the benefit of the full optical power. Although called an interferometer here, direct temporal overlap of the pulses from the two arms of each stage of the MZI is actually avoided; this reduces significant noise related to optical phase variation. Each MZI stage increases the number of pulses in the output by a factor of two but does not necessarily double the repetition rate. By selecting a set of proper values of  $k_1, k_2, \dots, k_i$ , integers that set the delay in each stage, we can satisfy the condition of no pulses overlapping and all pulses contributing in phase to the desired 10-GHz signal. Trimming and splicing of the fiber delay in the interferometer arms is accomplished with the aid of a high-speed oscilloscope, and satisfactory tolerances below 5 ps ( $\sim 1$  mm of fiber) are achieved.

Figure 5.6 shows the PD2 output signal in the time and frequency domains with the 3-cm FP cavity (5 GHz repetition rate) and a four-stage MZI with  $k_1 = 20$ ,  $k_2 = 10$ ,  $k_3 = 5$ , and  $k_4 = 2$ . The time domain signals are measured with a 20 GHz oscilloscope, while the spectra are obtained with a spectrum analyzer. The incident power is about 3.5 mW in all cases. In the case of the FP cavity, the microwave spectrum shows suppression of unwanted modes, consistent with the finesse of the

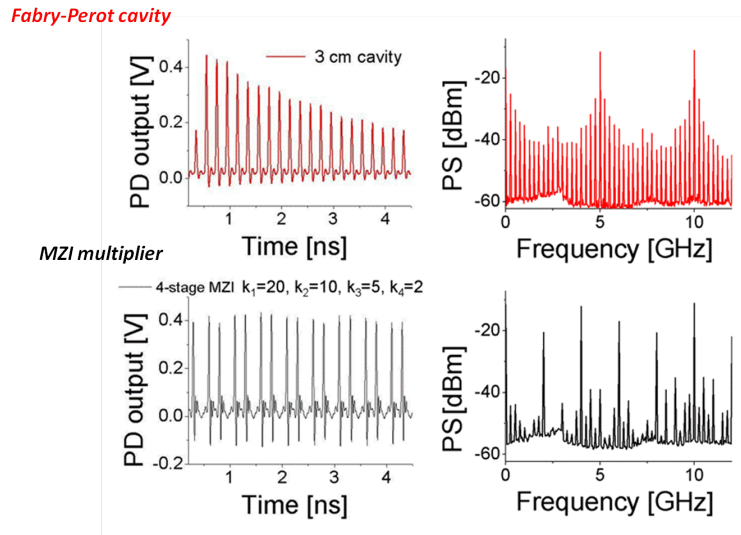


Figure 5.6: PD2 output in time and frequency domain with 3 cm/5 GHz FP cavity and a four-stage MZI. The optical power in all cases is 3.5 mW; PS denotes power spectrum.

cavity. In contrast, the spectrum of the output from the four-stage MZI is much more irregular, with the details dependent on the exact delay values in the various stages. Despite these marked differences, the 10-GHz signal size is approximately 11 dBm in both cases. This level is well in agreement with the fact that the alternating current (AC) power at a harmonic frequency is twice that of the direct current (DC) power for a narrow pulse train [123]. It indicates that all pulses are well aligned in phase to the 10-GHz signal so that they all have the maximum contribution to the desired 10-GHz frequency.

The improvement in 10-GHz power output from PD2 for different FP and MZI configurations is shown in Fig. 5.7(a). Here, the measured power in the 10-GHz harmonic from the photodiode is plotted versus the incident optical power. The pulse rate multiplication methods enhance the maximum achieved signal size by nearly 20 dB. With both the four-stage MZI and 3-cm cavity, we see no evidence of photodiode saturation, and the 10-GHz power increases with the expected slope of 20 dB per decade. In this case, and for all four Discovery diodes, the incident power is limited below 20 mW, or about 13 mA, to avoid damaging the photodiode.

Fig. 5.7(b) shows the expected noise floors calculated by use of Eq. 4.16 and Eq. 4.21, with

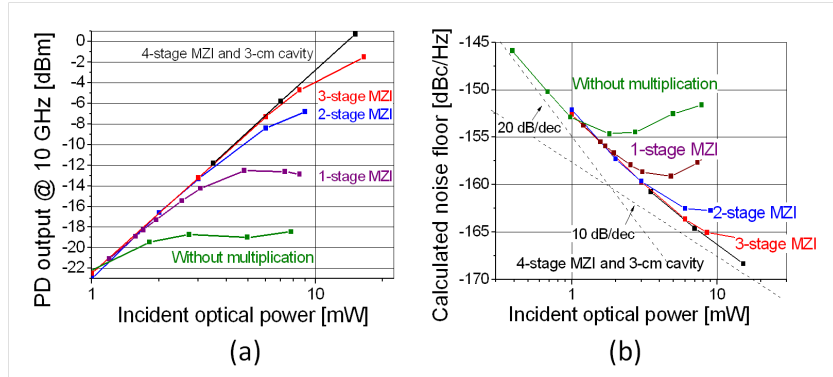


Figure 5.7: a. Signal size for PD2 at 10 GHz, Er:fiber, versus incident optical power. b. Predicted  $\mathcal{L}(f)$  given by Eq. 4.16 and Eq. 4.21. Dashed lines are the contributions of the thermal and shot noise with slopes of 20 dB per decade (dB/dec) and 10 dB/dec, respectively. The results of the four-stage MZI and 3-cm FP cavity are nearly identical and are therefore shown as a single curve in these figures.

$P_0$  obtained from the data of Fig. 5.7(a). At low incident power, the thermal noise dominates, and the noise floor improves at a rate of 20 dB per decade. Above a few milliwatts of optical power, the noise floor is limited by shot noise, and the noise floor improvement with incident power is reduced to 10 dB per decade. As will be shown in Chapter 6, the increased signal power from repetition rate multiplication will translate into an actual reduction in the phase noise floor that is in line with the predictions of Fig. 5.7(b).

Repetition rate multiplication also substantially improves signal power with MUTC diodes. Figure 5.8 shows the 10 GHz signal power of three 34- $\mu\text{m}$  MUTC diodes operated at -9 V bias with the unfiltered (250 MHz) Er:fiber signal and the cavity-filtered signal (5 GHz). A twenty-fold increase in the repetition rate yields a 30 dB increase in signal size. Since these photodiodes are built to handle higher power and photocurrent than the Discovery diodes, we are also able to increase the incident optical power to over 100 mW to see the onset of saturation between 30 to 50 mA. Such high signal powers are unprecedented in our work and in some cases eliminates the need for amplification before or after photodetection, which is significant since amplifiers can add noise on the signal. Furthermore, the increased signal will translate into a reduction in the phase noise, as will be shown in Chapter 6.

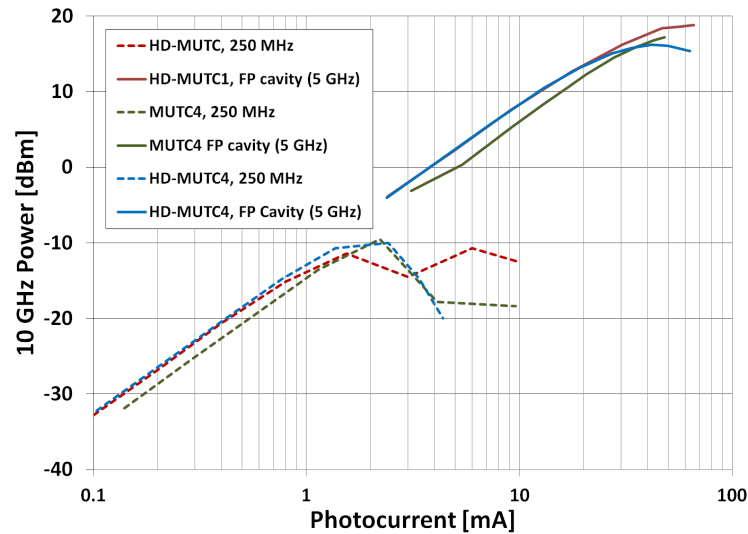


Figure 5.8: Signal size for MUTC diodes at 10 GHz, Er:fiber, versus photocurrent with and without repetition rate multiplication.

### 5.2.3.1 Saturation with Ti:Sapphire laser

Repetition rate multiplication can also be done to improve saturation for the Ti:Sapphire laser. A Mach-Zehnder interferometer is straightforward to construct in this free-space system; Figure 5.9 shows such a system constructed in the Ti:S laser. Using a polarizing beam splitter (PBS), approximately half the light is sent along a path that is half the length of the path traveled by the remainder of the beam. The exact path length difference between the two arms is tuned with a mechanical delay. When the beams are recombined on a second PBS, this results in an output signal that is multiplied by two, from 1 GHz to 2 GHz. Note that in this case the two interleaved pulse trains are orthogonally polarized. Moreover, due to the use of polarizing beamsplitters, all of the power exits a single port of the second PBS.

Figure 5.10 shows the 10 GHz power for MUCT3 and PD4 with 1 GHz and 2 GHz repetition rates for Ti:S.

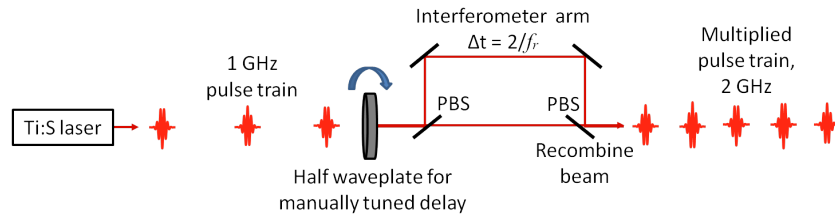


Figure 5.9: Schematic of free-space MZI in Ti:S laser.

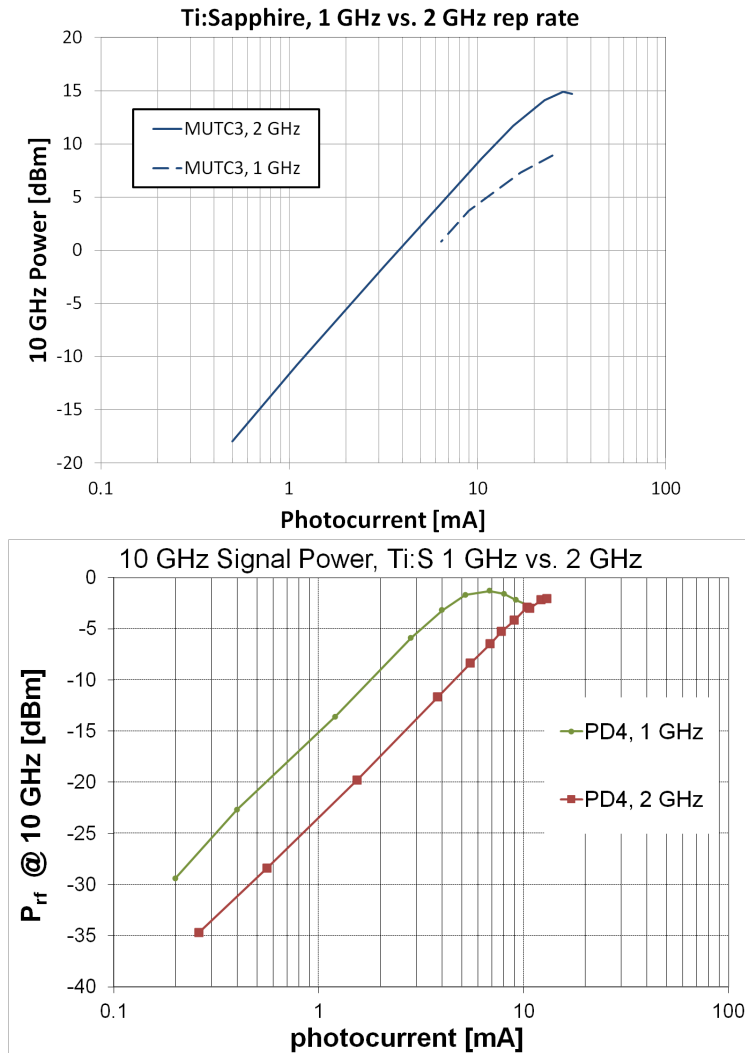


Figure 5.10: 10 GHz power for MUTC3 and PD4 on Ti:S with 1 GHz rep rate and MZI-multiplied 2 GHz rep rate.

### 5.3 Amplitude-to-Phase Conversion

As mentioned in Section 4.2.3, we define an AM-to-PM coefficient,  $\alpha$ , as the induced RMS phase variation arising from a fractional power fluctuation ( $\Delta P/P_0$ ). While  $\alpha$  could be generally

defined and measured for any frequency, we restrict most of our attention to the 10 GHz harmonic of the generated photocurrent. In order to calculate this coefficient, one must measure RMS phase fluctuations on the microwave signal from the photodiode in response to power modulation on the incident light. Here, we present two measurement techniques, which are described in detail in the following sections.

### 5.3.1 Phase Bridge Measurement System

Our primary technique for measuring amplitude-to-phase conversion employs a microwave phase bridge that permits the direct measurement of phase fluctuations relative to a stable 10 GHz reference with low uncertainty and high resolution (limited ultimately by fundamental thermal and shot noise). Variations of this well-developed technique have been previously applied to the measurement of saturation effects and AM-to-PM in photodiodes [43] [44] [45] [117] as well as intrinsic  $1/f$  noise [44] [47]. The phase bridge approach has the advantage of being a high precision measurement, capable of measurement at the thermal noise limit with sub-femtosecond timing precision in narrow resolution bandwidths. A phase bridge is a microwave technique that allows sensitive relative measurement of phase and amplitude noise [124] [125]. Variations of this method relating to noise in photodiodes have been demonstrated previously [43] [44] [45] [47]. Two different phase bridge measurement systems were used in this analysis and are described below.

The first phase bridge method is based on setting the two arms in quadrature; it is most similar to that found in [45] with the main difference being the control of the laser repetition rate versus the reference synthesizer frequency. The block diagrams of our system with the Ti:S and Er:F lasers are shown in Figure 5.11. The repetition rate ( $f_{rep}$ ) of the laser, which is around 1 GHz for Ti:S and 250 MHz for Er:F, is mixed with a 1 GHz or 250 MHz signal, respectively, from a hydrogen maser-referenced synthesizer. This beat signal is fed into a loop filter servo and used to phase lock  $f_{rep}$  to the synthesizer frequency using piezo-based control of the laser cavity length. The carrier-envelope offset frequency,  $f_0$ , of the laser can also be controlled [126], although it is typically left unlocked for this measurement.

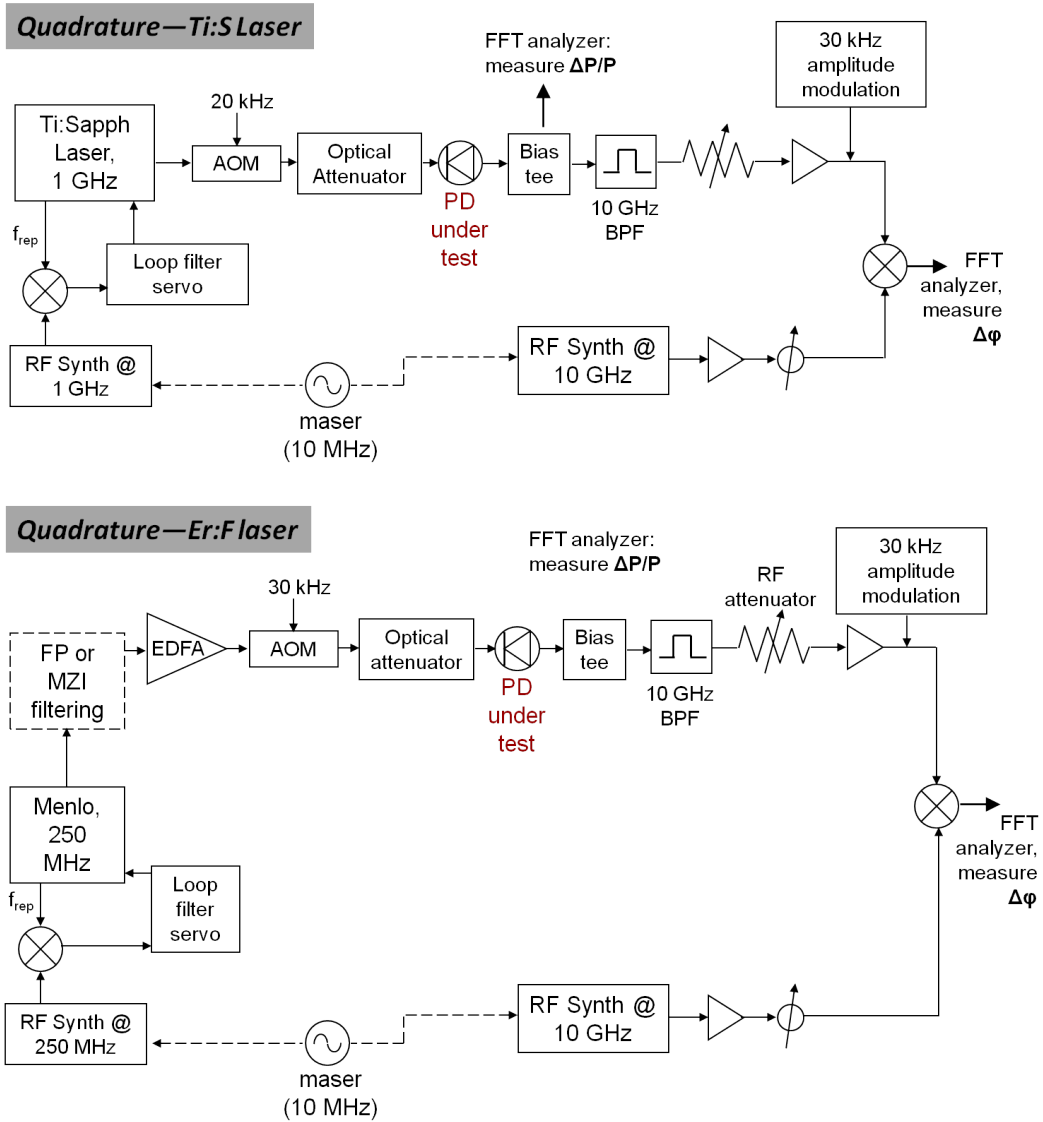


Figure 5.11: Block diagram of quadrature phase bridge measurement set-up for Ti:S and Er:F laser systems.

For the Er:F laser, multiplication of the repetition rate can be done at this point with an FP cavity or MZI if desired. Filtered or unfiltered, the signal is then amplified in an EDFA. The final laser output is sent through an acousto-optic modulator (AOM), which adds a known 20 kHz amplitude modulation on the laser light. Since AM-to-PM conversion in the photodiode changes some amount of this amplitude modulation into phase modulation, we monitor this spectral tone to quantify this conversion. The modulated beam goes through optical attenuator that is used to control the average optical power on the photodiode. At this point, the Ti:S beam is coupled into fiber. The signal in fiber is then connected to the fiber pigtailed photodiode, as shown in Figures 3.12 and 3.14 in Section 3.2. As we will discuss in later in this section, it is important to note that changing the fiber configuration in the system can affect AM-to-PM as well.

For the DSC diodes, a bias tee at the output of the PD allows us to monitor the average DC voltage drop across the  $50\ \Omega$  load resistor (and thus the photocurrent generated by the photodiode) on a high-impedance voltmeter while allowing frequency components of the signal  $>80$  kHz to pass through to the rest of the measurement system. The 20 kHz tone from the AOM can also be monitored from the low frequency port of the bias tee. For the UVA diodes, which do not have an internal load resistor, a Keithley sourcemeter is used to monitor the average photocurrent and set the bias voltage. An external  $10\ \Omega$  series resistor is added in the electrical path of the bias, and a differential amplifier (un-grounded on the input side) is used to monitor the voltage changes associated with the 20 kHz tone across this  $10\ \Omega$  resistor.

The high frequency signal is bandpass filtered around the tenth harmonic at 10 GHz. Following the filter, a combination of a microwave attenuator and low noise amplifier is used to keep the power of the signal at the LO port of the mixer constant while the optical power is being attenuated using the optical attenuator. This ensures a constant mixer gain factor of  $k_d = 0.47\ \text{V/rad}$ , allowing us to convert voltage fluctuations to phase fluctuations.

The reference arm of the phase bridge is from a second maser-referenced synthesizer with its frequency set to match the 10 GHz signal in the test arm. A second photodiode using the same pulsed signal is not used in order to isolate only the AM-to-PM of one photodiode. Proper tuning

of the relative phase between signals at the RF and LO ports of the mixer results in amplitude-insensitive detection. This is accomplished by adding a pure 30 kHz amplitude modulation to the amplified signal using a signal generator and a passive amplitude/phase modulator [127]. The phase shifter is then adjusted so that the 30 kHz tone, as seen on the FFT analyzer, is minimized. We note that this does not necessarily correspond to a minimum in voltage of the mixer output [89]. At this point, the measurement system is sensitive only to phase modulation in the test signal arising from any photodiode amplitude-to-phase conversion of the 20 kHz modulation on the light.

The RMS voltage of the initial 20 kHz modulation is measured on the FFT analyzer from the output of the bias tee and then divided by the average voltage to yield the normalized amplitude noise. The RMS voltage of the 20 kHz tone from the output of the mixer, which contains any phase modulation from AM-to-PM conversion in the PD, is then measured on the FFT analyzer and converted to radians using the gain factor  $k_d$ . The ratio of the two gives us the AM-to-PM conversion factor  $\alpha$  for this method.

The second phase bridge method is similar to the previous method; however, the frequencies of the two arms are offset by a fixed frequency instead of being kept the same [116]. The block diagram for this alternative setup is shown in Figure 5.12. The laser signal onto the photodiode remains unchanged, as well as the bias tee and the bandpass filter selecting the 10 GHz harmonic. The attenuator and amplifier pair is used now to keep this arm at a low power, between -20 and -25 dBm, into the mixer.

In the second arm, the synthesizer is now set to 10.001 GHz, 1 MHz different from the 10 GHz tone selected by the bandpass filter in the first arm. This 10 dBm signal is sent to the mixer, resulting in a 1 MHz beat signal out of the mixer. There is no need to set the two arms in a particular phase relative to each other or to calibrate an injected AM signal, making this a more straightforward and stable measurement than the quadrature method. The beat signal is sent to the FFT analyzer, where an analog demodulation mode is used to track phase fluctuations directly with no need to convert using  $k_d$ . These two methods were compared in our lab and shown to reproduce the same results. They have been used interchangeably to obtain the data shown.

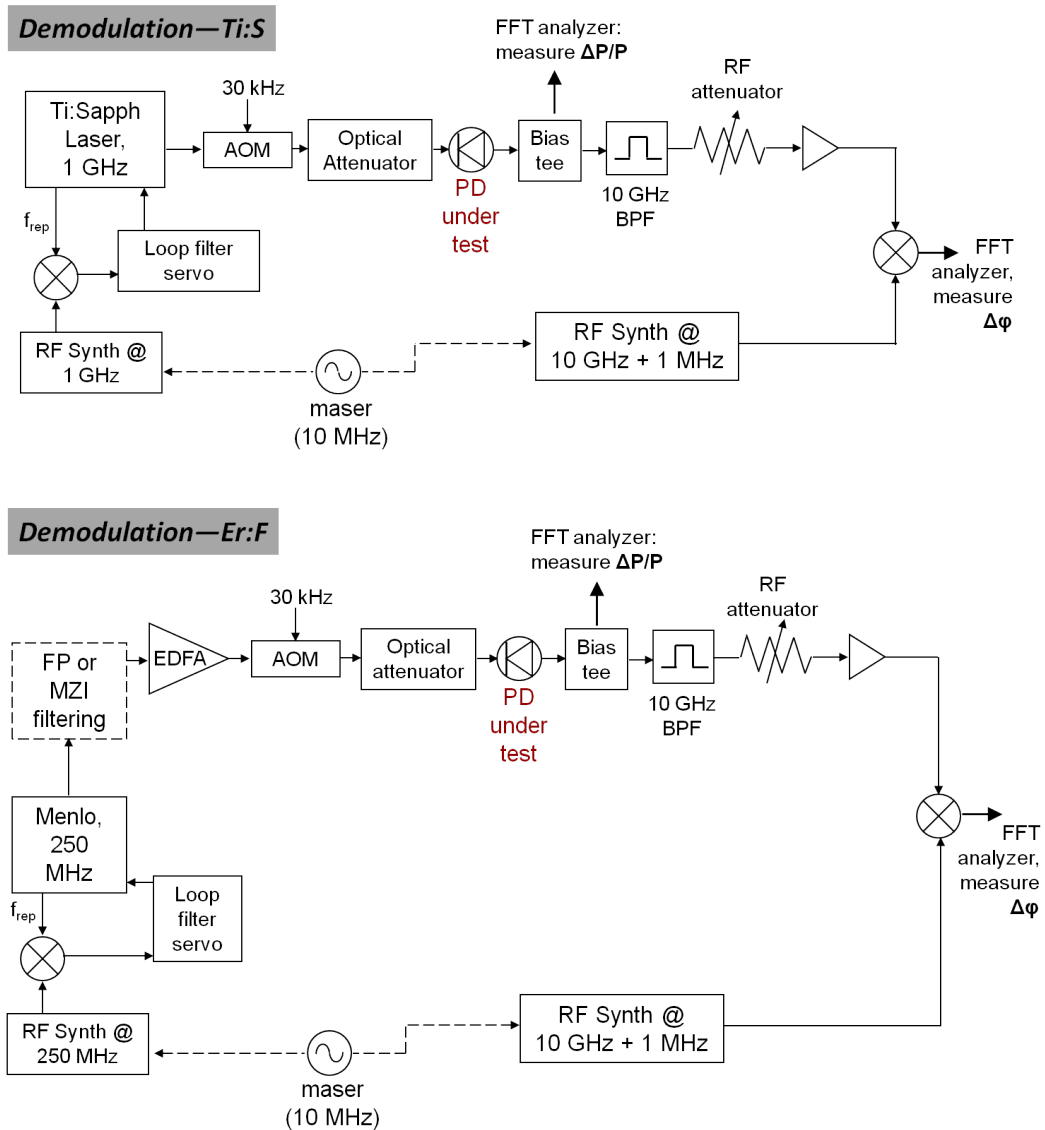


Figure 5.12: Block diagram of demodulation phase bridge measurement set-up for Ti:S and Er:F laser systems.

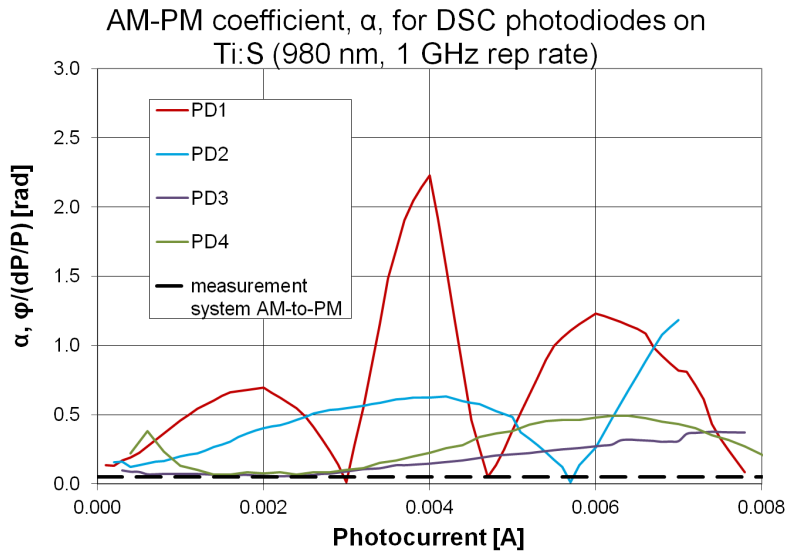


Figure 5.13: Average power-to-phase conversion factor,  $\alpha$ , for four DSC photodiodes on Ti:S laser.

### 5.3.2 AM-to-PM Results

Figure 5.13 shows the measurement of  $\alpha$  for the four DSC photodiodes at the Ti:S wavelength of 980 nm using the phase bridge method. PD2, PD3, and PD4 show consistently lower  $\alpha$  across a wide range of photocurrent than PD1. This is consistent with the design parameters of these photodiodes described in Chapter 3, which were implemented to reduce current density, saturation, and related nonlinear effects. The impulse response measurements shown in Section 5.1 confirm the higher power handling capability of PD2 and PD3 relative to PD1. The implication of these measurements is that reduction in photodiode nonlinearity indeed results in reduced AM-to-PM conversion. Low AM-to-PM at the largest photocurrent is especially desirable from the point of view of minimizing the shot-noise floor of generated microwave signals [114] [113]. In this regard,  $\alpha$  for PD3 and PD4 is below 0.5 rad up to a photocurrent of nearly 8 mA. The dashed black line indicates the measurement floor of the system; that is, how much AM-to-PM is present in the microwave components without the photodiodes. This is determined by using a 10 GHz synthesizer in place of the laser and photodiode in the phase bridge and measuring the AM-to-PM at varying signal power.

The most striking feature in the data of Figure 5.13 is the presence of nulls in the measured  $\alpha$  of PD1 and PD2, indicating photocurrents where AM-to-PM conversion approaches zero. It is important to note that our measurements do not determine the sign of the phase response to amplitude modulation (e.g., whether the 10 GHz phase is advanced or delayed with increasing power). Thus, the nulls are more correctly interpreted as zero crossings in the AM-to-PM response of the photodiode. Such nulls were also observed in earlier measurements [45] and at that time were attributed to impedance mismatch in the microwave components following the photodiode. However, the nulls are consistently observed near the same average photocurrent irrespective of the exact lengths of microwave cables and the configuration of other components. As discussed in Section 4.2.3, a simple model of pulse energies given in Ref. [116] recreates this phenomenon. From a physical picture, this could indicate that there are competing power-dependent processes related to space-charge screening and the time delay of the removal of photocarriers, which apparently precisely cancel each other at specific photocurrents [114] [128] [129]. A fundamental understanding of these processes and their interactions does not yet exist, but one can still use the information given by a measurement of  $\alpha$  to pick ideal photodiodes and operating parameters for a particular application. The advantage of operating the photodiode at one of these nulls is discussed in greater detail in Section 5.3.3.

The frequency dependence of AM-to-PM conversion can clearly be seen by changing the repetition rate of the laser. A lower repetition rate signal, such as 250 MHz for the Er: fiber laser, generates nulls much closer together than those given by a higher repetition rate signal. This is seen in Figure 5.14 where  $\alpha$  for PD1 is shown for the same Er:F laser with the normal 250 MHz repetition rate and also with the 5 GHz FP cavity. AM-to-PM conversion at 250 MHz rep rate (red curve) shows many fluctuations and nulls, while at 5 GHz (orange curve) only one null is seen within the range of photocurrent.

Figure 5.13 also shows a reduction in nulls with modified photodiode structure measured with the same 1 GHz repetition rate. PD1, with no special modification, exhibits three pronounced nulls in its range of photocurrent; PD2 has one null at a higher photocurrent, and PD3 and

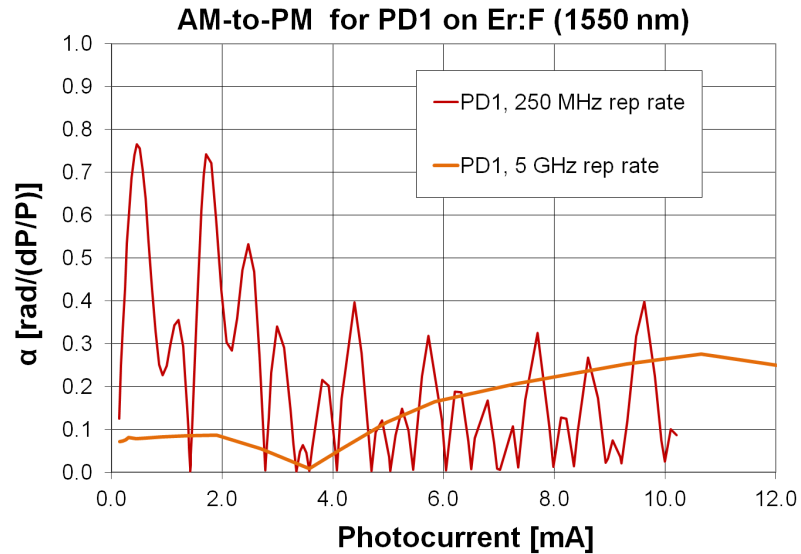


Figure 5.14: AM-to-PM conversion with repetition rate multiplication.

PD4 do not show very distinct nulls. It is also notable that nulls are most often observed at a photocurrent higher than the compression photocurrent associated with saturation. As previously discussed, increased repetition rate and improved photodiode structure are techniques used to improve saturation. Figures 5.13 and 5.14 suggest that this improvement in saturation appears to be the cause for spreading out the nulls and pushing the first null to a higher value of photocurrent.

Due to the great number of possible nulls, measurement of  $\alpha$  at a lower repetition rate can be challenging. Optical power onto the photodiode is manually decreased in incremental steps; the interval of the steps can be larger for a faster, more general measurement across the range of available optical power, or the steps can be much smaller, generating a much higher resolution but taking much longer. Even with steps very close together, nulls or peaks might occur at some power between those measured, giving an artificially smoothed result. The measurements of  $\alpha$  at 250 MHz presented in Figure 5.14 have been taken with small intervals (on the order of tenths of milliwatts) to preserve as much of the structure as possible, though some washing out might occur (possibly seen below 2 mA).

In principle, operating at a null for  $\alpha$  would be ideal for experiments focused on the generation

of low phase noise microwaves, particularly if a laser with large amplitude fluctuations is being used. However, we have observed that these nulls can move to higher or lower photocurrent depending on specific operating parameters. For example, external factors such as temperature, bias voltage, and the shape of the optical mode of the light out of the fiber can impact the exact position of the nulls. We observed displacements of the nulls by about half a milliamp by changing the external temperature by 10 °C or the bias voltage from 9 V to 5 V. At times, this shift can be large enough such that a photocurrent that once resulted in a null now results in  $\alpha$  sitting at or near a peak. This would make the conversion of amplitude to phase even worse than intended, and the shift would likely be undetected unless constantly monitored.

Another effect that can cause shifts in the location of nulls is the shape of the modes incident onto the photodiode. Figure 5.15 specifically illustrates the effect of optical mode shaping for PD1 with an SMF-28 fiber pigtail on Ti:S. Because SMF-28 is multimode at the 980 nm operating wavelength, the light can occupy several higher order modes of the fiber waveguide. By tightly coiling the fiber in loops of approximately 1 cm in diameter, these higher order modes can be reduced, thereby changing the illumination of the photodiode. While the mode structure was not rigorously analyzed, this simple example illustrates that changes in the spatial illumination a photodiode can move the placement of nulls by almost 0.5 mA, while the overall structure of  $\alpha$  versus photocurrent is unchanged. Of course, a potential variation such as this can be largely solved by employing fiber which is purely single mode at the illumination wavelength.

### 5.3.3 Prediction of Phase noise from RIN using $\alpha$

Another important result of quantifying AM-to-PM conversion is the ability to predict the impact of laser relative intensity noise (RIN) on the phase noise of a 10 GHz microwave signal from a frequency-stabilized repetitive pulse train. Knowing the laser RIN (measured in dBc/Hz), the predicted contribution of AM-to-PM to the single sideband phase noise is given by

$$\mathcal{L}_{\text{RIN}}(f) = \text{RIN} + 20 \log(\alpha) - 3 \text{ dB}. \quad (5.1)$$

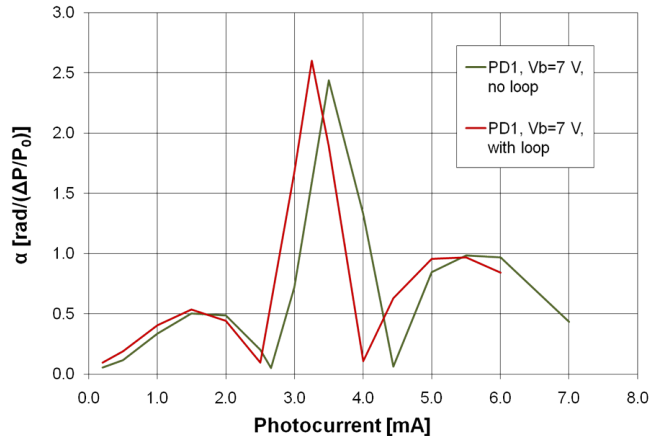


Figure 5.15: Phase bridge results for PD1 on Ti:S (980 nm) with changes in shape of the optical mode incident on the detector due to the creation of  $\sim 1$  cm loops in the optical fiber. Note large shifts of nulls and peaks.

To test the predictive utility of our measurements, a residual phase noise measurement on the 10 GHz harmonic was done with PD1 and PD2 and compared to the prediction based on the laser RIN and measured values of  $\alpha$ . The RIN of the Ti:S laser employed in this work is shown in Figure 5.16a. It was measured with the offset frequency unlocked, causing the high AM from the pump laser in the 100 Hz to 1 kHz region to be visible. From Figure 5.13, the “worst case” AM-to-PM values for PD1 and PD2 are 2.3 rad and 0.6 rad, respectively, at 4 mA. Using these values and the RIN of Figure 5.16a, the anticipated phase noise was calculated (Figure 5.16b). Then, a residual phase noise measurement on the 10 GHz harmonic from each photodiode was made. A 50/50 fiber splitter sent half of the laser signal to the photodiode under test (PD1 or PD2) and half to a reference photodiode with a low, flat AM-to-PM coefficient. To insure the measurement was not limited by the noise floor, the laser power was adjusted so the photodiodes were at the “worst case” photocurrent. We compare those measurements to the predicted curves (Figure 5.16b). As seen, there is very good agreement between the estimate and the measurement in the high-AM region. Clearly, a good choice of photodetector and optimal operating parameters will ultimately reduce the phase noise. Using the above analysis, we can estimate the required laser RIN to achieve desired phase noise levels. For example, if the goal were to achieve 10 GHz microwave signals with

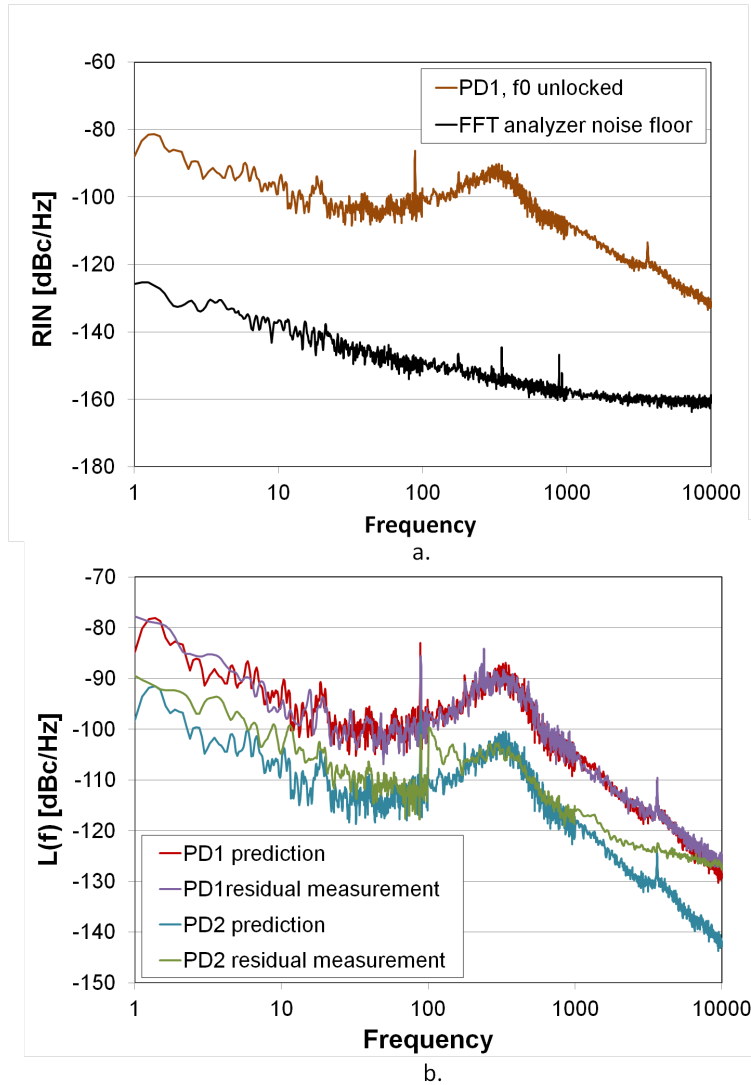


Figure 5.16: a. AM spectrum of the free-running Ti:S laser. b. Prediction of phase noise from laser AM spectrum (a). The “worst case” performance of PD1 and PD2 is multiplied by the AM spectrum in (a). The residual phase noise is measured at a photocurrent where PD1 and PD2 exhibit high AM-to-PM conversion (around 4 mA in Figure 5.13).

single sideband phase noise less than -100 dBc/Hz at 1 Hz offset (corresponding approximately to fractional frequency instability of  $1 \times 10^{-15}$ ), then the laser RIN would need to be at least as low at -83 dBc/Hz at the same offset if  $\alpha = 0.2$  rad. Operating any photodetector at a null has the potential to significantly reduce the impact of laser RIN on the microwave phase noise, if the location of the null can be retained without drifting.

### 5.3.3.1 Impulse Response (FWHM) Analysis

While the phase bridge approach is a high-precision measurement, the method comes with the cost of additional complexity. An alternative approach that employs more straightforward time-domain acquisition of data with an oscilloscope is described here. In this case, the time-domain electrical impulse response of the photodiode is measured with a high-speed sampling oscilloscope as in Section 5.1, and Fourier analysis is used to extract power-dependent phase shifts at a desired frequency [46]. A time-domain measurement has the benefit of a simplified measurement system, but it comes with the possibility of increased noise and ambiguity in data analysis. This approach measures the power-dependent phase, but requires differentiation to obtain the power-to-phase coefficient  $\alpha$ . It further requires the use of a high-speed sampling oscilloscope, which is a well-developed laboratory instrument, but whose intrinsic timing jitter also introduces measurement uncertainties. We note that approaches have been developed to measure and remove time-base errors in sampling oscilloscopes, yielding precision at the level of  $\sim 200$  fs [130] [131] [132]. The implementation of such time-base correction algorithms would likely decrease the uncertainty of the time-domain measurement presented here. Nonetheless, as will be shown, the results of the impulse response measurement agree with the phase-bridge measurement within a factor of two or less and lend increased confidence to the phase bridge results. A more detailed comparison of the measurement results will be given below.

Using Fourier analysis, we can extract phase information from the electrical impulse response of a photodiode to examine phase fluctuations that occur due to increasing the optical power incident on the photodiode [46]. This analysis is done for PD1, PD2, and PD3 on the 1 GHz Ti:S laser to illustrate the technique. These measurements employed a 20 GHz sampling oscilloscope, which is triggered by a second photodiode on which the optical power is kept constant. As already noted, timing errors intrinsic to sampling oscilloscopes have been studied and could be taken into account to improve this method [130] [131] [132]. Additionally, waveforms measured on the oscilloscope with and without a 10 dB attenuation between the photodiode and scope have the

same shape, indicating that any nonlinearity in the amplitude of the scope response is small [133]. Since we are interested in comparing the results in general, more detailed analysis of these effects will not be presented here.

The impulse responses for PD1, PD2, and PD3 were previously shown in Figure 5.1. The Fourier transform of the impulse response provides the RF phase in radians for a given Fourier frequency. Repeating this analysis for different average photocurrents yields the data of Figure 5.17a. The constant phase difference between the harmonics is largely arbitrary, arising from the impulse function being offset in time at the sampling oscilloscope (see Figure 5.17a); however, variations of the phase with photocurrent contain information about the AM-to-PM conversion. A cubic polynomial is fitted to the RF phase versus optical power, and the power-to-phase conversion (PPC) factor,  $d\phi/dP$  [rad/W], at a given optical power is the derivative of the fitted line with respect to average optical power at that point. An absolute value is taken, though in principle the sign of the relative phase could be determined. The AM-to-PM coefficient,  $\alpha$ , is generated by normalizing the derivative at each point with the power  $P_0$  at that point. Figure 5.17b demonstrates this analysis for three harmonics (1, 3, and 10 GHz) for PD3 at a reverse bias  $V_b = 9$  V. While only three harmonics are shown here, this approach has the benefit of providing information about all harmonics generated by the photodiode up to its cutoff frequency.

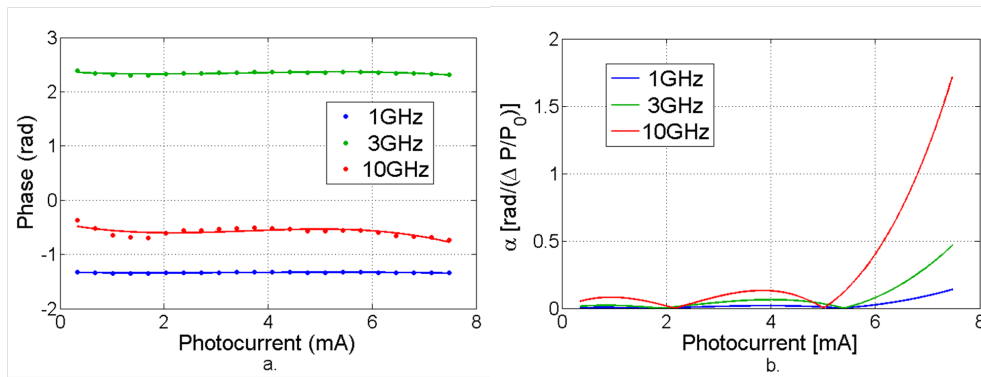


Figure 5.17: Fourier method as shown for PD3 at 9 V. (a) Phase (dots) is extracted from the Fourier transform of the impulse response at three Fourier frequencies, with cubic polynomial fits (solid lines). (b) Taking the derivative of phase with respect to power and then normalizing each point with its given optical power ( $P_0$ ) gives  $\alpha$ .

The results of the impulse response method for all three photodiodes are shown in Figure 5.18. Figure 5.18a shows  $\alpha$  calculated using the cubic polynomial fits, which approximate the shape of the phase changes and smooth possible noise in the data. A better fit and higher resolution can be obtained by taking more points close together (that is, changing optical power by smaller steps). The data go through one or two nulls and then rise to 1 rad or more at higher photocurrents. These nulls, given by derivatives of the cubic polynomial at an inflection point, were also seen in the direct measurement of  $\alpha$  with the phase bridge method for PD1 and PD2 (see Figure 5.13).

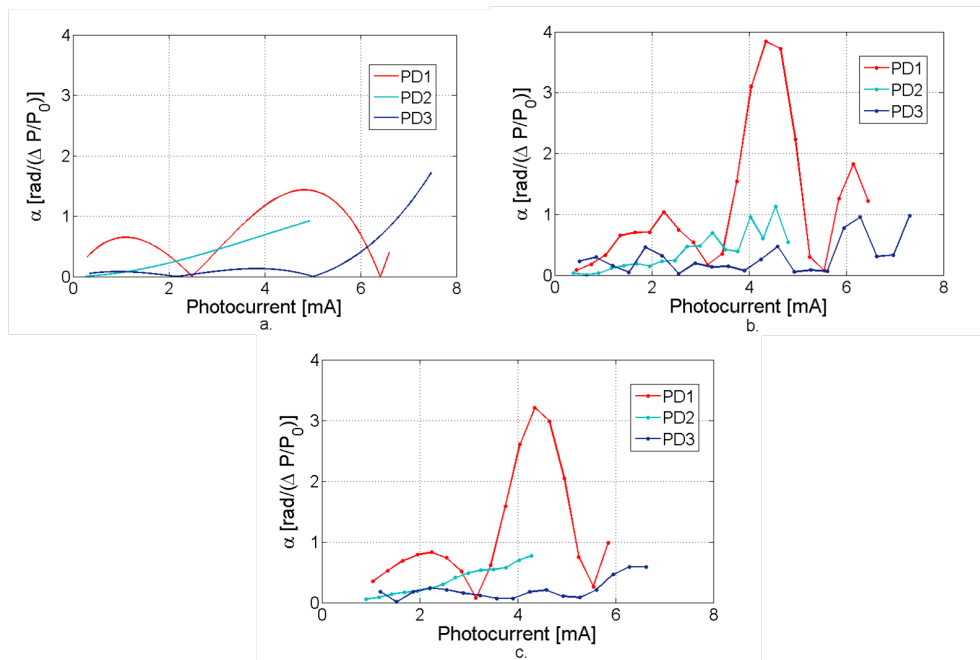


Figure 5.18: Compilation of magnitude of  $\alpha$  for the three photodiodes using a. impulse response with cubic fits, b. impulse response with point derivatives, c. impulse response with triangle filter.

In addition to using polynomial fits for derivatives, one also can generate the slope from a point-by-point derivative; that is, taking the “slope” of each pair of consecutive data points. This better represents the natural rise or fall of the phase with respect to power; however, this method is more susceptible to sudden, noisy jumps in the data. This method is shown in Figure 5.18b. We also see a large spike in  $\alpha$  for PD1 in Figure 5.18b near 4 mA, which corresponds almost exactly to the peak and nulls seen in Figure 5.13 with the phase bridge method. However, the relative  $\alpha$

levels for the three photodiodes are two times the levels given by the phase bridge method. This is likely due to the sensitivity of the point derivative method to jumps in the data.

To help minimize these jumps, one can also apply various types of numerical filters to smooth point derivatives. An in-depth analysis of these filters will not be presented here, but we briefly show the results of a simple triangle filter in Figure 5.18c. There is a reduction of the magnitude of  $\alpha$  to more closely reflect the phase bridge results to a factor of 1.5, while maintaining much of the general structure of the point derivative method.

The phase bridge and impulse response methods of measuring  $\alpha$  show agreement within a factor of two or less, in some cases matching exactly. As already noted, while the phase bridge techniques are considered to be more precise, the impulse response measurement has the advantage of simplified data acquisition. However, in our present implementation, this comes at the expense of increased noise and greater ambiguity in data analysis. Therefore, for generation of ultra-low phase noise microwave signals, the measurement of  $\alpha$  using one of the phase bridge methods is preferred.

## Chapter 6

### Demonstrations of Ultra-Low Phase Noise Microwave Signals

The goal of the optical-to-microwave generation scheme is to generate spectrally pure, low-phase noise 10 GHz signals that can be used in the applications described in the introduction. Having carefully assessed the noise limitations of each component of the photonic oscillator, we now examine the overall phase noise stability of a number of photonic oscillator and photodetection schemes to demonstrate ultra-low phase noise signals at a wide range of offset frequencies.

As presented in Section 4.1.2, phase noise is characterized by the Fourier decomposition of frequency fluctuations of a signal.  $S_\phi(f)$  is defined to be the spectral density of phase fluctuations at a Fourier frequency  $f$ , and  $S_y(f)$  is the spectral density of fractional frequency fluctuations; the relationship between the two is given in Equation 4.9. These are single-sideband, double-sided spectra. The standard measure of phase noise is  $\mathcal{L}(f)$ , a single-sided, single-sideband quantity defined to be half of  $S_\phi(f)$ :

$$\mathcal{L}(f) = \frac{1}{2}S_\phi(f). \quad (6.1)$$

$\mathcal{L}(f)$  (units of dBc/Hz) can also be thought of as a “noise to signal” ratio, as it compares the level of the noise to the level of the carrier. It is also typically converted from linear into logarithmic scale:

$$\mathcal{L}(f) = 10 \log \left[ \frac{1}{2}S_\phi(f) \right] = 10 \log \left[ \frac{P_{noise}}{P_{signal}} \right]. \quad (6.2)$$

$\mathcal{L}(f)$  for an oscillator is measured by comparing it to a reference oscillator of the same frequency in a phase bridge [124] [125]. The arms are set in quadrature (90 degrees phase difference)

by a phase shifter and are sent to the two inputs of a mixer. The resulting output is the short-term phase fluctuations between the oscillators appearing as voltage fluctuations from the mixer. An absolute phase noise measurement includes all of the noise from two independent sources, while a residual phase noise measurements typically excludes the noise contributions from the reference oscillator (cavity-stabilized laser in this case) enabling one to analyze the noise from other components in the system. The following sections show absolute and residual phase noise measurements for 10-GHz signals generated from optical frequency references and the relation of photodetector noise, as characterized in the previous chapter, to overall phase noise.

## 6.1 Absolute Phase Noise of Photonic Oscillator

As the microwaves generated from this photonic approach have a phase noise that is lower than that available from commercially available microwave references, characterization of the generated phase noise required two similar, but fully independent systems for an absolute phase noise comparison (see Figure 6.1). Known noise sources in all parts of the system were minimized as much as possible to achieve the lowest possible phase noise results. Both photonic oscillators were based on fiber and solid-state CW lasers that are frequency-stabilized to a single transverse and longitudinal mode of an optical cavity via the Pound-Drever-Hall locking scheme [57], as described in Chapter 2. The cavities were constructed of low-expansion ULE spacers with optically contacted high-reflectivity mirrors that exhibited a finesse of 200,000 and 300,000 for the 518 THz laser and the first harmonic of the 282 THz laser, respectively. In both systems, the intensity of the light incident on the high-finesse cavities was stabilized to minimize thermal instabilities of the cavity length due to heating of the mirrors. Mounting of the cavities and the cavity geometries themselves, although different, were both chosen to minimize the effects of accelerations on the optical cavity length. The design of the FP cavities for the 518 THz and 282 THz cavities were similar to those described in References [134], [76], and [36], respectively. To isolate the cavities from external perturbations, each cavity was held in a temperature-controlled evacuated chamber mounted on an active vibration stage inside an acoustic isolation enclosure. The light generated from the two

systems demonstrated optical linewidths of less than 1 Hz and a frequency instability of less than  $7 \times 10^{-16}$  at 1 s of averaging.

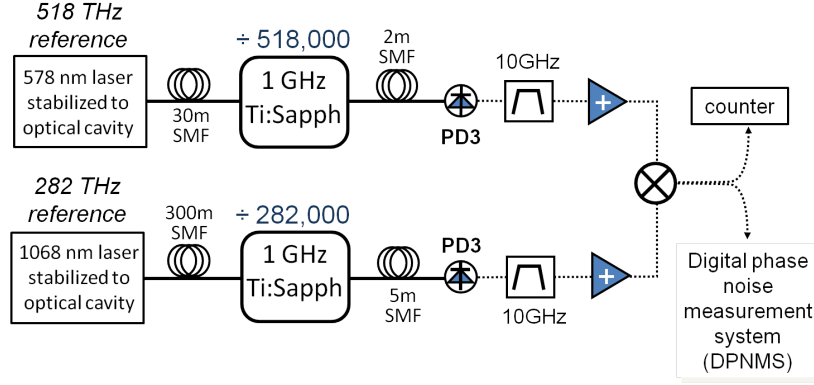


Figure 6.1: Schematic of the absolute phase noise measurement between two independent photonic oscillators.

The two optical reference cavities were located in laboratories  $\sim 300$  m apart on different floors of the NIST laboratory building; one was separated from the optical frequency combs (OFCs), both located in a third laboratory, by 30 m and the other by 300 m. The frequency-stabilized light from each optical cavity was transmitted (with negligible change in optical stability or phase noise) via stabilized fiber-optical links [80].

For the first measurements, both OFCs were 1 GHz Ti:S lasers located in the same laboratory. One laser system was located on a passively isolated optical table and enclosed in nested aluminum and plexiglass boxes. The second comb system was separated from the first by a few meters. It was enclosed in a free-standing isolation box that provided  $\sim 30$  dB of acoustic suppression. The base plate of this comb was isolated from seismic vibrations by a piezo-actuated platform. Each laser was pumped with  $\sim 8$  W of 532 nm light, and produced  $\sim 1$  W of mode-locked power. Both lasers produced an optical spectrum with usable bandwidth from 55 nm to 1,200 nm, allowing for  $f - 2f$  stabilization of  $f_0$  and the laser pump power [65]. A heterodyne beat between the CW laser frequency and a single mode of the self-referenced frequency comb provided the error signal used to control the cavity length with a piezoelectric actuated mirror [65].

The dual packaged PD3 with PMF pigtailed at 980 nm was chosen for photodetection due to

its low AM-to-PM conversion and higher saturation photocurrent. Light near 980 nm (with  $\sim 50$  nm bandwidth) was coupled to the photodiodes using a 5 m fiber-optical cable from one comb system and a 2 m fiber-optical cable from the second comb system. Approximately 12 mW of optical power incident on the photodiodes generated about -8 dBm in the 10 GHz carriers. The residual intensity noise (RIN) on this light was close to -100 dBc/Hz at 1 Hz offset, which was estimated to not significantly impact the present phase noise by AM-to-PM conversion in the photodiodes using the method in Section 5.3.3.

The schematic of the phase noise measurement system is shown in Figure 6.1. The signals generated from the two divided optical reference cavities are photodetected, and then this electronic signal is band-pass filtered to generate the ultimate 10 GHz signal. These signals are both amplified to between 0 dBm and 7 dBm for input to the mixer. The repetition rates of the two combs were adjusted so that the beat between the two 10 GHz signals is  $\sim 15$  MHz. This mixed-down signal is input to a digital phase-noise measurement system (DPNMS) to measure  $\mathcal{L}(f)$ ; the DPNMS does not require maintaining quadrature between the two arms. This measurement system uses cross-spectrum analysis to reduce the white noise floor of the measurement system to below -160 dBc/Hz.

Phase noise data are presented in Figure 6.2. The absolute single-side-band phase noise  $\mathcal{L}(f)$  on an individual 10 GHz signal is given by curve (a). This curve is 3 dB below the measured noise, under the reasonable assumption that the contribution from both oscillators is equal and uncorrelated. The phase noise from the optical heterodyne between the two CW lasers using one of the combs is given by curve (b), which has been normalized to the 10 GHz carrier. This represents the present noise floor given by a single CW laser and the frequency comb. As can be seen, the optical and microwave data converge at -104 dBc/Hz at 1 Hz. Above 10 kHz, the noise floor is set by the photon shot noise of the 10 GHz photodetector. Curve (c) shows the calculated shot noise floor of -157 dBc/Hz for the 10 GHz signal delivered at a power level of -8 dBm from 4 mA of average photocurrent. In the range of 10 Hz to 1 kHz, the noise contribution of microwave amplifiers cannot be neglected, as shown in curve (d). The combined noise of the CW laser, frequency comb, amplifiers and shot noise is given by curve (e). There is good agreement between this projection and

the actual measurement, indicating that we have identified and properly accounted for the present limitations to the noise floor. The spurious peaks in the 10 GHz phase noise (Fig. 6.2, curve (a)) between 5 Hz and 300 Hz arise from unidentified intermittent noise sources that also appear on the optical comparison (in later measurements, these spurs were eliminated). The largest spur at 29 Hz is a known vibration of our laboratory floor. The microwave data in curve (a) were chosen to show the upper limit to the phase noise. Optical data without the spurs (curve (b)) were chosen to display the lower limit to the phase noise with our current optical references and optical dividers, neglecting limitations due to photodetection of  $f_{rep}$ . The right axis of Figure 6.2 shows that even the largest spurs are sub-femtosecond and the integration over 1 Hz to 1 MHz yields a timing jitter of 760 as. The extension of this integration to 5 GHz at the present shot-noise level yields timing jitter of  $\sim 25$  fs. Straightforward reduction of the noise floor with band-pass filters provides still lower integrated jitter. At Fourier frequencies above  $\sim 10$  kHz, the achieved phase noise of Fig. 6.2 approaches the shot-noise limited floor of  $-157$  dBc/Hz. In the absence of photodiode saturation, this phase noise floor should decrease proportionately to the detected optical power, implying that a 10-fold increase in optical power would be required to obtain a 10 dB decrease in the noise floor.

In addition to the 10 GHz microwave signal, the optical stability of the frequency comb and the CW lasers was also measured, thereby obtaining a lower limit of the timing stability of the microwave signals. This is accomplished by measuring and analyzing the optical beat signal  $f_b$  between the second stabilized CW laser and a tooth of the frequency comb that is independently stabilized by the first CW laser. For the counting measurements, the offset beat between the two 10 GHz signals was tuned to  $\sim 50$  kHz. The output of the mixer was low-pass filtered, amplified and input to a high-resolution L-type counter [135]. The fractional frequency instability of Fig. 6.3b was calculated from a time series of these counter measurements for both the microwave and optical data. By integration of the appropriately weighted phase noise spectrum of Fig. 6.2, it was verified that the 1 s instability presented here was consistent with the counter data of Fig. 6.3 and with the more conventional Allan Deviation [135].

In Figure 6.3, the corresponding frequency counter data show the instability of the 10 GHz

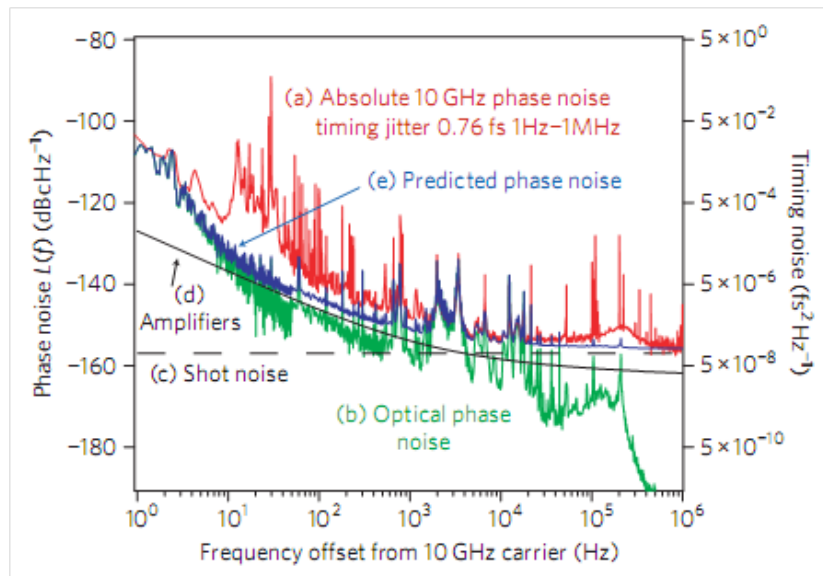


Figure 6.2: Phase noise spectrum of the photonically generated 10 GHz microwaves and contributing noise sources. a. Measured phase noise for a single photonic oscillator (red), b. Measured phase noise for a single optical reference (green), c. Calculated shot noise floor (dashed black), d. Specified amplifier noise floor (solid black), e. Sum of curves b, c, and d (blue), yielding the estimated phase noise achievable with the current systems.

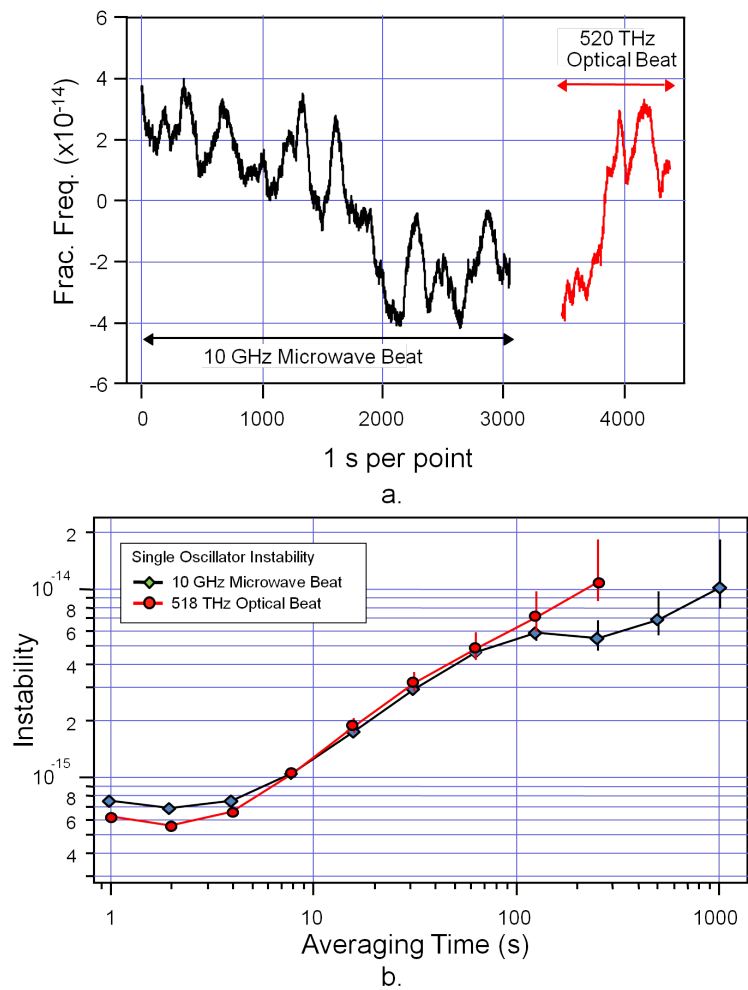


Figure 6.3: a. Time record of measured beat frequency between two 10 GHz signals and the beat signal of the optical comparison of the two CW reference lasers, b. Fractional frequency instability, calculated from the data in (a) for a single oscillator, assuming equal contributions to instability from each oscillator.

microwave signals and the optical instability of the CW lasers and frequency comb. The time record of frequency counter measurements (1 s gate time) is shown in Fig. 6.3a, and the fractional frequency instability calculated from these data are in Fig. 6.3b. Under the assumption of equal and uncorrelated oscillators, the data of Fig. 6.3b have been reduced by a factor of  $\sqrt{2}$  from the measurement. These data have not been post-processed, and the slow oscillations and linear drift seen in Fig. 6.3a are the result of temperature variations of the independent FP cavity references.

The close-to-carrier phase noise and short-term instability with this approach are lower than that achieved with any other room-temperature 10 GHz oscillator. With a thermal noise-floor limited optical cavity, a phase noise of  $\mathcal{L}(f) = -117$  dBc/Hz at a 1 Hz offset appears feasible [32] [33]. Even lower phase noise levels might be achieved in the future with new optical references based on spectral hole-burning techniques [34]. As can be seen in Fig. 6.4, the present noise is comparable to only the very best cryogenic dielectric oscillators [24][29] [30] [25]. Opto-electronic oscillators (OEOs) have achieved lower noise floors at Fourier frequencies  $>1$  kHz [27], but all such photonic devices with photodetectors have a noise floor ultimately limited by shot noise and the power-handling capabilities of the high-speed photodiode. As previously seen, higher repetition rates and higher power photodetectors would alleviate photodiode saturation effects and improve the shot noise floor.

A still lower noise floor could be achieved with a hybrid approach: locking a low-noise, room temperature dielectric sapphire oscillator [26] to this photonic oscillator to combine the low offset performance of the optical frequency reference with the non-shot noise limited performance of a microwave oscillator far from carrier. This approach and the resulting phase noise are described in the following section.

## 6.2 Residual and Absolute Phase Noise with Hybrid Photonic-Microwave Oscillator

While microwaves generated by a photonic approach are very low phase noise close to carrier, the spectral purity is fundamentally limited at larger frequency offsets by photodetection shot noise.

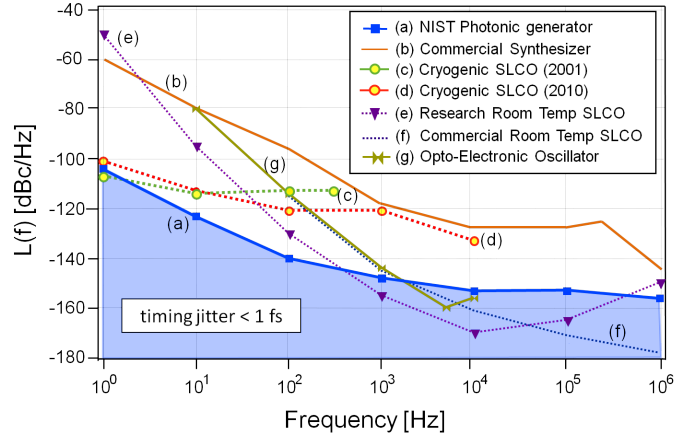


Figure 6.4: Approximate single-sideband phase noise for several leading microwave generation technologies in the 10 GHz range. Spurious tones have been neglected for all data. a. Result of the present work, b. A commercial, quartz-based synthesizer [23], c and d. Cryogenic sapphire oscillators [24] [25], e. Research room-temperature sapphire oscillator [26], f. Commercial room-temperature sapphire oscillator, g. Opto-electronic oscillators [27].

Microwave oscillators are not limited by shot noise; however, they do not provide the close-to-carrier stability desired by many applications. A unique approach to generating a 10-GHz signal with ultra-low phase noise at all Fourier frequencies is to phase-lock a microwave oscillator to a stable optical reference, creating a hybrid oscillator with the close-to-carrier stability of the optical reference and the far from carrier performance of a microwave oscillator not limited by shot noise.

High power 10 GHz oscillators containing a microwave reference cavity (sapphire loaded cavity oscillator, or SLCO) can reach a thermal noise limited floor that is three orders of magnitude lower than that of the cavity-stabilized CW reference [28]. The microwave reference cavity, however, has a significantly lower quality factor ( $Q$ ) than the optical reference cavity, resulting in a very clean waveform, but one whose center frequency wanders slowly with time. The best of both signals are combined by synchronizing the cycles from the SLCO, on a timescale  $<0.2$  ms, to those from the photonic generator. Characterizing the timing stability of the hybrid source requires comparison against a reference with similar or better performance. A second fully independent, but nearly identical hybrid microwave oscillator was built as a reference, and by operating both systems at the same frequency and mixing their output signals, the timing noise of the 10 GHz signals is isolated

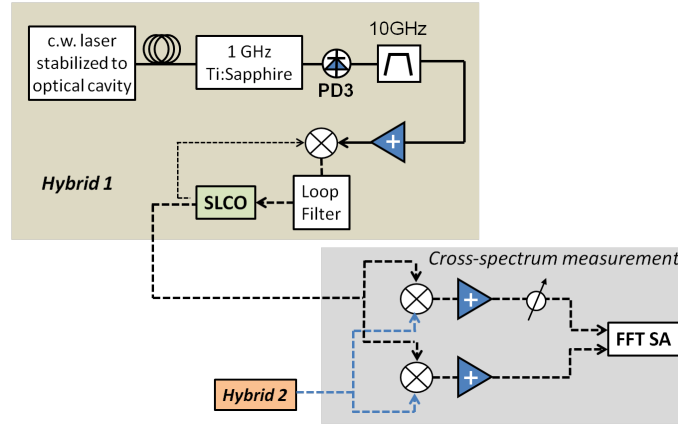


Figure 6.5: Schematic of the locking of the hybrid oscillator and the cross-spectrum measurement system.

from the carrier.

Figure 6.5 shows the schematic of the hybrid oscillators and the cross-spectrum measurement system. The 10 GHz microwave signal from the SLCO (+15 dBm) is disciplined to that from the photonic oscillator via an electronic phase lock with a 5 kHz loop bandwidth within the loop filter. Filtering and amplification of the 10th harmonic of  $f_{rep}$  generates a 10 GHz signal with a signal strength of 0 dBm. An absolute phase noise measurement is obtained via comparison between two nearly identical hybrid systems using a cross-spectrum measurement [136]. This technique allows for suppression of the electronic noise of amplifiers and mixers in the measurement system by  $\sqrt{N}$ , where  $N$  is the number of averages. To reach a noise floor of  $5 \times 10^{-19}$  rad<sup>2</sup>/Hz requires fifteen minutes and 10,000 averages. During this time the passive stability of the hybrid oscillators is sufficient to maintain the 10 GHz signals in quadrature without the use of a slow feedback loop.

The Fourier transformation of this noise yields a spectrum of the timing error for frequencies offset from the 10 GHz carrier. Figure 6.6 shows the comparison of the microwave signals from the photonic and sapphire oscillators as well as the output of the hybrid oscillators. As seen in Fig. 6.6c, the noise spectrum of the hybrid signal is the combination of the high frequency spectrum from the SLCO microwave source (Fig. 6.6a) and the low frequency noise spectrum from the photonic oscillator (Fig. 6.6b). Integration of the phase noise on the hybrid oscillator results

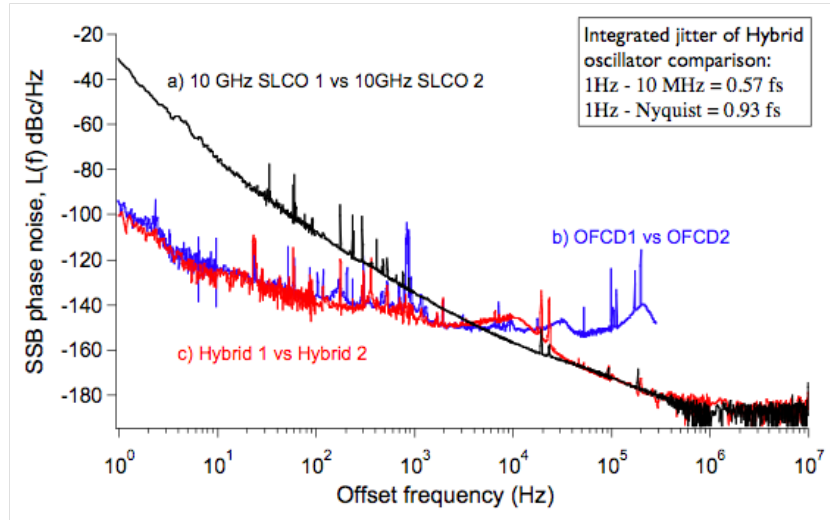


Figure 6.6: Phase noise on the 10 GHz signal for (a) microwave sapphire loaded cavity oscillator (SLCO), (b) optical oscillator with a frequency-comb-based optical frequency divider (OFCD), and (c) the hybrid oscillator based on the combination of the microwave and optical devices.

in an unprecedented combined absolute timing jitter for the two hybrid 10 GHz oscillators of 590 attoseconds (1 Hz to 5 GHz). For comparison, the absolute timing jitter for the SLCOs and the photonic generators are 295 fs and 12 fs (1 Hz to 5 GHz), respectively. Assuming that both hybrid oscillators contribute equally, the single oscillator timing jitter would be 420 attoseconds. Alternatively, if it were possible to overlap  $10^{10}$  consecutive cycles from the output of the hybrid oscillator, the zero crossings would exactly match within an *rms* difference of only 4 parts per million of one cycle.

While the overall spectral purity of this combination of the best photonic and microwave technologies is exceptional, this is not a practical or cost-effective approach for a fieldable low-noise oscillator. To improve the ultimate shot noise floor that limits the photonic oscillator at higher offset frequencies, we can make use of the improved saturation given by repetition rate multiplication and higher-power photodetectors. These lower cost and more robust options are more practical for ultimately generating an ultra-stable 10 GHz source for use in state-of-the-art applications.

### 6.3 Residual Noise on Er:Fiber laser with repetition rate multiplication

To determine the relative impact of repetition rate multiplication on the phase noise floor of the photodetected optical signals, we compare the residual phase noise of the 250-MHz repetition rate output of an Er:fiber laser compared to that using the Fabry-Perot filter cavity and Mach-Zehnder fiber interferometers. Since we are only considering the change in the white noise floor of the phase noise, the optical frequency divider is not locked to an optical frequency reference, which sets the close-in noise.

The signals from two independent repetition rate multipliers are compared using the residual phase noise measurement system of Figure 6.7. The 250-MHz repetition rate of the commercial Er:fiber mode-locked laser is locked to a 10-GHz synthesizer reference. The Er:fiber laser has two 35-mW outputs, which are directly used to measure the phase noise of two cascaded MZI. For the cavity case, one of the laser outputs is amplified to approximately 180 mW using an Erbium-doped fiber amplifier (EDFA); the output is split evenly and input to two identical 5-GHz FP cavities. For the unfiltered repetition rate case, the unamplified laser signal is also split evenly. The resulting outputs are detected with the two identical photodiodes in the dual-packaged PD2 with SMF pigtails; this generates the comb of microwave frequencies at harmonics of the repetition rate of the optical pulse train. The desired frequency of 10 GHz is selected by narrow bandpass cavity-filters, and microwave amplifiers are used as needed to increase the signals to about 0 and 7 dBm to drive the RF and LO ports of the mixer, respectively. The relative phases of the two inputs to the mixer are adjusted with a phase shifter to be in quadrature, for maximum sensitivity to phase fluctuations. A low-noise baseband amplifier with 20-dB gain is used after the mixer to enhance the measurement sensitivity, and the voltage fluctuations at its output are recorded and analyzed with a fast-Fourier transform spectrum analyzer (FFT). Using the measured voltage-to-phase conversion factor of the mixer,  $k_d$ , the spectral density of phase noise is obtained.

Fig. 6.8 shows the measured residual single-sideband phase noise of the 10-GHz signal obtained with the previously discussed setups. The data of Fig. 6.8 have been reduced by -3 dB to

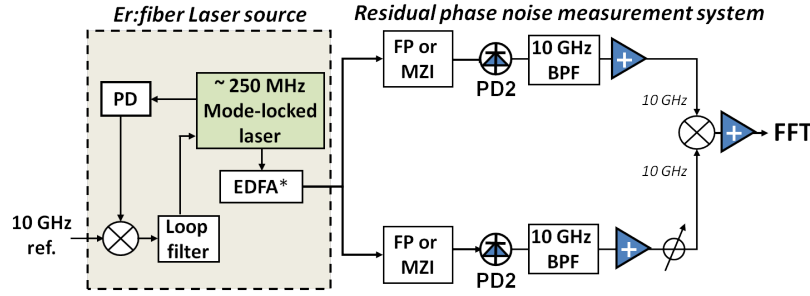


Figure 6.7: Schematic of the residual phase noise measurement system for the Er: fiber 250 MHz mode-locked laser. The EDFA (Erbium-doped fiber amplifier) is only used for measuring the residual noise with the FP cavity multiplier. FFT is the fast-Fourier transform spectrum analyzer.

represent the noise of a single system under the assumption of equal noise contributions from the repetition rate multipliers in both arms of the phase measurement system. The lowest phase noise floors are  $-158$  dBc/Hz and  $-162$  dBc/Hz for FP cavity and MZI approaches, respectively, which is an improvement of  $>10$  dB as compared with no repetition rate multiplication. The additional noise in the frequency range from 1 Hz to 1 kHz is introduced by thermal, mechanical, and acoustic fluctuations of the FP filter cavities and the MZI fibers, which were not addressed in this experiment. The variation seen at these frequencies ( $<1$  kHz) arises from slight differences in the experimental setup and environmental isolation. Improvements can be expected with more attention to these details. In the case of the FP filter cavities (see curve (e) of Fig. 6.8), the EDFA used before the cavities adds additional noise in the 1-Hz to 10-Hz range. Nonetheless, the close-to-carrier residual phase noise is not seen to be a fundamental limitation.

At Fourier frequencies above 100 kHz, the measured residual phase noise with the MZIs is 36 dB higher than the calculated values. This is due primarily to AM-to-PM conversion, as well as the cavity loss of the 10-GHz bandpass filter ( $\sim 2$  dB) and extra noise introduced by the measurement system (including the microwave amplifiers, mixer, baseband amplifier, and the Fourier-transform spectrum analyzer). For the FP cavity case (see curve (e) of Fig. 6.8), the measured phase noise is about 9 dB higher than the calculated value. This is attributed to the amplified spontaneous emission (ASE) of the EDFA required to increase the optical power following the FP

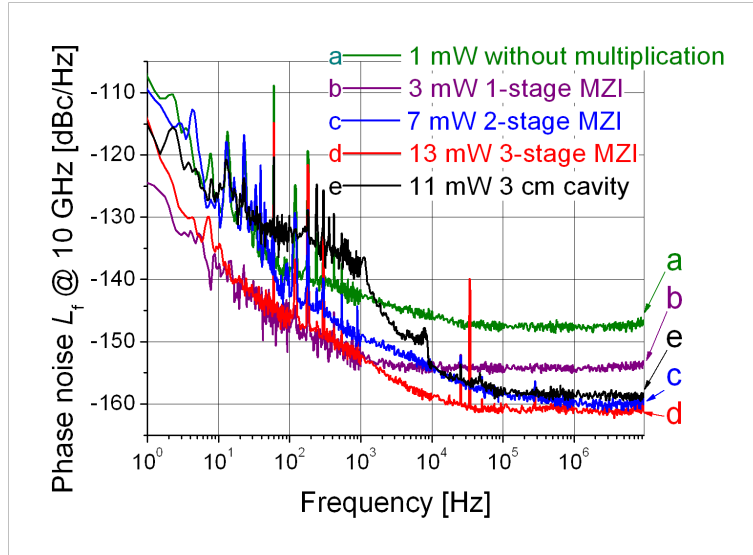


Figure 6.8: Residual phase noise of repetition rate multiplication schemes.

cavity filter. This was verified with an independent measurement of the noise floor of a single PD output with a spectrum analyzer at a frequency of 600 MHz. This spectrum analyzer noise floor agrees with the measurement result of Fig. 6.8(e) within 2 dB. This noise floor can be reduced by increasing the cavity transmission power (or seed power of the EDFA) and by using an EDFA with lower noise figure. However, it cannot be completely eliminated.

Unfortunately, in all cases the AM-to-PM noise conversion of the photodiodes is not negligible, especially since the commercial mode-locked laser has significant residual intensity noise ( $RIN \approx -140$  dBc/Hz) from a few kilohertz to a few megahertz. In order to get the lowest noise floor for the data of Fig. 6.8, we had to choose a proper working point where  $\alpha$  is very low, making the noise converted from laser amplitude noise well below that of other noise sources. One proper working point is about 6 pJ per pulse, corresponding to 1.5 mW without multiplication and 12 mW with a three-stage MZI. However, for the four-stage MZI, this working point is beyond the safe operating range of the PD. For the FP cavity filter approach, the proper working point is different because its output is a series of pulses with different energies. This could be improved by using photodiodes with lower AM-to-PM conversion, such as PD3 or PD4; however, this result still demonstrates improvement in the white noise level of the phase noise with repetition rate multiplication.

## 6.4 Residual phase noise with MUTC diodes

Residual phase noise measurements were also made with the MUTC diodes from the University of Virginia. Since these photodiodes produce very large 10-GHz signals with, even more so with repetition rate multiplication, the white noise floor decreases, allowing for even lower phase noise at high offset frequencies.

The measurement system depicted in Figure 6.7 was used to measure residual phase noise on the 10 GHz signal generated by HD-MUTC4, 34  $\mu\text{m}$ , with both a three-stage and a five-stage MZI. The residual phase noise using the three-stage MZI is shown in the green plot in Figure 6.9. This three-stage MZI produces a pulse train with a repetition rate of 2 GHz. The unamplified incident optical power after filtering was  $\sim 70$  mW, producing 10 mA of photocurrent with 21 V bias. The single-oscillator phase noise is -167 dBc/Hz at 10 MHz, about 6 dB less than the result for PD2 with the three-stage MZI shown in Figure 6.8 (also shown in Figure 6.9 (red)). The elevated noise level between  $\sim 100$  kHz and 4 MHz is mostly due to AM-to-PM conversion; however, even with this, the result is still significantly better.

The residual phase noise measurements demonstrated in the previous two sections clearly show that repetition rate multiplication and photodiode improvements make significant improvements in the phase noise, particularly in reducing the shot noise limited floor at high Fourier frequencies. In this region, laser servos are not limiting the noise floor, so similar reductions in the shot noise floor should be achieved with an absolute noise measurement as well. The biggest consideration is still the appropriate handling of AM-to-PM conversion, which can be significant at these high offset frequencies. Operating at a null, as observed in Section 5.3.3, is one effective method for dealing with this phenomenon.

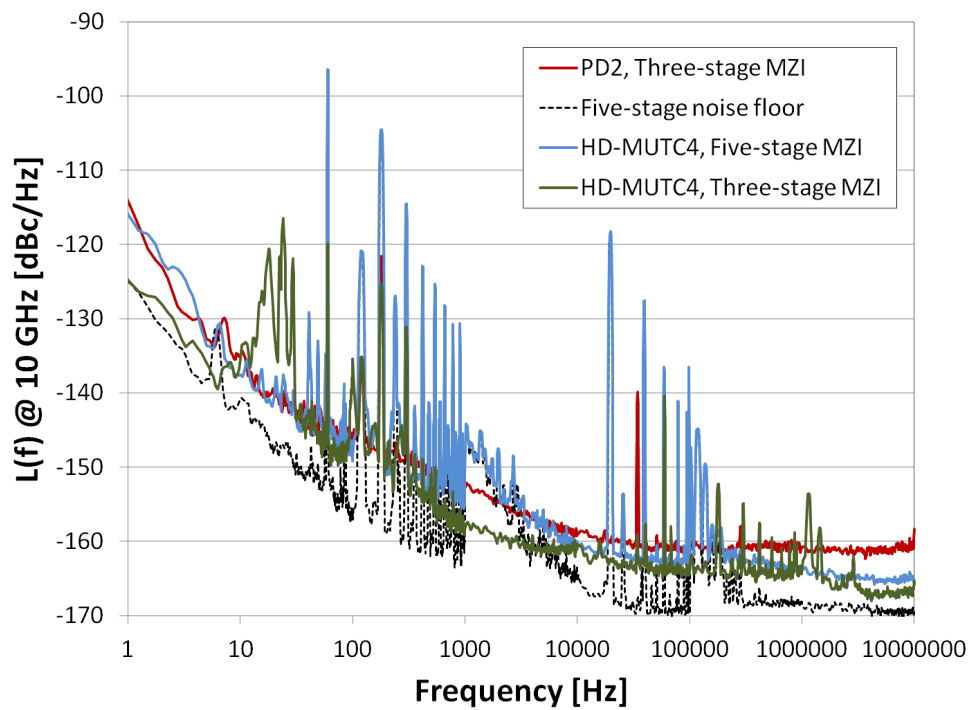


Figure 6.9: Phase noise at 1550 nm for HD-MUTC4 with three-stage MZI (green) and five-stage MZI (blue). Noise floor for PD2 with three-stage MZI (red) and noise floor of five-stage MZI system (black) shown for reference.

## Chapter 7

### Conclusion and Future Work

#### 7.1 Review of results and analysis

The work in this thesis demonstrates 10-GHz signals with some of the lowest phase noise ever recorded over a full range of Fourier frequencies (1 Hz to 10 MHz). These ultra-stable microwave signals are produced by dividing the stable output of an optical frequency reference–CW laser stabilized to an optical cavity–and using a stabilized femtosecond model-locked laser to divide the optical signal to 10 GHz through photodetection of the repetition rate.

The fundamental noise limitations of each part of this method have been described. Optical cavities are limited by thermal noise, limiting the close-in noise to below -100 dBc/Hz, which is comparable to cryogenic SLCOs. Noise on the optical pulse train as well as stabilization of  $f_0$  and  $f_b$  and amplitude noise on the pump laser limit the stability of the femtosecond frequency dividers. However, these effects are small compared to the current noise contributions due to photodetection. The effect of these noise limitations on the generation of ultra-stable microwave sources was thoroughly analyzed in this work.

Far from carrier, the shot noise due to the photodetector sets the noise floor for any optical system. As the incident optical power on the photodiode increases, charge carriers in the semiconductor slow as they move across the intrinsic region due to space charge screening. For pulsed inputs, this broadens the output impulse response, and the decrease in mobility causes the microwave power to level off instead of continuing to increase, an effect called saturation. The shot noise limit can be greatly reduced by reducing saturation at high power. Repetition rate mul-

tiplication is an effective solution; increasing the frequency of incident pulses reduces the energy per pulse and allows charge carriers in the photodiode to respond without the device saturating as quickly.

Amplitude-to-phase conversion in photodiodes is also a significant noise effect. Related to the space charge effect, fluctuations in the amplitude of the incoming optical signal are translated into phase fluctuations, thus adding extra phase noise onto an otherwise phase stable signal. This is especially a concern with the high intrinsic amplitude noise pump lasers of femtosecond laser dividers. One characteristic of AM-to-PM conversion, particularly at low repetition rates, is the presence of alternating nulls and large peaks at certain values of the photocurrent. Advances in photodetector design such as optimal diode illumination and improved absorption are shown to improve AM-to-PM conversion levels and reduce the size and occurrence of peaks and nulls. However, repetition rate multiplication has the most significant effect on reducing the peaks and nulls in the range of available photocurrent.

This thesis shows the first thorough characterization of phase noise associated with the photodetection of optical signals for microwave generation. By pairing photodiodes capable of high power handling (thereby providing optimal shot noise performance) and low AM-to-PM conversion with high repetition rate sources, the shot noise floor of the optically generated 10-GHz microwaves can be significantly decreased (Figs. 6.8 and 6.9). In fact, recent measurements done in our research group since the completion of the work presented in this thesis show absolute phase noise levels of  $\mathcal{L}(f) = -177$  dBc/Hz using these techniques.

## 7.2 Future Work

While this research demonstrates some of the lowest phase noise 10 GHz signals ever recorded, there is still room for development and improvement of the overall optical-to-microwave system. One area of current research is development of new optical frequency references. Current optical frequency reference cavities have almost reached the fundamental limit of performance, but even lower phase noise levels could be achieved with optical references based on new technologies. Work

has also been done to test and improve the performance in non-laboratory environments. One recent approach to improving the thermal noise limit is a cryo-cooled, silicon single-crystal optical cavity [137]. High environmental isolation and cryogenic cavity temperature stabilization allows operation of this cavity in a regime where fluctuations in cavity length are suppressed, resulting in fractional frequency stability of  $1 \times 10^{-16}$  at short timescales.

Spectral hole-burning is another technique used to circumvent thermal limitations. It compares the CW laser frequency to a narrow transparency in the absorption spectrum of a crystal [34]. Since spectral holes are atomic frequency references that are weakly perturbed through coupling to the crystal, the fundamental noise limit is expected to be lower than that of thermomechanical limits in current reference cavities.

The performance of an optical frequency reference has recently been demonstrated in a non-laboratory environment [138]. The cavity-stabilized CW laser and all associated electronics were mounted to a test platform placed inside of a passenger vehicle. Vibration sensitivity and frequency response were tested while idling and driving the vehicle. Initial tests show acceleration sensitivity one order of magnitude lower than that of the best rf crystal oscillators, showing promise for the development of this technology for a fieldable photonic oscillator [138].

Although Ti:sapphire systems demonstrate excellent performance in the laboratory, their environmental sensitivity and reliance on large, high power pump lasers are limiting factors for development of a portable photonic oscillator. Other frequency combs could be candidates for a more fieldable system. Er: fiber frequency combs have been demonstrated that have excellent close-to-carrier phase noise performance and low acceleration sensitivity. They are also diode pumped, reducing their size and required power, and operate at 1550 nm, a telecom frequency for which there are many convenient system components available for use. While repetition rates are lower, the rep rate multiplication techniques demonstrated in this thesis, particularly the Mach Zehnder interferometers, could be used to overcome the saturation effects associated with this. Such systems will likely be an important component for a future optical frequency divider that operates outside the laboratory.

Microresonator-based optical frequency combs are small, high-Q devices that produce combs with repetition rates in the range of 10 to 1000 GHz [139][140][141][142]. Their size and the possibility for chip-scale integration make them intriguing for a portable microwave generation application. However, the small size can also create problems with noise and stabilization [142]. Ongoing research will prove whether these devices can perform at a level required for this application.

Another interesting prospect is the development of diode-pumped solid state lasers. Self-referencing, femtosecond pulses and gigahertz repetition rates have been demonstrated with these systems, but, most recently, 4.8 GHz was demonstrated with a semiconductor saturable absorber mirror (SESAM) mode-locked Yb:KGW laser [143]. This approach is anticipated to attain even higher repetition rates and shorter pulses in the future.

The growing demand for high power handling, high bandwidth photodetectors in applications requiring low-noise signals will continue to fuel research and development in this area. The analyses in this thesis clearly show that new design implementations make positive impacts in the noise limitations of a photodetector, including the saturation and amplitude-to-phase conversion. Another approach to reducing the shot noise floor is combining the microwave power from an array of independently-illuminated diodes [144]. In addition to further development of the internal structures to optimize performance, the MUTC diodes from the University of Virginia could be fully packaged for easier implementation into experiments and to reduce the size required for microwave probes and external fiber coupling.

Nonetheless, the analysis of shot noise and AM-to-PM conversion in this work shows that, to a degree, the noise limitation of photodetection can be improved despite a less than ideal device. Repetition rate multiplication can benefit any photodiode by changing the incoming pulse train itself to delay the onset of saturation. Likewise, the periodic nature of AM-to-PM conversion could mean the presence of nulls where the effect goes near to zero. If one is careful to monitor the exact location of the null, operating at a low point of AM-to-PM conversion is possible for any photodiode with this behavior.

A fieldable photonic generator will ultimately be achieved by the integration of the optical

frequency reference, femtosecond divider, and photodetector into one physical unit. The current system consists of an optical frequency reference sitting on an optical table in one room and the femtosecond frequency divider on an optical table in another room as much as 300 m away. Besides reducing the need for fiber link stabilization, moving these two systems together into the same room allows for the development of an integrated system. In addition to developing optical frequency references and femtosecond dividers that are less environmentally sensitive, an additional tactic for environmental isolation is placing the optical reference and frequency comb into a vibration isolation enclosure. This approach can be further enabled by reduction of size as well as power requirements of each system.

Furthermore, future developments in these technologies could mean changing the total architecture of the photonic oscillator entirely. Just as the femtosecond frequency divider changed the way optical frequencies are divided down to microwave frequencies using a convoluted frequency chain [3], advances in the current systems, or even the development of technologies not even envisioned at the present time, could lead to the next major step in the development of ultra-stable timing signals. Only time—and further innovative research—will tell what the next great technological advances in timing and metrology will be.

## Bibliography

- [1] S. A. Diddams, J. C. Bergquist, S. R. Jefferts, and C. W. Oates, “Standards of time and frequency at the outset of the 21st century,” Science, vol. 306, pp. 1318–1324, Nov. 2004.
- [2] S. A. Diddams, T. Udem, J. C. Bergquist, E. A. Curtis, R. E. Drullinger, L. Hollberg, W. M. Itano, W. D. Lee, C. W. Oates, K. R. Vogel, , and D. J. Wineland, “An optical clock based on a single trapped  $199\text{Hg}^+$  ion,” Science, vol. 293, pp. 825–828, Aug. 2001.
- [3] L. Hollberg, C. W. Oates, G. Wilpers, C. W. Hoyt, Z. W. Barber, S. A. Diddams, W. H. Oskay, and J. C. Bergquist, “Optical frequency/wavelength references,” Journal of Physics B: Atomic, Molecular, and Optical Physics, vol. 38, pp. S469–S495, Apr. 2005.
- [4] T. W. Hänsch, “Nobel Lecture: Passion for precision,” Reviews of Modern Physics, vol. 78, pp. 1297–1309, Oct.-Dec. 2006.
- [5] J. L. Hall, “Nobel Lecture: Defining and measuring optical frequencies,” Reviews of Modern Physics, vol. 78, pp. 1279–1295, Oct.-Dec. 2006.
- [6] S. A. Diddams, D. J. Jones, J. Ye, S. T. Cundiff, J. L. Hall, J. K. Ranka, R. S. Windeler, R. Holzwarth, T. Udem, and T. W. Hänsch, “Direct link between microwave and optical frequencies with a 300 THz femtosecond laser comb,” Physical Review Letters, vol. 84, pp. 5102–5105, May 2000.
- [7] A. Bartels, S. A. Diddams, C. W. Oates, G. Wilpers, J. C. Bergquist, W. H. Oskay, and L. Hollberg, “Femtosecond-laser-based synthesis of ultrastable microwave signals from optical frequency references,” Optics Letters, vol. 30, pp. 667–669, Mar. 2005.
- [8] J. J. McFerran, E. Ivanov, A. Bartels, G. Wilpers, C. W. Oates, S. A. Diddams, and L. Hollberg, “Low-noise synthesis of microwave signals from an optical source,” Electronics Letters, vol. 41, pp. 650–651, May 2005.
- [9] J. Millo, R. Boudot, M. Lours, P. Y. Bourgeois, A. N. Luiten, Y. L. Coq, Y. Kersalé, and G. Santarelli, “Ultra-low-noise microwave extraction from fiber-based optical frequency comb,” Optics Letters, vol. 34, pp. 3707–3709, Dec. 2009.
- [10] T. Nagatsuma, H. Ito, and T. Ishibashi, “High-power RF photodiodes and their applications,” Laser and Photonics Reviews, vol. 3, pp. 123–137, Feb. 2008.
- [11] G. C. Valley, “Photonic analog-to-digital converters,” Optics Express, vol. 15, pp. 1955–1982, Mar. 2007.

- [12] P. W. Juodawlkis, J. C. Twichell, G. E. Betts, J. J. Hargreaves, R. D. Younger, J. L. Wasserman, F. J. O'Donnell, K. G. Ray, and R. C. Williamson, "Optically sampled analog-to-digital converters," IEEE Transactions on Microwave Theory and Techniques, vol. 49, pp. 1840–1853, Oct. 2001.
- [13] S. Doeleman, Frequency Standards and Metrology: Proceedings of the 7th Symposium, pp. 175–183. World Scientific, First ed., 2009.
- [14] S. Doeleman, T. Mai, A. E. E. Rogers, J. G. Hartnett, M. E. Tobar, and N. Nand, "Adapting a cryogenic sapphire oscillator for very-long baseline interferometry," Publications of the Astronomical Society of the Pacific, vol. 123, pp. 582–595, May 2011.
- [15] J.-F. Cliché and B. Shillue, "Precision timing control for radioastronomy: Maintaining femtosecond synchronization in the Atacama Large Millimeter Array," IEEE Control Systems Magazine, vol. 26, pp. 19–26, Feb. 2006.
- [16] J. Kim, J. A. Cox, J. Chen, and F. X. Kärtner, "Drift-free femtosecond timing synchronization of remote optical and microwave sources," Nature Photonics, vol. 2, pp. 733–736, Dec. 2008.
- [17] Z. Huang and K. J. Kim, "Review of X-ray Free-Electron Laser Theory," Physical Review Special Topics—Accelerators and Beams, vol. 10, p. 034801.
- [18] M. Alterelli and et. al., "XFEL: The European X-Ray Free-Electron Laser, technical design report," DESY 2006-097, vol. at <http://xfel.desy.de>.
- [19] A. Winter, H. Schlarb, B. Schmidt, F. O. Ilday, J.-W. Kim, J. Chen, F. J. Grawert, and F. X. Kärtner, "Stabilized optical fiber links for the XFEL," Proceedings of 2005 Particle Accelerator Conference.
- [20] M. S. Kirchner and S. A. Diddams, "Grism-based pulse shaper for line-by-line control of more than 600 optical frequency comb lines," Optics Letters, vol. 35, pp. 3264–3266, Oct. 2010.
- [21] M. H. Khan, H. Shen, Y. Xuan, L. Zhao, S. Xiao, D. Leaird, A. M. Weiner, and M. Qi, "Ultrabroad-bandwidth arbitrary radiofrequency waveform generation with a silicon photonic chip-based spectral shaper," Nature Photonics, vol. 4, pp. 117–122, Feb. 2010.
- [22] L. Hollberg, S. A. Diddams, C. W. Oates, E. A. Curtis, S. Bize, J. C. Bergquist, and W. Itano, "Enhanced security in communications systems with optical frequency standards and femtosecond laser combs." Unpublished communication, 2004.
- [23] Agilent Technologies, "Agilent E8257D PSG Microwave Analog Signal Generator Data Sheet," tech. rep., Agilent Technologies, 2011.
- [24] A. G. Mann, C. Sheng, and A. N. Luiten, "Cryogenic sapphire oscillator with exceptionally high frequency stability," IEEE Transactions on Instrumentation and Measurement, vol. 50, pp. 519–521, Apr. 2001.
- [25] S. Grop, P. Y. Bourgeois, R. Boudot, Y. Kersalé, E. Rubiola, and V. Giordano, "10 GHz cryocooled sapphire oscillator with extremely low phase noise," Electronics Letters, vol. 46, pp. 420–422, Mar. 2010.

- [26] E. N. Ivanov and M. E. Tobar, “Low phase-noise sapphire crystal microwave oscillators: Current status,” IEEE Transactions on UFFC, vol. 56, pp. 263–269, Feb. 2009.
- [27] D. Eliyahu, D. Seidel, and L. Maleki, “RF amplitude and phase-noise reduction of an optical link and an opto-electronic oscillator,” IEEE Transaction on Microwave Theory and Techniques, vol. 56, pp. 449–456, Feb. 2008.
- [28] C. McNeilage, J. H. Searls, E. N. Ivanov, P. R. Stockwell, D. M. Green, and M. Mossammaparast, “A review of sapphire whispering gallery-mode oscillators including technical progress and future potential of the technology,” Frequency Control Symposium and Exposition: Proceedings of the 2004 IEEE.
- [29] C. R. Locke, E. N. Ivanov, J. G. Hartnett, P. L. Stanwix, and M. E. Tobar, “Invited article: Design techniques and noise properties of ultrastable cryogenically cooled sapphire-dielectric resonator oscillators,” Review of Scientific Instruments, vol. 79, p. 051301, May. 2008.
- [30] S. Grop, P. Y. Bourgeois, N. Bazin, Y. Kersalé, E. Rubiola, C. Langham, M. Oxborrow, D. Clapton, S. Walker, J. D. Vicente, and V. Giordano, “ELISA: A cryocooled 10 GHz oscillator with  $10^{-15}$  frequency stability,” Review of Scientific Instruments, vol. 81, p. 025102, Feb. 2010.
- [31] L. Maleki, “The opto-electronic oscillator,” Nature Photonics, vol. 5, pp. 728–730, Dec. 2011.
- [32] W. Zhang, Z. Xu, M. Lours, R. Boudot, Y. Kersalé, G. Santarelli, , and Y. L. Coq, “Sub-100 attoseconds stability optics-to-microwave synchronization,” Applied Physics Letters, vol. 96, p. 211105, May 2010.
- [33] Y. Y. Jiang, A. D. Ludlow, N. D. Lemke, R. W. Fox, J. A. Sherman, L.-S. Ma, and C. W. Oates, “Making optical atomic clocks more stable with  $10^{-16}$ -level laser stabiliziation,” Nature Photonics Letters, vol. 5, pp. 158–161, Jan. 2011.
- [34] M. J. Thorpe, L. Rippe, T. M. Fortier, M. S. Kirchner, and T. Rosenband, “Frequency stabilization to  $6 \times 10^{-16}$  via spectral-hole burning,” Nature Photonics, vol. 5, pp. 688–693, Nov. 2011.
- [35] B. C. Young, F. C. Cruz, W. M. Itano, and J. C. Bergquist, “Visible lasers with subhertz linewidths,” Physical Review Letters, vol. 82, pp. 3799–3802, May 1999.
- [36] A. D. Ludlow, X. Huang, M. Notcutt, T. Zanon-Willette, S. M. Foreman, M. M. Boyd, S. Blatt, and J. Ye, “Compact thermal-noise-limited optical cavity for diode laser stabilization at  $1 \times 10^{-15}$ ,” Optics Letters, vol. 32, pp. 641–643, Feb. 2007.
- [37] A. J. Benedick, J. G. Fujimoto, and F. X. Kärtner, “Optical flywheels with attosecond jitter,” Nature Photonics, vol. 6, pp. 97–100, Jan. 2012.
- [38] T. K. Kim, Y. Song, K. Jung, C. Kim, H. Kim, C. H. Nam, and J. Kim, “Sub-100-as timing jitter optical pulse trains from mode-locked Er-fiber lasers,” Optics Letters, vol. 36, pp. 4443–4445, Nov. 2011.
- [39] J. D. McKinney and K. J. Williams, “Sampled analog optical links,” IEEE Transactions on Microwave Theory and Techniques, vol. 57, pp. 2093–2099, Aug. 2009.

- [40] J. Capmany and D. Novak, “Microwave photonics combines two worlds,” Nature Photonics, vol. 1, pp. 319–330, Jun. 2007.
- [41] D. Leaird, A. Weiner, A. Joshi, and S. Datta, “2.5 V arbitrary waveform generation in the UWB-Band with high power handling, highly linear photodiodes,” Proceedings of the 2010 Microwave Photonics Conference, pp. Paper TH4–10, 2010.
- [42] J. Kim and F. Kärtner, “Attosecond-precision ultrafast photonics,” Laser and Photonics Reviews, vol. 4, pp. 432–456, May 2010.
- [43] K. J. Williams, R. Esman, and M. Dagenais, “Nonlinearities in p-i-n microwave photodetectors,” Journal of Lightwave Technology, vol. 14, pp. 84–96, Jan. 1996.
- [44] D. Tulchinsky and K. Williams, “Excess amplitude and excess phase noise of RF photodiodes operated in compression,” IEEE Photonics Technology Letters, vol. 17, pp. 654–656, Mar. 2005.
- [45] E. Ivanov, S. Diddams, and L. Hollberg, “Study of the excess noise associated with demodulation of ultra-short infrared pulses,” IEEE Transactions on Ultrasonics, Ferroelectrics, and Frequency Control, vol. 52, pp. 1068–1074, Jul. 2005.
- [46] M. Currie and I. Vurgaftman, “Microwave phase retardation in saturated InGaAs photodetectors,” IEEE Photonics Technology Letters, vol. 18, pp. 1433–1435, Aug. 2006.
- [47] E. Rubiola, E. Salki, N. Yu, and L. Maleki, “Flicker noise in high-speed p-i-n photodiodes,” IEEE Transaction on Microwave Theory and Techniques, vol. 54, pp. 816–820, Feb. 2006.
- [48] J. Kim and F. Kärtner, “Microwave signal extraction from femtosecond mode-locked lasers with attosecond relative timing drift,” Optics Letters, vol. 35, pp. 2022–2024, Jun. 2010.
- [49] C. W. Oates, F. Bondu, R. W. Fox, and L. Hollberg, “A diode-laser optical frequency standard based on laser-cooled Ca atoms: Sub-kilohertz spectroscopy by optical shelving detection,” The European Physical Journal, vol. 7, pp. 449–460.
- [50] T. Udem, S. A. Diddams, K. R. Vogel, C. W. Oates, E. A. Curtis, W. D. Lee, W. M. Itano, R. E. Drullinger, J. C. Bergquist, and L. Hollberg, “Absolute frequency measurements of the Hg<sup>+</sup> and Ca optical clock transitions with a femtosecond laser,” Physical Review Letters, vol. 86, pp. 4996–4999, May 2001.
- [51] W. M. Itano, J. C. Bergquist, A. Brusch, S. A. Diddams, T. M. Fortier, T. P. Heavner, L. Hollberg, D. B. Hume, S. R. Jefferts, L. Lorini, T. E. Parker, T. Rosenband, and J. E. Stalnaker, “Optical frequency standards based on mercury and aluminum ions,” Proc. SPIE, vol. 6673, pp. 667301–1–667303–11.
- [52] C. W. Hoyt, Z. W. Barber, C. W. Oates, T. M. Fortier, S. A. Diddams, and L. Hollberg, “Observation and absolute frequency measurements of the 1S<sub>0</sub>-3P<sub>0</sub> optical clock transition in neutral Ytterbium,” Physical Review Letters, vol. 95, pp. 083003–1–083003–4, Aug. 2005.
- [53] H. Katori, M. Takamoto, V. G. Pal’chikov, and V. D. Ovsiannikov, “Ultrastable optical clock with neutral atoms in an engineered light shift trap,” Physical Review Letters, vol. 91, pp. 173005–1–173005–4, Oct. 2003.

- [54] M. E. Poitzsch, J. C. Bergquist, W. M. Itano, and D. J. Wineland, “Cryogenic linear ion trap for accurate spectroscopy,” Review of Scientific Instrumentation, vol. 67, pp. 129–134, Jan. 1996.
- [55] C. W. Chou, D. B. Hume, J. C. J. Koelemeij, D. J. Wineland, and T. Rosenband, “Frequency comparison of two high-accuracy  $\text{Al}^+$  optical clocks,” Physical Review Letters, vol. 104, pp. 070802–1–070802–4, Feb. 2010.
- [56] G. Rempe, R. J. Thompson, H. J. Kimble, and R. Lalezari, “Measurement of ultralow losses in an optical interferometer,” Optics Letters, vol. 17, pp. 363–365, Mar. 1992.
- [57] R. W. P. Drever, J. L. Hall, F. V. Kowalski, J. Hough, G. M. Ford, A. J. Munley, and H. Ward, “Laser phase and frequency stabilization using an optical oscillator,” Applied Physics B, vol. 31, pp. 97–105, Feb. 1983.
- [58] T. Udem, J. Reichert, R. Holzwarth, and T. W. Hansch, “Absolute optical frequency measurement of the cesium D-1 line with a mode-locked laser,” Physical Review Letters, vol. 82, pp. 3568–3571, May 1999.
- [59] S. A. Diddams, D. J. Jones, L.-S. Ma, S. T. Cundiff, and J. L. Hall, “Optical frequency measurement across a 104-THz gap with a femtosecond laser frequency comb,” Optics Letters, vol. 25, pp. 186–188, Feb. 2000.
- [60] D. J. Jones, S. A. Diddams, M. S. Taubman, S. T. Cundiff, L.-S. Ma, and J. L. Hall, “Frequency comb generation using femtosecond pulses and cross-phase modulation in optical fiber at arbitrary center frequencies,” Optics Letters, vol. 25, pp. 308–310, Mar. 2000.
- [61] S. A. Diddams, “The evolving optical frequency comb,” J. Opt. Soc. Am. B, vol. 27, pp. B51–B60, Nov. 2010.
- [62] T. M. Ramond, S. A. Diddams, L. Hollberg, and A. Bartels, “Phase-coherent link from optical to microwave frequencies by means of the broadband continuum from a 1-GHz Ti:Sapphire femtosecond oscillator,” Optics Letters, vol. 27, pp. 1842–1844, Oct. 2002.
- [63] A. Bartels, C. W. Oates, L. Hollberg, and S. A. Diddams, “Stabilization of femtosecond laser frequency combs with subhertz residual linewidths,” Optics Letters, vol. 29, pp. 1081–1083, May 2004.
- [64] J. K. Ranka, R. S. Windeler, and A. J. Stentz, “Visible continuum generation in air-silica microstructure optical fibers with anomalous dispersion at 800 nm,” Optics Letters, vol. 25, pp. 25–27, 2000.
- [65] T. M. Fortier, A. Bartles, and S. A. Diddams, “Octave-spanning Ti:Sapphire laser with a repetition rate  $>1$  GHz for optical frequency measurements and comparisons,” Optics Letters, vol. 31, pp. 1011–1013, Apr. 2006.
- [66] L. E. Nelson, D. J. Jones, K. Tamura, H. A. Haus, and E. P. Ippen, “Ultrashort-pulse fiber ring lasers,” Applied Physics B, vol. 65, pp. 277–294, Apr. 1997.
- [67] F. Quinlan, T. M. Fortier, M. S. Kirchner, J. A. Taylor, M. J. Thorpe, N. Lemke, A. D. Ludlow, Y. Jiang, and S. A. Diddams, “Ultralow phase noise microwave generation with an Er:fiber-based optical frequency divider,” Optics Letters, vol. 36, pp. 3260–3262, Aug. 2011.

- [68] P. Wasylczyk, P. Wnuk, and et al., “Passively modelocked, diode-pumped Yb:KYW femtosecond oscillator with 1 GHz repetition rate,” Optics Express, vol. 17, pp. 5630–5635, Mar. 2009.
- [69] H. Byun, M. Y. Sander, A. Motamedi, H. Shen, G. S. Petrich, L. A. Kolodziejski, E. P. Ippen, and F. X. Kärtner, “Compact, stable 1 GHz femtosecond Er-doped fiber lasers,” Applied Optics, vol. 49, pp. 5577–5582, Oct. 2010.
- [70] S. Pekarek, C. Fiebig, and et al., “Diode-pumped gigahertz femtosecond Yb:KGW laser with a peak power of 3.9 kW,” Optics Express, vol. 18, pp. 16320–16326, Jul. 2010.
- [71] L. Peng, A. Wang, X. Wang, and Z. Zhang, “330 MHz repetition rate femtosecond Yb:fiber ring laser,” CLEO:2011 Laser Applications to Photonic Applications.
- [72] J. Alnis, A. Matveev, N. Kolachevsky, T. Udem, and T. W. Hänsch, “Subhertz linewidth diode lasers by stabilization to vibrationally and thermally compensated ultralow-expansion glass Fabry-Perot cavities,” Physical Review Letters A, vol. 77, p. 053809, May 2008.
- [73] S. A. Webster, M. Oxborrow, S. Pugla, J. Millo, and P. Gill, “Thermal-noise-limited optical cavity,” Physical Review A, vol. 79, pp. 033847–1–6, Mar. 2008.
- [74] M. Notcutt, L.-S. Ma, J. Ye, and J. L. Hall, “Simple and compact 1-Hz laser system via an improved mounting configuration of a reference cavity,” Optics Letters, vol. 30, pp. 1815–1817, Jul. 2005.
- [75] T. Nazarova and F. Riehle, “Vibration-insensitive reference cavity for an ultra-narrow-linewidth laser,” Applied Physics B, vol. 83, pp. 531–536, May 2006.
- [76] J. Millo, D. V. Magalhaes, C. Mandache, Y. L. Coq, E. M. L. English, P. G. Westergaard, J. Lodewyck, S. Bize, P. Lemonde, and G. Santarelli, “Ultrastable lasers based on vibration insensitive cavities,” Physical Review A, vol. 79, pp. 053829–1–8, May 2009.
- [77] M. J. Thorpe, D. R. Leibbrandt, T. Fortier, and T. Rosenband, “Measurement and real-time cancellation of vibration-induced phase noise in a cavity-stabilized laser,” Optics Express, vol. 18, pp. 18744–18751, Aug. 2010.
- [78] D. Leibbrandt, M. Thorpe, M. Notcutt, R. E. Drullinger, T. Rosenband, and J. C. Bergquist, “Spherical reference cavities for frequency stabilization of lasers in non-laboratory environments,” Optics Express, vol. 19, pp. 3471–3482, Feb. 2011.
- [79] K. Numata, A. Kemery, and J. Camp, “Thermal-noise limit in the frequency stabilization of lasers with rigid cavities,” Physical Review Letters, vol. 93, p. 250602, Dec. 2004.
- [80] L.-S. Ma, P. Jungner, J. Ye, and J. L. Hall, “Delivering the same optical frequency at two places: accurate cancellation of phase noise introduced by an optical fiber or other time-varying path,” Optics Letters, vol. 19, pp. 1777–17779, Nov. 1994.
- [81] S. M. Foreman, K. W. Holman, D. D. Hudson, D. J. Jones, and J. Ye, “Remote transfer of ultrastable frequency references via fiber networks,” Review of Scientific Instruments, vol. 78, p. 021101, Feb. 2007.

- [82] N. R. Newbury, P. A. Williams, and W. C. Swann, “Coherent transfer of an optical carrier over 251 km,” Optics Letters, vol. 32, pp. 3056–3058, Nov. 2007.
- [83] H. Jiang, F. Kefelian, S. Crane, O. Lopez, M. Lours, J. Millo, D. Holleville, P. Lemonde, C. Chardonnet, A. Amy-Klein, and G. Santarelli, “Long-distance frequency transfer over and urban fiber link using optical phase stabilization,” Journal of the Optics Society of America B, vol. 25, pp. 2029–2035, Dec. 2008.
- [84] G. Grosche, O. Terra, K. Predehl, R. Holzwarth, B. Lipphardt, F. Vogt, U. Sterr, and H. Schnatz, “Optical frequency transfer via 146 km fiber link with  $10^{19}$  relative accuracy,” Optics Letters, vol. 34, pp. 2270–2272, Aug. 2009.
- [85] J. B. Johnson, “Thermal agitation of electricity in conductors,” Physics Review, vol. 32, pp. 97–109, Jul. 1928.
- [86] H. Nyquist, “Thermal agitation of electric charge in conductors,” Physics Review, vol. 32, pp. 110–113, Jul. 1928.
- [87] A. Yariv, Optical Electronics, pp. 364–372. Saunders College Publishing, 4th ed., 1991.
- [88] B. E. A. Saleh and M. C. Teich, Fundamentals of Photonics, pp. 676–677. Wiley, 1st ed., 1991.
- [89] E. N. Ivanov, J. McFerran, S. Diddams, and L. Hollberg, “Noise properties of microwave signals synthesized with femtosecond lasers,” IEEE Transactions on Ultrasonics, Ferroelectrics, and Frequency Control, vol. 54, pp. 736–745, Apr. 2007.
- [90] B. E. A. Saleh and M. C. Teich, Fundamentals of Photonics, pp. 543–545. Wiley, 1st ed., 1991.
- [91] B. E. A. Saleh and M. C. Teich, Fundamentals of Photonics, pp. 429–430. Wiley, 1st ed., 1991.
- [92] B. E. A. Saleh and M. C. Teich, Fundamentals of Photonics, p. 551. Wiley, 1st ed., 1991.
- [93] B. E. A. Saleh and M. C. Teich, Fundamentals of Photonics, pp. 563–567. Wiley, 1st ed., 1991.
- [94] K. K. Ng, Complete Guide to Semiconductor Devices, pp. 431–434. Wiley-IEEE Press, 1st ed., 2002.
- [95] B. E. A. Saleh and M. C. Teich, Fundamentals of Photonics, pp. 657–661. Wiley, 1st ed., 1991.
- [96] A. Joshi and X. Wang, “DC to 50 GHz wide bandwidth InGaAs photodiodes and photoreceivers,” Proceedings SPIE 1999, vol. CR73, pp. 181–196.
- [97] B. E. A. Saleh and M. C. Teich, Fundamentals of Photonics, pp. 649–654. Wiley, 1st ed., 1991.
- [98] B. E. A. Saleh and M. C. Teich, Fundamentals of Photonics, pp. 645–648. Wiley, 1st ed., 1991.

- [99] F. J. Effenberger and A. Joshi, "Ultrafast, Dual-Depletion Region, InGaAs/InP p-i-n detector," Journal of Lightwave Technology, vol. 14, pp. 1859–1864, Aug. 1996.
- [100] A. Joshi, S. Datta, and D. Becker, "GRIN lens coupled top-illuminated highly linear InGaAs photodiodes," IEEE Photonics Technology Letters, vol. 20, pp. 1500–1502, Sep. 2008.
- [101] T. Ishibashi, T. Furuta, H. Fushimi, and H. Ito, "Photoresponse characteristics of uni-traveling-carrier photodiodes," Proceedings of SPIE, vol. 4283, pp. 469–479, Jan. 2001.
- [102] T. Ishibashi, S. Kodama, N. Shimizu, and T. Furuta, "High-speed response of uni-traveling-carrier photodiodes," Japanese Journal of Applied Physics, vol. 36, pp. 6263–6268, Oct. 1997.
- [103] Z. Li, H. Chen, H. Pan, A. Beling, and J. C. Campbell, "High-power integrated balanced photodetector," IEEE Photonics Technology Letters, vol. 21, pp. 1858–1890, Dec. 2009.
- [104] H. Pan, Z. Li, and J. C. Campbell, "High-power high-responsivity modified uni-traveling-carrier photodiode used as V-band optoelectronic mixers," Journal of Lightwave Technology, vol. 28, pp. 1184–1189, Apr. 2010.
- [105] X. Wang, N. Duan, H. Chen, and J. C. Campbell, "InGaAs-InP photodiodes with high responsivity and high saturation power," IEEE Photonics Technology Letters, vol. 19, pp. 1272–1274, Aug. 2007.
- [106] Y.-W. Chen, W.-C. Hsu, R.-T. Hsu, and Y.-H. Wu, "Low dark current InGaAs(p)/InP p-i-n photodiodes," Japanese Journal of Applied Physics, vol. 42, pp. 4249–4252, Feb. 2003.
- [107] A. Joshi and S. Datta, "Dual InGaAs photodiodes having high phase linearity for precise timing applications," IEEE Photonics Technology Letters, vol. 21, pp. 1360–1362, Oct. 2009.
- [108] A. Joshi and D. Becker, "GRIN lens coupled top-illuminated photodiodes for high-power applications," Proceedings of the Microwave Photonics Conference, pp. Paper W–1.5, 2007.
- [109] D. B. Sullivan, D. W. Allan, D. A. Howe, and F. L. Walls, "Characterization of clocks and oscillators," NIST Technical Note 1337.
- [110] W. J. Riley, "Handbook of frequency stability analysis," NIST Special Publication 1065.
- [111] D. Howe, "Frequency Stability," Encyclopedia of RF and Microwave Engineering, vol. 2, pp. 1706–1720.
- [112] J. A. McGee and D. Howe, "ThêoH and Allan deviations as power-law noise estimators," IEEE Transactions on Ultrasonics, Ferroelectrics, and Frequency Control, vol. 54, pp. 448–452, Feb. 2007.
- [113] S. A. Diddams, M. Kirchner, T. Fortier, D. Braje, A. M. Weiner, and L. Hollberg, "Improved signal-to-noise ratio of 10 GHz microwave signals generated with a mode-filtered femtosecond laser frequency comb," Optics Express, vol. 17, pp. 3331–3340, Mar. 2009.
- [114] J. Taylor, F. Quinlan, A. Hati, C. Nelson, S. Diddams, S. Datta, and A. Joshi, "Phase noise in the photodetection of ultrashort optical pulses," Proceedings of the 2010 IEEE International Frequency Control Symposium, pp. 684–688, 2010.

- [115] K. Williams and R. Esman, "Observation of photodetector nonlinearities," Electronics Letters, vol. 28, pp. 731–732, Apr. 1992.
- [116] W. Zhang, T. Li, M. Lours, S. Seidelin, G. Santarelli, and Y. L. Coq, "Amplitude to phase conversion of InGaAs pin photo-diodes for femtosecond lasers microwave signal generation," Applied Physics B, Lasers and Optics, vol. 106, pp. 301–308, Sep. 2011.
- [117] R. Esman and K. Williams, "Measurement of harmonic distortion in microwave photodetectors," IEEE Photonics Technology Letters, vol. 2, pp. 502–504, Jul. 1990.
- [118] S. Xiao, L. Hollberg, N. R. Newbury, and S. A. Diddams, "Toward a low-jitter 10-GHz pulsed source with an optical frequency comb generator," Optics Express, vol. 16, pp. 8498–8508, Jun. 2008.
- [119] S. A. Diddams, M. Kirchner, T. Fortier, D. Braje, A. M. Weiner, and L. Hollberg, "Improved signal-to-noise ratio of 10 GHz microwave signals generated with a mode-filtered femtosecond laser frequency comb," Optics Express, vol. 17, pp. 3331–3340, Mar. 2009.
- [120] D. A. Shaddock, M. B. Gray, and D. E. McClelland, "Frequency locking a laser to an optical cavity by use of spatial mode interference," Optical Letters, vol. 24, pp. 1499–1501, Nov. 1999.
- [121] B. Xia and L. R. Chen, "A direct temporal domain approach for pulse-repetition rate multiplication with arbitrary envelope shaping," IEEE J. Sel. Topics Quantum Electronics, vol. 11, pp. 165–172, Jan/Feb. 2005.
- [122] S. S. Min, Y. Zhao, and S. Fleming, "Repetition rate multiplication in figure-eight laser with 3 dB couplers," Optics Commun., vol. 277, pp. 411–413, Sep. 2007.
- [123] R. P. Scott, C. Langrock, and B. Kolner, "High-dynamic-range laser amplitude and phase noise measurement techniques," IEEE J. Sel. Topics Quantum Electronics, vol. 7, pp. 641–655, Jul/Aug. 2001.
- [124] K. H. Sann, "The measurement of near-carrier noise in microwave amplifiers," IEEE Transactions on Microwave Theory and Technique, vol. 9, pp. 761–766, Sep. 1968.
- [125] E. Rubiola and V. Giordano, "Advanced interferometric phase and amplitude noise measurements," Review of Scientific Instrumentation, vol. 73, pp. 2445–2457, Jun. 2002.
- [126] M. Ramond, S. Diddams, A. Bartels, and L. Hollberg, "Phase-coherent link from optical to microwave frequencies by means of the broadband continuum from a 1-GHz Ti:Sapphire femtosecond oscillator," Optics Letters, vol. 27, pp. 1842–1844, Oct. 2002.
- [127] W. Walls, "Frequency calibration standard using a wide band phase modulator," Mar. 1992.
- [128] P.-L. Liu, K. Williams, M. Frankel, and R. Esman, "Saturation characteristics of fast photodetectors," IEEE Transactions on Microwave Theory and Techniques, vol. 47, pp. 1297–1303, Jul. 1999.
- [129] L. Huang and C.-K. Sun, "Nonlinear saturation behaviors of high-speed p-i-n photodetectors," Journal of Lightwave Technology, vol. 18, pp. 203–212, Feb. 2000.

- [130] P. Hale, C. Wang, D. Williams, K. Remley, and J. Wepman, "Compensation of random and systematic timing errors in sampling oscilloscopes," IEEE Photonics Technology Letters, vol. 55, pp. 2146–2154, Dec. 2006.
- [131] C. Wang, P. Hale, and D. Williams, "Uncertainty of timebase corrections," IEEE Transactions on Instrumentation and Measurement, vol. 58, pp. 3468–3472, Oct. 2009.
- [132] J. Jargon, P. Hale, and C. Wang, "Correcting sampling oscilloscope timebase errors with a passively mode-locked laser phase locked to a microwave oscillator," IEEE Transactions on Instrumentation and Measurement, vol. 59, pp. 916–922, Apr. 2010.
- [133] T. Clement, D. Williams, P. Hale, and J. Morgan, "Calibrating photoreceiver response to 110 GHz," Proc. of LEOS, 2002, pp. 877–878.
- [134] S. A. Webster, M. Oxborrow, and P. Gill, "Subhertz-linewidth Nd:YAG laser," Optics Letters, vol. 29, pp. 1497–1499, Jul. 2004.
- [135] S. T. Dawkins, J. J. McFerran, and A. N. Lutien, "Considerations on the measurement of the stability of oscillators with frequency counters," IEEE Transactions on Ultrasonics, Ferroelectrics and Frequency Control, vol. 54, pp. 918–925, May 2007.
- [136] W. F. Walls, "Cross-correlation phase noise measurements," Proceedings of the 46th Frequency Control Symposium, pp. 257–261, May 1992.
- [137] T. Kessler, C. Hagemann, C. Grebing, T. Legero, U. Sterr, F. Riehle, M. J. Martin, L. Chen, and J. Ye, "A sub-40 mHz linewidth laser based on a silicon single-crystal optical cavity," arXiv, vol. arXiv:1112.3854, p. 250602, Jan. 2012.
- [138] D. R. Leibbrandt, M. J. Thorpe, J. C. Bergquist, and T. Rosenband, "Field-test of a robust, portable, frequency-stable laser," Optics Express, vol. 19, pp. 10278–10286, May 2011.
- [139] P. DelHaye, A. Schliesser, O. Arcizet, T. Wilken, R. Holzwarth, and T. J. Kippenberg, "Optical frequency comb generation from a monolithic microresonator," Nature, vol. 450, pp. 1214–1217, Dec. 2007.
- [140] A. A. Savchenkov, A. B. Matsko, V. S. Ilchenko, I. Solomatine, D. Seidel, and L. Maleki, "Tunable optical frequency comb with a crystalline whispering gallery mode resonator," Physics Review Letters, vol. 101, p. 093902, Aug. 2008.
- [141] T. J. Kippenberg, R. Holzwarth, and S. A. Diddams, "Microresonator-based optical frequency combs," Science, vol. 332, pp. 555–559, Apr. 2011.
- [142] S. B. Papp and S. A. Diddams, "Spectral and temporal characterization of a fused-quartz-microresonator optical frequency comb," Physical Review A, vol. 84, pp. 053833–1–7, Nov. 2011.
- [143] S. Pekarek, A. Klenner, T. Sudmeyer, C. Fiebig, K. Pashke, G. Erbert, and U. Keller, "Femtosecond diode-pumped solid-state laser with a repetition rate of 4.8 GHz," Optics Express, vol. 20, pp. 4248–4253, Feb. 2012.
- [144] Y. Fu, H. Pan, Z. Li, and J. Campbell, "High linearity photodiode array with monolithically integrated Wilkinson power combiner," 2010 IEEE Topical Meeting on Microwave Photonics.